

**Design and Implementation of a Lithium-ion Cell Tester
Capable of Obtaining High Frequency Characteristics**

Design and Implementation of a Lithium-ion Cell Tester Capable of Obtaining High Frequency Characteristics

By

Ali Delbari, B.Eng

A Thesis

Submitted to the School of Graduate Studies
in Partial Fulfilment of the Requirements
for the Degree of Master of Applied Science
in Mechanical Engineering
at McMaster University, Hamilton, ON,
Canada

Master of Applied Science (2016)

McMaster University

(Mechanical Engineering)

Hamilton, Ontario

TITLE: Design and Implementation of a Lithium-ion Cell Tester
Capable of Obtaining High Frequency Characteristics

AUTHOR: Ali Delbari B.Eng (McMaster University)

SUPERVISOR: Dr. Saeid R. Habibi

NUMBER OF PAGES: 100

Permission to Use

In presenting this thesis in partial fulfillment of the requirements for a Postgraduate degree from McMaster University, I agree that the Libraries of this University may take it freely available for inspection. I further agree that the permission for copying this thesis in any manner, in whole or in part for scholarly purposes, may be granted by the professors who supervised my thesis work or, in their absence, by the head of the Department or the Faculty Dean in which my thesis work was conducted. It is understood that any copying or publication or use of this thesis or parts thereof for financial gain shall not be allowed without my writing permission. It is also understood that due recognition shall be given to me and McMaster University in any scholarly use which may be made of any material in my thesis. Requests for permission to copy or to make other use of material in this thesis, in whole or part, should be addressed to:

Head of Department of Mechanical Engineering

McMaster University

Faculty of Engineering

1280 Main Street West

Hamilton, Ontario L8S 4L6

Canada

Abstract

The field of energy storage has improved drastically within the last two decades. Batteries of various chemistries have been relied on to provide energy for numerous portable electronic devices. Lithium-ion cells, when compared to other chemistries have been known to provide outstanding energy-to-weight ratios and exhibit low self-discharge when not in use [1]. The aforementioned benefits in conjunction with decreasing costs have made lithium-ion cells an exceptional choice for use in electrical vehicles (EVs). Battery Management Systems (BMS) in EVs are responsible for providing estimates for values that are indicative of the battery pack's present operating condition. The current operating condition could be described by State of Charge, power fade, capacity fade and various other parameters [2]. Importantly, it is essential for the estimation technique to adjust to fluctuating cell characteristics as the cell ages, in pursuance of having available accurate estimates for the life time of the pack. In order for the estimation technique to properly estimate the desired quantities, a mathematical model capable of capturing cell dynamics is desired. There are various proposed methods recommended for mathematically modeling a cell, namely equivalent Circuit modeling, electro-chemical modeling and impedance spectroscopy. Consequently, in order to ensure mathematical models are accurate and further to have the ability to compare the proposed models, it is essential to have available data gathered from a given cell at specific operating conditions. This Master's thesis outlines the development of a lithium-ion cell tester that is capable of controlling, monitoring and recording parameters such as current, voltage and temperature. The Dual capability of obtaining data from standardized cell tests as well as high frequency cell tests is fascinating and intriguing. As this capability holds the possibility of reducing cost otherwise spent on man hours and equipment which are both paramount in any industrially automated process.

Acknowledgements

I would like to first and foremost thank God, for his endless showers of blessings. I would like to express my gratitude to my parents: Hassan and Nadereh, and sister, Ariana. The values you have instilled in me, encouraged me to be a better person every waking moment. Your accomplishments in your own lives are a source of inspiration. Dr. Habibi, thank you for your kindness, guidance and support during the course of this dissertation. Cam Fisher, thank you for putting up with me despite my lack of ability to tie a ratchet strap properly (I don't know if I still can). Your help and guidance within and outside the scope of this project is greatly appreciated. Allen Pauric, Ryan Ahmed and Megan Wood, thank you for explaining concepts, helping with equipment and providing general assistance. Fellow lab members: Hamed, Mina, Atta, Mahmoud, Zhongzhen, Andrew, Yu and yifei, Sean, Essam thank you for laughing at my jokes despite the lack of humor. Your enthusiasm for your own projects were a source of encouragement for me and I truly enjoyed learning more about them and exchanging ideas. Last but not least, thanks to Max and Mishka for being awesome.

.

.

Table of Contents

Abstract.....	III
Acknowledgments.....	IV
Table of Contents.....	V
List of Figures.....	VIII
List of Tables.....	XII
Chapter 1: Introduction.....	1
1.1. Thesis Objectives.....	3
1.2. Thesis Organization.....	4
Chapter 2: Literature Review	5
2.1. Current Energy Situation.....	5
2.1.1. The 1800’s.....	7
2.1.2. 1900-1960.....	8
2.1.3. 1960-Present.....	9
2.2. Energy Storage Candidates.....	11
2.3. Lithium-ion Cell.....	13
2.4. Battery Management Systems.....	15
2.5. Battery Modeling.....	17
2.6. Equivalent Circuit Models.....	18
2.6.1. The Simple Model.....	18
2.6.2. The First-Order RC Model	19
2.6.3. The Second-Order RC Model.....	20

2.6.4. The Third-Order RC Model.....	21
2.7. The Electro-Chemical Model.....	22
2.8. Electro-Chemical Impedance Spectroscopy.....	26
2.9. EIS Model.....	30
2.10. Industry Testers.....	34
2.11. Summary.....	35
Chapter 3: Design of a Lithium-ion Cell Tester.....	37
3.1. Battery Tester Specification.....	38
3.2. Battery Tester Components.....	39
3.2.1. Battery Holder.....	39
3.2.2. Power Supply.....	42
3.2.3. Data Acquisition Chassis.....	42
3.2.4. Data Acquisition Modules.....	43
3.2.5. Environmental Chamber.....	44
3.2.6. Current Sensor.....	44
3.2.7. Thermocouples.....	45
3.2.8. Safety Circuit	48
Chapter 4: Results and Discussion.....	52
4.1. Characterization Tests.....	52
4.1.1. Static Capacity Test.....	53
4.1.2 SOC-OCV Test.....	58
4.1.3 Driving Cycles.....	63

4.1.4 Battery Cycling test.....	70
4.2. Electro-Chemical Impedance Spectroscopy	72
4.2.1 SOC Measurements	78
4.2.2 Ambient Temperature Measurements.....	80
4.2.3 Cycling Measurements.....	82
4.3 Equivalent-Circuit Modeling.....	84
4.4. EIS Modeling.....	91
4.5. Multi-objective Optimization.....	92
Chapter 5: Conclusion.....	93
5.1. Summary of Research.....	93
5.2. Future Work.....	94
Bibliography.....	96
Appendix.....	102

List of Figures

Figure 2.1: CO2 emissions in millions of tones.....	6
Figure 2.2: First Electric Powered Vehicle.....	8
Figure 2.3: Ford Comuta developed in 1967.....	9
Figure 2.4: Toyota Prius 1997.....	10
Figure 2.5: Ragone Plot of Energy Storage Devices.....	13
Figure 2.6: The components of a lithium-ion cell.....	14
Figure 2.7: Battery State of Health for HEV applications.....	17
Figure 2.8: Schematic drawing of the First-Order RC model.....	20
Figure 2.9: Schematic drawing of the Second-Order RC model.....	20
Figure 2.10: Micro-Macro cell model.....	26
Figure 2.11: EIS pattern of a lithium-ion cell.....	28
Figure 2.12: Change of EIS spectra during lithium-ion cell life span.....	29
Figure 2.13: Effect of Ambient Temperature in a Battery spectra at 50% SOC.....	30
Figure 2.14: Randles Cell.....	31
Figure 2.15: Diffusion processes in a battery.....	32
Figure 3.1: Tester Circuit Architecture.....	40
Figure 3.2: The Experimental Setup.....	41
Figure 3.3: Battery Holder Materials.....	41
Figure 3.4: Power Supply Connections.....	43
Figure 3.5: Current sensor PCB diagram.....	44
Figure 3.6: Current Sensor PCB.....	45

Figure 3.7: Thermocouple connections.....46

Figure 3.8: Thermocouple insertion sites.....47

Figure 3.9: Current sensor PCB diagram Part 1.....49

Figure 3.10: Current sensor PCB diagram Part 2.....50

Figure 3.11: Flow diagram for Current sensor PCB.....51

Figure 4.1: Front Panel Design for Capacity and SOC/OCV Tests.....53

Figure 4.2: Block Diagram for Static Capacity and SOC-OCV Tests.....54

Figure 4.3: Voltage vs Time for a Static Capacity test.....57

Figure 4.4: Current Vs Time for a Static Capacity Test.....57

Figure 4.5: Temperature Vs Time for a Static Capacity Test.....58

Figure 4.6: OCV vs SOC for charge and discharge.....59

Figure 4.7: Hysteresis vs SOC.....60

Figure 4.8: OCV vs SOC- Averaged Experimental Results and 10th Order Polynomial fit.....62

Figure 4.9: UDDS Driving Schedule Velocity Profile.....64

Figure 4.10:US06 Driving Schedule Velocity Profile.....64

Figure 4.11: HWFET Driving Schedule Velocity Profile.....65

Figure 4.12: UDDS Driving Schedule Cell Current Profile.....66

Figure 4.13: UDDS Driving Schedule Cell Voltage Profile66

Figure 4.14: HWFET Driving Schedule Cell Current Profile67

Figure 4.15: HWFET Driving Schedule Cell Voltage Profile67

Figure 4.16:US06 Driving Schedule Cell Voltage Profile68

Figure 4.17:US06 Driving Schedule Cell Voltage Profile68

Figure 4.18: Front Panel for drive cycle tests.....69

Figure 4.19: Block Diagram for drive cycle tests.....71

Figure 4.20: Resistor Setup for validation Test.....73

Figure 4.21: Bode Plot for the Power Supply74

Figure 4.22: Front Panel for EIS tests.....75

Figure 4.23: Block Diagram for EIS Tests.....76

Figure 4.24: Impedance vs. Frequency for Tester and Gammry tests.....77

Figure 4.25: Phase vs Frequency for Tester and Gammry tests.....78

Figure 4.26: Impedance vs. Frequency at different SOC.....79

Figure 4.27: Phase vs. Frequency at different SOC.....79

Figure 4.28: EIS spectra at different SOC.....80

Figure 4.29: Impedance vs. Frequency at different temperatures.....81

Figure 4.30: Phase vs. Frequency at different Temperatures.....81

Figure 4.31: EIS spectra at different Temperatures.....82

Figure 4.32: Impedance vs. Frequency at different SOH83

Figure 4.33: Phase Vs Frequency at different SOH.....83

Figure 4.34: EIS Spectra at different SOH.....84

Figure 4.35: Simulated Voltage and Actual Voltage vs. Time for First-Order R-RC Model.....85

Figure 4.36: Simulated Voltage and Actual Voltage vs. Time for First-Order R-RC Model with Hysteresis.....86

Figure 4.37: Simulated Voltage and Actual Voltage vs. Time for Second-Order R-RC Model....86

Figure 4.38: Simulated Voltage and Actual Voltage vs. Time for Second-Order R-RC Model with Hysteresis.....87

Figure 4.39: Simulated Voltage and Actual Voltage vs. Time for Third-Order R-RC Model.....	87
Figure 4.40: Simulated Voltage and Actual Voltage vs. Time for Third-Order R-RC Model with Hysteresis.....	88
Figure 4.41: RMSE for each model.....	90
Figure 4.42: Simulated vs. Actual EIS Spectra at 50%SOC and Room Temperature.....	91
Figure A.1: NI cDAQ-9188.....	102
Figure A.2: NI 9213, NI 9264, NI 9239, NI 9205.....	103

List of Tables

Table 2.1: ECM model nomenclature	24
Table 2.2: Specifications of the Battery Tester.....	35
Table 3.1: Specifications of the Battery Tester based on a lithium iron Phosphate Cell.....	38
Table 4.1: Block Diagram notes for Static Capacity and SOC-OCV tests.....	56
Table 4.2: Coefficients for the 10 th order polynomial fit to the SOC-OCV curve.....	61
Table 4.3: Block Diagram notes for Aging tests.....	72
Table 4.4: Block Diagram notes for EIS tests.....	77
Table 4.5: Identified parameters for six equivalent circuit models.....	89
Table A.1: Specifications for NI cDAQ-9188.....	101
Table A.2: Rate Specifications for the Environmental Chamber.....	104

Chapter 1

Introduction

The combustion reaction has powered the technological revolution responsible for fuelling many of the devices, machinery and appliances used today. From providing energy for aircrafts to micro-chips, humanity has depended in parts on burning fossil fuels to power its increasingly demanding needs. Over consumption however, has not been without consequence. The carbon dioxide produced as a by-product of the combustion reaction has induced global climate change. Carbon dioxide in particular, in combination with other greenhouse gases trap the solar energy in the atmosphere. This energy imbalance has led to creation of drought prone regions, erosion of ice sheets, rising sea levels and many other severe consequences [3]. Now, more than ever, there is a need for an alternative, cheap, reliable and sustainable power supply. Such a supply is especially desirable in the transportation industry, which is responsible for 28% of total United States [4] and 23% of total Canadian [5] greenhouse gas emissions. Here electrical energy using batteries can potentially prove very useful as they are able to store energy from a variety of different sources.

Batteries are increasingly used in the automotive industry, and there is a cumulating need to improve their performance. Generally, performance of a battery pack can be enhanced by having access to how the pack behaves under a given condition. Having access to information on the pack's condition, enables the Battery Management Systems (BMS) in EVs to optimize their performance without the fear of the occurrence of overcharge or discharge. The battery pack is comprised of individual cells connected in series and parallel configurations. Therefore as an initial step, it is important to have information and to characterize the behaviour of the cell in different operating conditions by modeling. These models can be used in BMS to estimate values such as State of Charge (SOC) and State of Health (SOH).

Models are typically parameterized using data from several standardized tests. The equipment used to carry out these tests, range in their capabilities. Generally testers feature several channels with the ability to provide sufficient current and voltage to perform tests such as characterization tests, and life cycle tests. These cell testers are also able to provide sufficient accuracy ($\pm 0.1\%$ of full scale) [6]. However most cell testers are unable to extract high frequency characteristics from the battery cell due to their limited sampling rate (10 ms). Furthermore in order to obtain the desired high frequency behavior of the cell, the cell needs to be disconnected from the cycler and attached to electro-chemical impedance spectroscopy (EIS) equipment.

The ability to perform high frequency tests such as EIS on the battery cell, provides an additional mechanism for observing and modeling processes occurring inside the cell. Electro-chemical impedance spectroscopy involves applying an AC signal that spans

range of frequencies (typically between 10^5 KHz to 10^{-3} Hz) to the cell and measuring its impedance. The results from this test provide the ability to make qualitative deductions on several phenomena, including electronic/ionic conduction in the electrode and electrolytes, interfacial charging at the surface films, charge and mass transfer effects [7].

The motivation of this thesis is to reduce cost and time spent on testing battery cells by developing a tester capable of conducting standardized characterization and life tests as well as high frequency electro-chemical impedance spectroscopy tests.

1.1. Thesis Objectives

The objective of this research are as follows:

- I.** To design and implement a cell tester system capable of controlling, monitoring and recording parameters such as voltage, current and temperature from the cell.
- II.** To develop a safety circuit module capable of keeping cell operation within safety limits specified by the manufacturer.
- III.** To provide additional capability to implement standardized cell tests, perform preloaded driving profiles and implement electro-chemical impedance spectroscopy tests.
- IV.** To develop and validate equivalent circuit models at different States of Charge and States of Health using experimental data.
- V.** To optimize equivalent circuit models using a Genetic Algorithm.

1.2. Thesis Organization

This thesis is organized into five chapters. Chapter one offers an introduction into why a battery tester system with dual capability was developed. Chapter two starts by explaining the current energy situation and how electrification of automobiles can have an impact on reducing emissions and conserving fuel for future generations. Energy storage technologies such as fuel cells and lithium-ion batteries are also discussed. Finally various modeling strategies for State of Charge and State of Health determination are presented. Chapter three provides a detailed description of the components such as the environmental chamber and the data acquisition modules utilized for the battery tester experimental setup. Chapter four provides the results obtained from performing a variety of standardized characterization and life tests as well high frequency EIS tests. Results from parametrization of six equivalent circuit models using a genetic algorithm are also presented. Chapter five discusses various shortcomings of the experimental setup, as well as means of improvement.

Chapter 2

Literature Review

The increasing sales of electric and hybrid electric cars in urban areas, in conjunction with the large assortment of consumer electronics are fueling demand for a portable, low-cost, environmentally friendly and reliable energy storage devices. Lithium-ion batteries currently provide one of the best solutions when considering cost, energy density and safety. This chapter presents an overview on the current state of lithium-ion battery technology in the automotive field.

2.1. Current Energy Situation

Presently, fossil fuels supply 80% and renewable resources supply only 13 % of the total global energy demand [8]. There are several concerns with the ongoing trend, mainly the limited sources of fossil fuels. Several studies suggest that the reserves of oil, coal and natural gas could be exhausted within the next 200 years [9]. Another issue worth addressing is the impact of emissions from burning fossil fuels on the environment. The presence of excess carbon dioxide in the atmosphere has been attributed to a rise in global temperatures, rise in sea levels, negative impacts on natural ecosystems and a rise in catastrophic weather events. The world's predicted carbon dioxide emission by year and

region, given no change to the current trend, is demonstrated in Figure 2.1. It is apparent that a change from the current trend of energy use is necessary in order to sustain the needs of the future generations and avoid global climate change.

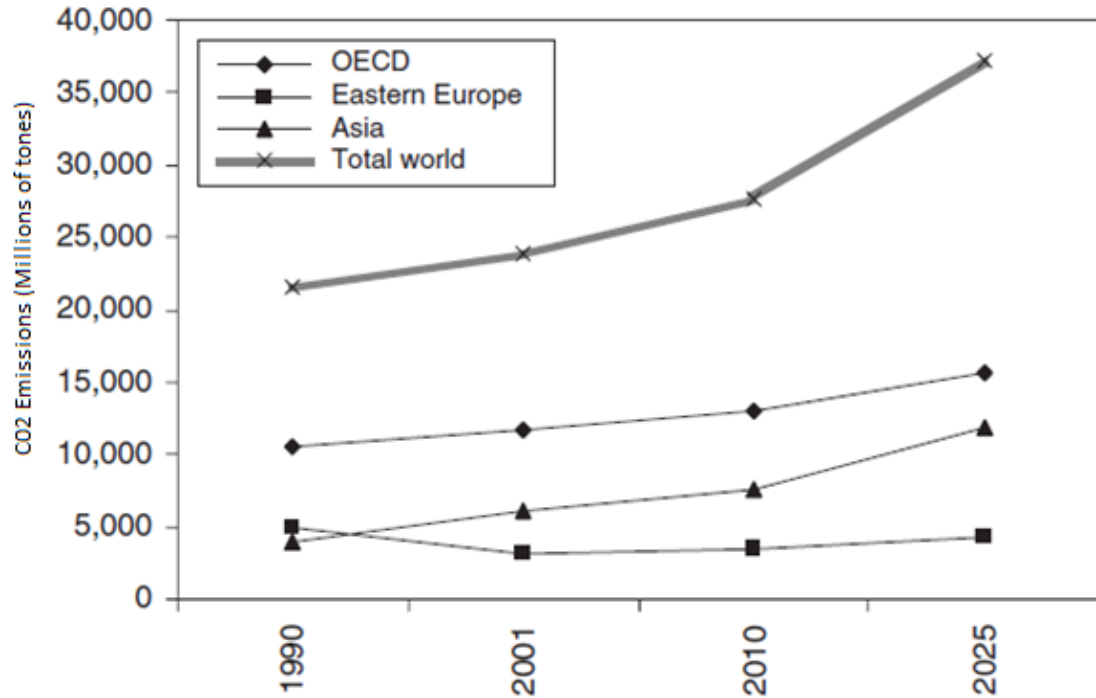


Figure 2.1: CO2 emissions in millions of tones [8]

Given that the transportation industry is responsible for such a large portion of the global emissions, alternative means of powering vehicles could be significant in reversing the current trend of climate change. A study performed in the United States found that electric vehicles produce lower global warming emissions compared to an average compact gasoline-powered vehicle even when the electricity used to power the vehicle was produced primarily from coal. The study also found that EVs that are powered mainly from renewable sources such as wind and solar, produce little to no emissions at all [10].

The question is then why is the industry not dominated by EVs. The answer to this question requires a look at the history of electrical vehicles, a brief summary of which is provided below:

2.1.1. The 1800's

Alessandro Volta inspired by earlier experiments of Luigi Galvani first invented the primary cell and battery in the early 1800's. Galvani conducted an experiment in which he witnessed the twitching of a frog's leg as a result of application of electric current. Later in 1821, Michael Faraday showcased the basic principles of electricity. Faraday continued on his research and in 1831 demonstrated the principles of electromagnetic induction which are essential in electric vehicles. The year of 1859 saw the development of the first Lead-acid battery by Belgian Gaston Plante. The Lead-acid battery is still used today as a starter battery in most internal combustion vehicles. Gustave Trouve of France, revealed the first electric vehicle in 1881. Trouve utilized the previously developed lead-acid battery to power a tricycle. The end of 1800's saw the development of nickel-iron battery by Thomas Edison. Although quite high in production cost, the nickel-iron battery was able to store 40% more energy per unit weight than the lead-acid battery. The same period saw the development of nickel-zinc and zinc-air batteries [11] [12].



Fig. 133. — TRICYCLE DE M. TROUVÉ.

Figure 2.2: First Electric Powered Vehicle [13]

2.1.2. 1900-1960

Known as the *golden age* of electrical vehicles (1880-1920), this period witnessed the advancement of electric vehicle technology. The technologies developed during this time allowed electric vehicles to compete with their gasoline and steam powered counterparts. The technological advancements were in fields such as battery development, battery charging technology and regenerative braking. Regenerative braking allows for the electric motor to act as a generator, converting portion of the car's kinetic energy back to electrical energy and storing it in the batteries.

This period also saw the development of electric-gasoline hybrid technology. This technology was advertised to provide electric-noiseless driving with no range anxiety. However this technology was phased out due mainly to cost issues and revisited later in

1970's. Improvements made to the internal combustion engine was the beginning of the *dark ages* for the electrical vehicle (1925-1960). The limited range and the inability to build EVs at a competitive price point were the main contributing factors for the effective disappearance of EVs from the market place [11] [12].

2.1.3. 1960-present

In the 1960's several car manufacturers such as Ford Motor Company and General Motors built prototypes of electric vehicles that never went into large scale production, such as the Ford *Comuta* pictured below:



Figure 2.3: Ford Comuta developed in 1967 [11]

However in the 1970's several factors encouraged more efforts to be placed on developing electric vehicles. These factors included more emphasis being placed on limitations and environmental impacts of fossil fuels, the oil embargo effectuated by major oil producers and the nuclear power debate. Furthermore local, federal and global regulations such as California's *zero emission* regulation and the *Kyoto Protocol* additionally advanced the global effort for advancements in electric vehicle technology. The US government started electrification initiatives at this time such as the introduction of the "Partnership for a New Generation of Vehicles", which resulted in three more electric vehicle prototypes at a price tag of one billion dollars with none of the vehicles ever going to production. Japanese manufacturers became hybrid front runners with Toyota releasing the *Prius* in 1997 and Honda releasing *Insight* in 2003. In 2004 the *Ford Escape* became the first American hybrid vehicle [11] [12].

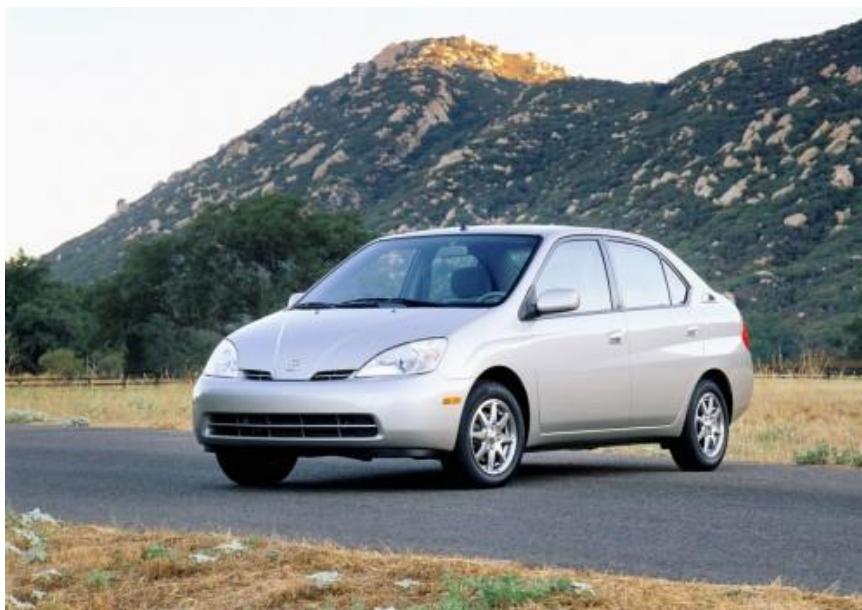


Figure 2.4: Toyota Prius 1997 [14]

Although presently commercially available, electric and hybrid-electric vehicles have failed to attract sufficient interest from consumers. This is due to issues such as size and cost of batteries, slow recharging times and range anxiety [11].

2.2. Energy Storage Candidates

In the context of global warming, electrical energy storage devices and batteries are critically important and can be used in applications ranging from transportation to localised urban electrical power generation and distribution. Batteries are able to store energy that is produced at times of either low requirement, low cost or from irregular sources. The stored energy can then be used at times of peak demand, high production cost or when there are no other viable generations means present [15]. A brief description of some of these energy storage devices is presented below:

- VI.** *Lead acid batteries:* Lead acid batteries are one the oldest and most popular energy storage devices due to their high reliability and low cost. However Low energy density, short cycle life and inability to work in low temperatures make lead acid batteries unsuitable for long term energy storage [15] .
- VII.** *Nickel cadmium batteries:* Nickel cadmium batteries are also popular due to their reliability and minimal need for care. Nonetheless issues associated with their cost and disposal impede their progress into the next generation of energy storage devices [15].
- VIII.** *Lithium-ion batteries:* Lithium-ion batteries first produced by Sony in 1990 have drastically improved over the last few decades. Improvements have been in terms of

energy density, cycle life and efficiency. Lithium-ion batteries have largely replaced bulkier less energy absorbing nickel cadmium batteries in electronic devices such as cellular phones and computers. Furthermore lithium-ion batteries are now used in electrical and hybrid electrical vehicles such as the Nissan Leaf and the Chevrolet Volt [15] [16].

- IX.** *Fuel Cells:* Some examples of current fuel cell technology include hydrogen fuel cells, direct-methanol fuel cells and molten carbonate fuel cells. Most fuel cell technologies are excellent at storing energy. Unfortunately, fuel cells suffer from high cost and low efficiency [15].
- X.** *Ultra-capacitors:* Ultra-capacitors are an excellent candidate for producing short term instantaneous power. In comparison to batteries, ultra-capacitors have much lower energy densities and much greater power densities. This relationship has encouraged further exploration into producing a battery/ultra-capacitor hybrid energy storage unit [15] [17].

Figure 2.5 provides a comparison in terms of specific energy and power density for storage devices.

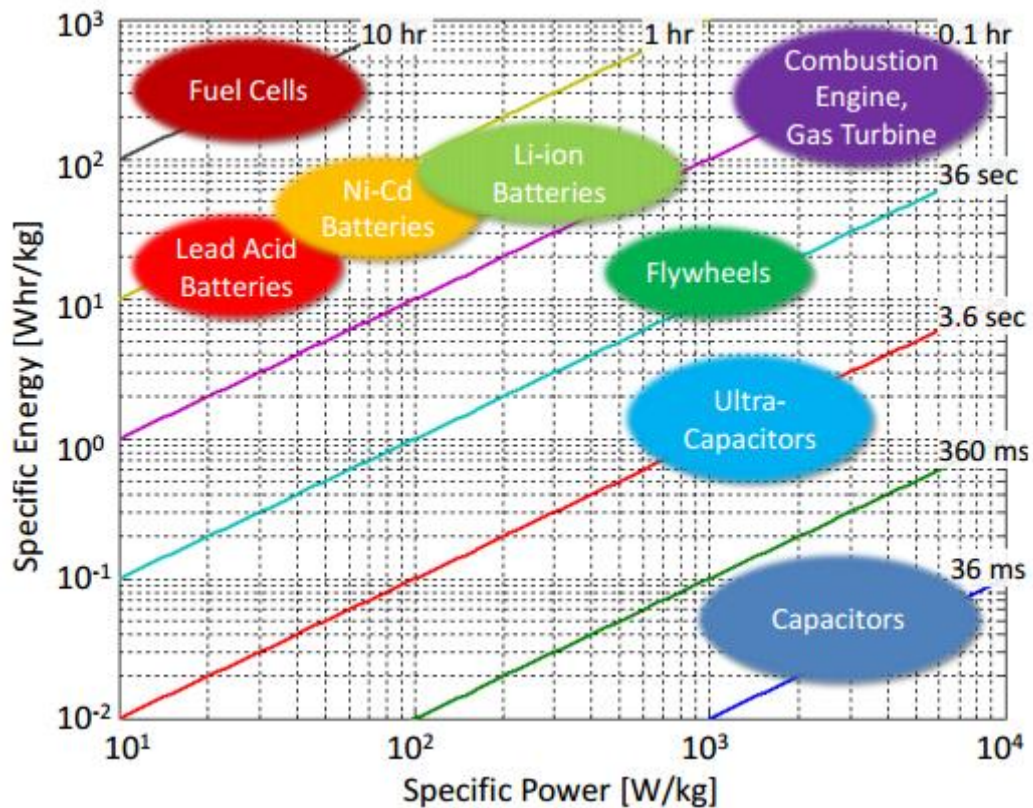


Figure 2.5: Ragone Plot of Energy Storage Devices [18]

2.3. Lithium-Ion Cell

A lithium-ion cell generally consists of an anode and cathode immersed in electrolyte solution and a separator. During charge, lithium ions as well as electrons move from the cathode to the anode. The medium for transportation of ions is provided by the electrolyte solution. The electrons however utilize current collecting plates at both electrodes in order to move through the external circuit. The purpose of the cell is to store electro-chemical energy during charge, and to release the stored charge during discharge. The components of a lithium-ion cell are explained in detail below and shown in Figure 2.6:

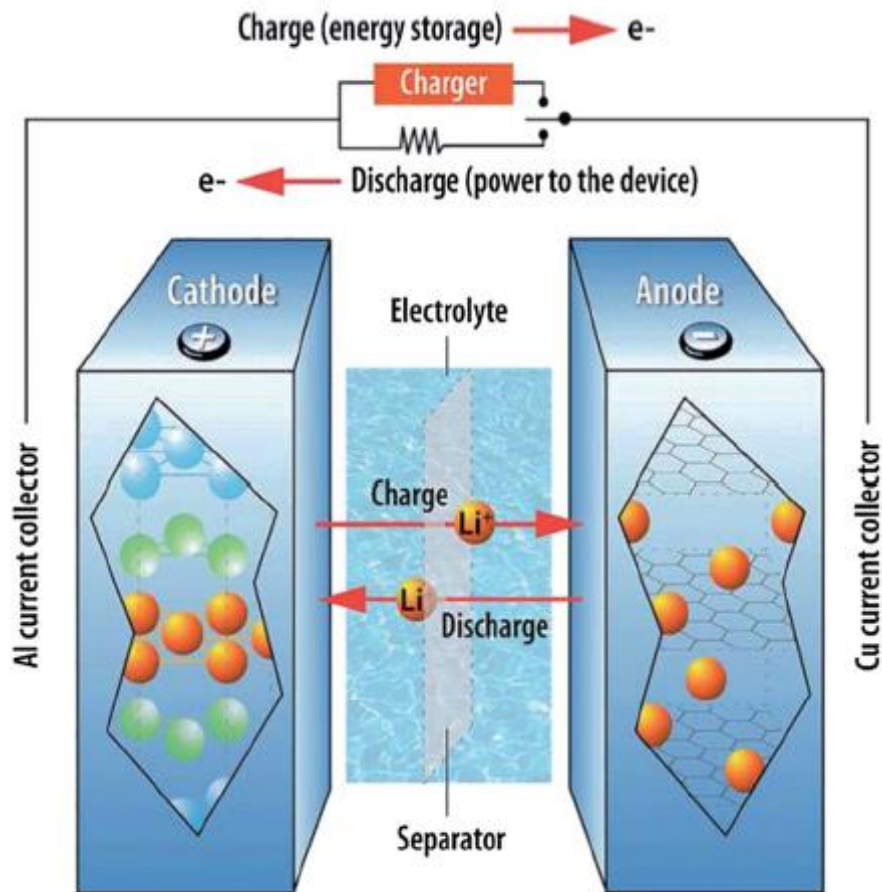


Figure 2.6: The components of a lithium-ion cell [19]

- XI.** *Cathode:* Layered structured lithium cobalt oxide, $LiCoO_2$ is the most prevalent cathode material used for Li-ion batteries. This structure although easy to prepare has a few shortcomings, mainly the relatively high cost and the environmental issues associated with it. Other compounds likely to replace cobalt for a given application include nickel, manganese and vanadium.
- XII.** *Anode:* A mixture of graphitic carbon (ex. LiC_6) is the most commonly used material in the negative electrode of lithium-ion batteries. The inclination to use this material is its low cost and low operational voltage. However low rate capabilities and

irreversible capacity losses are its limitations, prompting a search for finding a replacement anode material. Some materials under investigation include tin, silicon and indium. These materials offer better specific capacity, however under cyclic loading their particles experience successive cracking and eventual loss of contact between particles.

XIII. *Electrolyte:* The electrolyte solution separating the anode and cathode in lithium-ion batteries needs to possess several qualities. These qualities include high ion conductivity, low electrical conductivity and thermodynamic stability. Currently one or a combination of propylene carbonate, dimethyl-carbonate, ethylene carbonate and vinylene carbonate dissolved with electrolyte salts such as lithium perchlorate and lithium hexafluorophosphate are used to form the electrolyte solution [16] [19].

2.4. Battery Management Systems

Battery Management Systems (BMS) are typically used in consumer portable electronics, hybrid electrical vehicles and battery electric vehicles. BMS are responsible for communicating between the host device and the battery pack in order perform tasks such as cell balancing, control, thermal management and for State of Charge and State of Health estimation [20]. SOC and SOH are briefly discussed below:

- *State Of Charge:* State Of Charge represents the present battery capacity as a ratio of maximum capacity. SOC value of 1, signifies that the battery under study is fully charged and it is currently at the highest permissible voltage, conversely the value of 0 represents a battery that is fully discharged and is currently at the lowest permissible voltage (cut-off voltage). The most prominent method used to measure SOC is coulomb counting [21], which involves integrating current as demonstrated in Equation 2.1. Here SOC_0 is the initial State of Charge, C_n is the nominal capacity and I is the discharge current. Nominal capacity of a battery is equivalent to the total ampere hours it has available at a specific C-rate. C-rate is

a measure of rate of charge and discharge relative to maximum capacity. For instance if a battery has a nominal capacity of 10 ampere hours, for this battery 1C would be equivalent to 10 Amps. In using the coulomb counting method an initial value of SOC is necessary. Additionally this method is susceptible to accumulation of errors [22]. There are other methods available for State of Charge estimation [23], mainly using an estimation technique such as the extended Kalman filtering (EKF) [24] in conjunction with a mathematical model. Modeling techniques are discussed in the latter part of this chapter.

$$SOC = SOC_0 - \frac{1}{C_n} \int_{t_0}^t I d\tau \quad (2.1)$$

- *State Of Health*: SOH as demonstrated in Figure 2.7, is a measure of degradation of the battery. Key parameters associated with SOH include capacity fade and power fade. In HEV and BEV applications a battery is no longer usable when the battery has reached 80% of its maximum nominal capacity (capacity fade) or 80 % of its maximum rated power (power fade) [25]. There are various methods used in order to quantify SOH as a life fraction (LF) between 0 and 1 [26] [27] [28]. These methods include impedance spectroscopy, fuzzy logic methodology, Extended Kalman filtering for real time prediction and the use of a sliding mode observer [28].

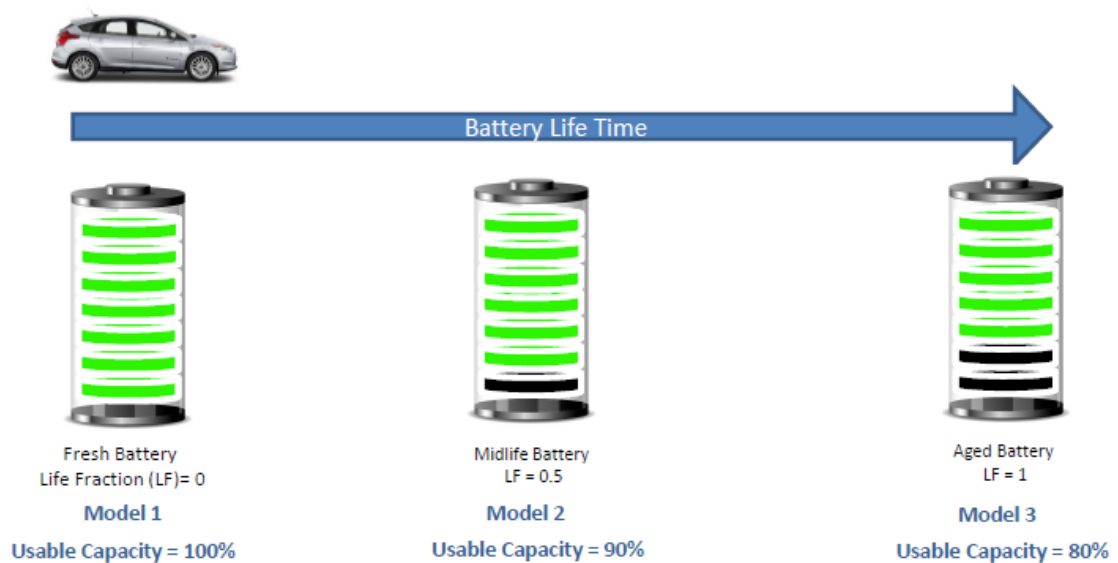


Figure 2.7: Battery State of Health for HEV applications [29]

There are many algorithms designed for SOH and SOC prediction, however HEV applications are known to impose harsh requirements on battery packs with C-rates of up to and surpassing 20C [2].

2.5. Battery Modeling

Battery Management Systems typically utilize battery models that possess several variables and parameters that are indicative of SOC and SOH, in addition to an estimation algorithm to monitor their values in real time. The accuracy of models impact the accuracy of estimation. Accurate values of SOC and SOH can be used to prolong battery life and enhance safety by preventing over-charge or over-discharge. It also allows BMS to get the maximum performance from the battery pack without causing damage [20]. There are different types of battery models including Lumped parameter models, equivalent circuit

models, electro-chemical models and impedance spectroscopy. The choice between the models is a trade-off between complexity, desired accuracy and computational requirements; generally models need to be sufficiently accurate, but not overly complicated in order for them to be embedded in microprocessors [30].

2.6. Equivalent Circuit Models

Equivalent circuit models utilize circuit elements such as resistors and capacitors in order to model the cell. The main advantage of this type of modeling is its computational simplicity [31]. Furthermore, this technique eliminates the need for understanding complex phenomena, as only a few variables need to be parameterized using experimental data. A total of six equivalent circuit models are selected from literature and discussed here. These models include the simple model, the first-order RC model, the second order RC model, the third-order RC model and hysteresis models. A more comprehensive list of equivalent circuit models can be found in reference [30].

2.6.1. The Simple Model

Typically equivalent circuit models capture the battery SOC and current dynamics. As presented in [2], the output equation in the simple battery model is divided into two parts; the first part is a function of the battery SOC and the second relates to battery terminal voltage.

$$z_{k+1} = z_k - \left(\frac{\eta_i \Delta t}{C_n} \right) i_k \quad (2.2)$$

$$y_k = OCV(z_k) - R i_k \quad (2.3)$$

Here OCV represents the open circuit voltage which is function of the State of Charge z_k , C_n is the battery nominal capacity, R is the cell internal resistance (different values may be used for charge/discharge), η_i is the charging and discharging efficiency and y_k is the terminal voltage. OCV is the voltage between the battery terminals when there is no load applied. In contrast y_k is the voltage between battery terminals when there is a load applied.

2.6.2. The First-Order RC model

The first-order RC model is the simplest of the RC equivalent circuit models. It consists of a resistor in series with an RC pair in parallel. The system and measurement equations are summarized by the following two equations [32]:

$$\begin{bmatrix} V_{k+1} \\ z_{k+1} \end{bmatrix} = \begin{bmatrix} 1 - \frac{\Delta t}{R_1 C_1} & 0 \\ 0 & 1 \end{bmatrix} \begin{bmatrix} V_k \\ z_k \end{bmatrix} + \begin{bmatrix} \frac{\Delta t}{C_1} \\ -\frac{\eta_i \Delta t}{C_n} \end{bmatrix} i_k \quad (2.4)$$

$$y_k = OCV(z_k) - R_0 i_k - V_k \quad (2.5)$$

Here the Ohmic resistant elements are summarized into $(R_0 i_k)$ and the faradic non-linear elements are lumped into the RC pair [31]. The voltage drop across the RC pair is represented by V_k , as shown in Figure 2.8

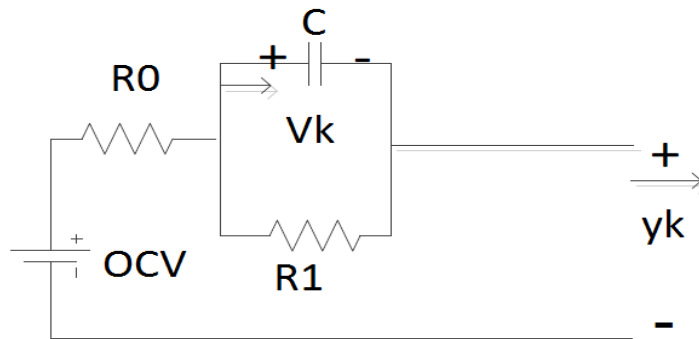


Figure 2.8: Schematic drawing of the First-Order RC model

2.6.3. The Second-Order RC Model

The second-order RC model expands on the first order model. The polarization characteristics previously only represented by V_k in the first order model, is broken down to electro-chemical polarization ($V_{1,k}$) and concentration polarization ($V_{2,k}$) [33]. The second-order RC model is shown in Figure 2.9.

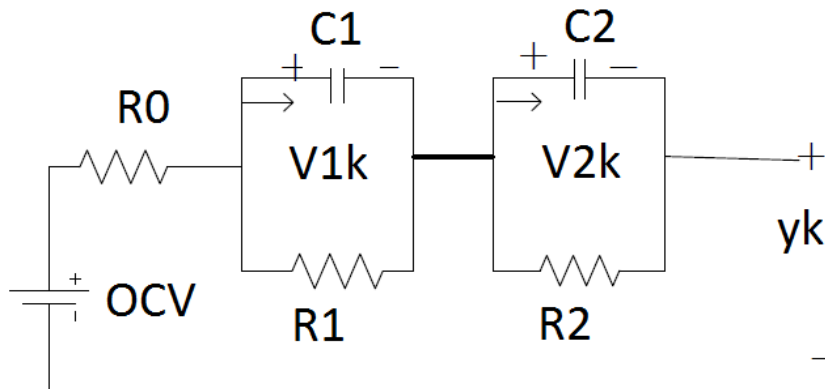


Figure 2.9: Schematic drawing of the Second-Order RC model

$$\begin{bmatrix} V_{1,k+1} \\ V_{2,k+1} \\ z_{k+1} \end{bmatrix} = \begin{bmatrix} 1 - \frac{\Delta t}{R_1 C_1} & 0 & 0 \\ 0 & 1 - \frac{\Delta t}{R_2 C_2} & 0 \\ 0 & 0 & 1 \end{bmatrix} \begin{bmatrix} V_{1,k} \\ V_{2,k} \\ z_k \end{bmatrix} + \begin{bmatrix} \frac{\Delta t}{C_1} \\ \frac{\Delta t}{C_2} \\ -\frac{\eta_i \Delta t}{C_n} \end{bmatrix} i_k \quad (2.6)$$

$$y_k = OCV(z_k) - Ri_k - V_{1,k} - V_{2,k} \quad (2.7)$$

2.6.4. The Third-Order RC Model

The third-order RC model further divides polarization characteristics (V_k) into $V_{1,k}$, $V_{2,k}$ and $V_{3,k}$ [33].

$$\begin{bmatrix} V_{1,k+1} \\ V_{2,k+1} \\ V_{3,k+1} \\ z_{k+1} \end{bmatrix} = \begin{bmatrix} 1 - \frac{\Delta t}{R_1 C_1} & 0 & 0 & 0 \\ 0 & 1 - \frac{\Delta t}{R_2 C_2} & 0 & 0 \\ 0 & 0 & 1 - \frac{\Delta t}{R_3 C_3} & 0 \\ 0 & 0 & 0 & 1 \end{bmatrix} \begin{bmatrix} V_{1,k} \\ V_{2,k} \\ V_{3,k} \\ z_k \end{bmatrix} + \begin{bmatrix} \frac{\Delta t}{C_1} \\ \frac{\Delta t}{C_2} \\ \frac{\Delta t}{C_3} \\ -\frac{\eta_i \Delta t}{C_n} \end{bmatrix} i_k \quad (2.8)$$

$$y_k = OCV(z_k) - Ri_k - V_{1,k} - V_{2,k} - V_{3,k} \quad (2.9)$$

The models discussed can further be completed by considering phenomena such as hysteresis and adding states accordingly. Hysteresis takes into account the difference between charging and discharging characteristics of the cell. The term $h(z, t)$ can be used to model hysteresis voltage. Equation for hysteresis voltage is shown below:

$$\frac{dh(z, t)}{dz} = \gamma \text{sgn}(\dot{z}) [M(z, \dot{z}) - h(z, t)] \quad (2.10)$$

Here M is the maximum polarization resulting from hysteresis, $\text{sgn}(\dot{z})$ is used to distinguish between charging and discharging and γ represents rate of voltage decay. The system and state equations for the simple model with one-state hysteresis is shown below [33]:

$$\begin{bmatrix} h_{k+1} \\ z_{k+1} \end{bmatrix} = \begin{bmatrix} F(i_k) & 0 \\ 0 & 1 \end{bmatrix} \begin{bmatrix} h_k \\ z_k \end{bmatrix} + \begin{bmatrix} 0 & 1 - F(i_k) \\ -\frac{\eta_i \Delta t}{C_n} & 0 \end{bmatrix} \begin{bmatrix} i_k \\ M(z, \dot{z}) \end{bmatrix} \quad (2.11)$$

$$y_k = OCV(z_k) - R_0 i_k + h_k \quad (2.12)$$

Where $F(i_k) = \exp\left(-\left|\frac{\eta_i i(t) \gamma}{C_n}\right|\right)$

2.7. The Electro-Chemical Model

Although equivalent circuit models are popular in battery management systems due to their simplicity, their validity and accuracy is a concern in the automotive context. The accuracy of equivalent circuit models can be enhanced at the cost of complexity (i.e. taking into account thermal effects). Electro-chemical models are more accurate and have the added advantage of possessing parameters with physical interpretation [34]. Of importance to the automotive field where batteries experience high current and energy loads, ECM are able to anticipate cell limitations [35].

The literature on electro-chemical models is comprised of simplified and full order models. The porous electrode theory [36] [37] is a popular modeling approach. This theory considers the electrode as a group of spherical particles where the surface of particles provides the route for lithium ions to diffuse and react. Furthermore the electrolyte solution is treated as a different medium where diffusion and reactions take place. This approach is demonstrated in Figure 2.10 and the governing formulas are as follows [38]:

$$\nabla_x K^{eff} \nabla_x \phi_e + \nabla_x K_D^{eff} \nabla_x \ln C_e = -J^{Li} \quad (2.13)$$

$$\nabla_x \sigma^{eff} \nabla_x \phi_s = J^{Li} \quad (2.14)$$

$$\frac{d\varepsilon_e c_e}{dt} = \nabla_x (D_e^{eff} \nabla_x c_e) + \frac{1-t^0}{F} J^{Li} \quad (2.15)$$

$$\frac{dc_s}{dt} = \nabla_r (D_s \nabla_r c_s) \quad (2.16)$$

$$J^{Li}(x) = a_s j_0 \left[\exp\left(\frac{\alpha_a F}{RT} \eta\right) - \exp\left(-\frac{\alpha_c F}{RT} \eta\right) \right]$$

$$V = \phi_s(x=L) - \phi_s(x=0) - R_f I \quad (2.17)$$

$$\eta = \phi_s - \phi_e - U(C_{se})$$

Here Equation 2.13 describes electrolyte potential distribution and Equation 2.14 describes solid potential distribution. Furthermore Equation 2.15 describes linear lithium diffusion in electrolyte and Equation 2.16 describes spherical solid diffusion. Finally the Butler-Volmer current density Equation 2.17 provides a link to external connections. Equation 2.17 can be used in order to determine terminal voltage and SOC. The complete set of nomenclature for the above equations is summarized in table 2.1.

Table 2.1: ECM model nomenclature

Symvbol	Name	Unit
K^{eff}	Effective phase ionic conductivity	$\Omega^{-1} cm^1$
ϕ_e	Electrolyte potential	V
K_D^{eff}	Effective electrolyte phase diffusion conductivity	$\Omega^{-1} cm^1$
J^{Li}	Butler_Volmer current density	$A cm^{-3}$
σ^{eff}	Effective conductivity of solid active material	$\Omega^{-1} cm^1$
ϕ_s	Solid potential	V
c_e	Electrolyte concentration	$mol cm^{-3}$
ε_e	Electrolyte phase volume fraction	-
D_e^{eff}	Effective electrolyte phase diffusion coefficient	$cm^2 s^{-1}$
F	Faraday's number	$C mol^{-1}$
t^0	Transference number	-
c_s	Solid concentration	$mol cm^{-3}$
D_s	Solid phase diffusion coefficient	$cm^2 s^{-1}$
a_s	Active surface area per electrode unit volume	cm^{-1}
α_a, α_c	Change transfers coefficients	-
R	Gas constant	$JK^{-1} mol^{-1}$
T	Temperature	K
R_f	Film resistance on the electrodes surface	V
η	Overpotential	V
U	Open circuit voltage	V
A	Electrode plate area	cm^2
C_{se}	Solid concentration at electrolyte interface	$mol cm^{-3}$
I	Battery Current	A

Use of partial differential equations renders this model extremely complex, and almost impractical to use in a real-time controller. Hence various approximation Techniques have been applied, in order to reduce model complexity. Assumptions commonly used for simplifying the model complexity found in literature include:

- I.** Assuming the electrolyte concentration to be uniform and therefore reducing $C_e(x,t)$ to C_e [35] [39].
- II.** Assuming a solution of micro-current density.
- III.** Approximating spherical diffusion using pade approximation [40], parabolic profile approximation [41], and look-up tables [25] [42].

Simplifications one and two eliminate Equation 2.15 and make the following changes to the rest of the Equations:

$$\nabla_x K^{eff} \nabla_x \phi_e = -J^{Li} \quad (2.18)$$

$$\nabla_x \sigma^{eff} \nabla_x \phi_s = J^{Li} \quad (2.19)$$

$$\frac{dc_s}{dt} = \nabla_r (D_s \nabla_r c_s) \quad (2.20)$$

$$J^{Li} = 1/A\eta$$

$$\eta = \phi_s - \phi_e - U(C_{se}) \quad (2.21)$$

$$V = \phi_s(x = L) - \phi_s(x = 0) - R_f I$$

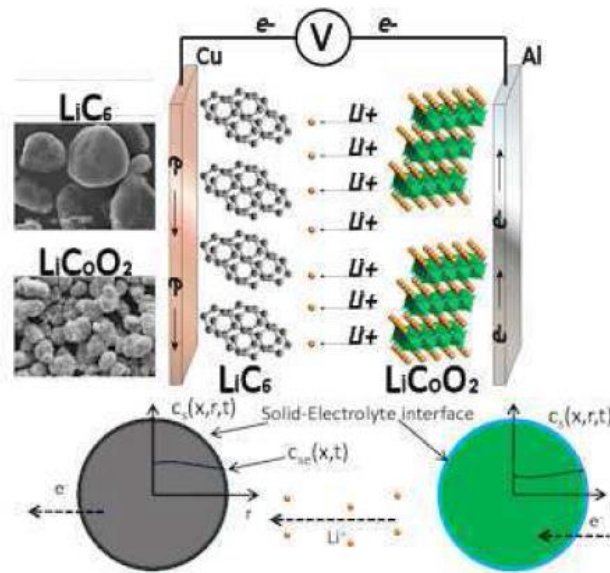


Figure 2.10: Micro-Macro cell model [43]

There are several studies done in order to study thermal effects from the electro-chemical phenomena taking place inside a battery [44] [45]. These models usually use additional parameters such as entropy change, ohmic loss and over potentials into account [46].

2.8. Electro-chemical Impedance Spectroscopy

The lithium-ion battery is host to multiple processes such as charge transfers, energy transfers and electro-chemical reactions. One method to quantify these processes is through electro-chemical Impedance spectroscopy (EIS) [47]. The EIS method involves applying a sinusoidal input to the cell and collecting the characteristic response from the cell (cell impedance). It is possible for the input to be either current (galvanostatic), or voltage (potentiostatic). The governing equation for the EIS method is as follows [48]:

$$Z = \frac{u(t)}{i(t)} = \frac{U * \sin(\omega t)}{I * \cos(\omega t - \phi)} = |Z| * \frac{\sin(\omega t)}{\cos(\omega t - \phi)} \quad (2.22)$$

where I is amplitude of the current signal, U is the amplitude of the voltage signal, ϕ is the phase shift between the two signals and Z is the impedance of the cell. In order to form the Nyquist plot, the impedance is separated into a real part Equation 2.23 and an imaginary part Equation 2.24 as follows:

$$Z' = |Z| * \cos(\phi) \quad (2.23)$$

$$Z'' = |Z| * \sin(\phi) \quad (2.24)$$

where $|Z|$ is the absolute value of impedance. The primary tool used for EIS analysis is the Nyquist plot shown in Figure 2.11. However Nyquist plots have the disadvantage of not being able to identify the frequency of measurement, for a particular point. This drawback can be overcome by using Bode plots.

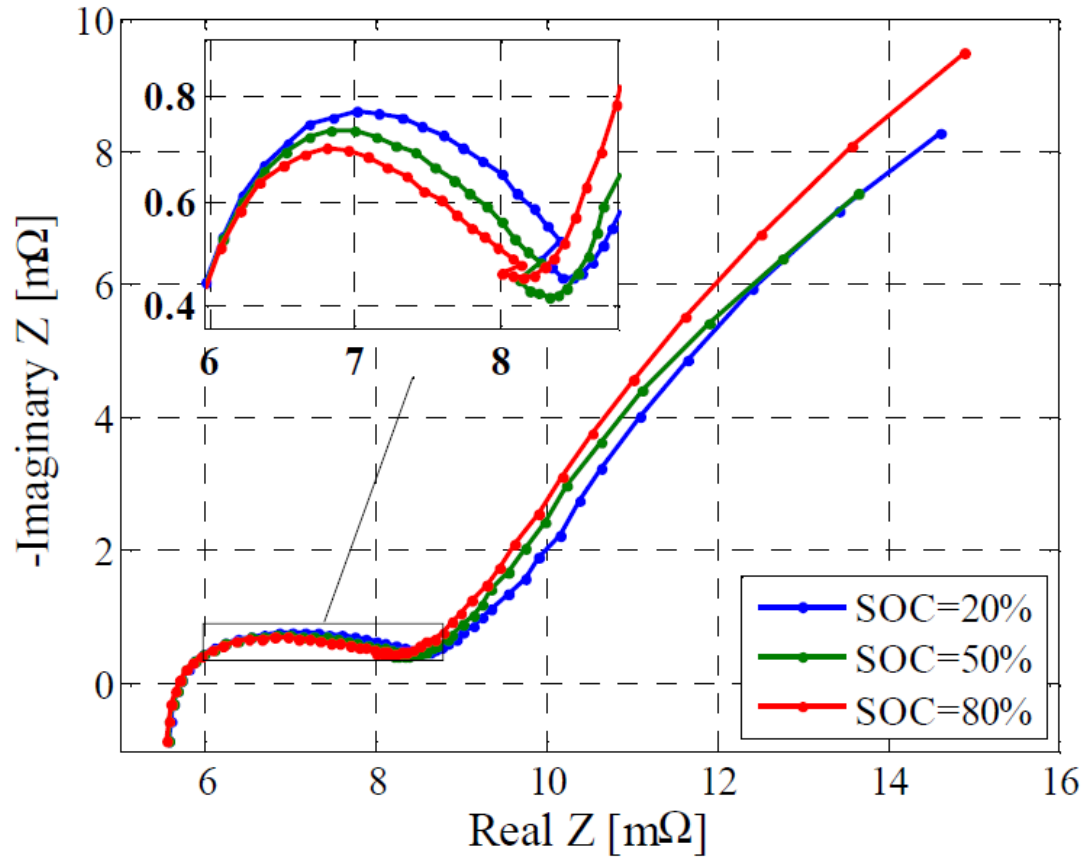


Figure 2.11: EIS pattern of a lithium-ion cell [49]

The general shape of EIS spectra follows that of Figure 2.11, however there are changes that happen due to changes in SOC and SOH. For instance the first semi-circle decreases in size as a result of increase in SOC levels as seen in the magnified portion of Figure 2.11. The reduction in size of the first semi-circle is due to decreasing of the cell polarization resistance with increasing states of charge. Furthermore the EIS spectra also varies as the cell ages. It is observed from Figure 2.12 that, as the cell ages the EIS spectra is shifted to the right side of the Nyquist plane. This shift is primarily due to increases in the ohmic resistance as the cell ages [49]. Temperature also has a dramatic impact on the impedance spectra as demonstrated in Figure 2.13. The effect of change in ambient temperature on the cell spectra is mainly

observed in the charge transfer loop, as low temperatures slow down the electro-chemical reactions and increase internal resistance of the cell causing the spectra to shift to the right. Worth mentioning is the fact that changes due to temperature are fully reversible, and changes in ambient temperature do not permanently improve or degrade a battery cell [50]. The experimental EIS data can be fitted into models that incorporate parameters such as electrolyte resistance, polarization resistance, charge transfer resistance, diffusion and coating capacitance [51].

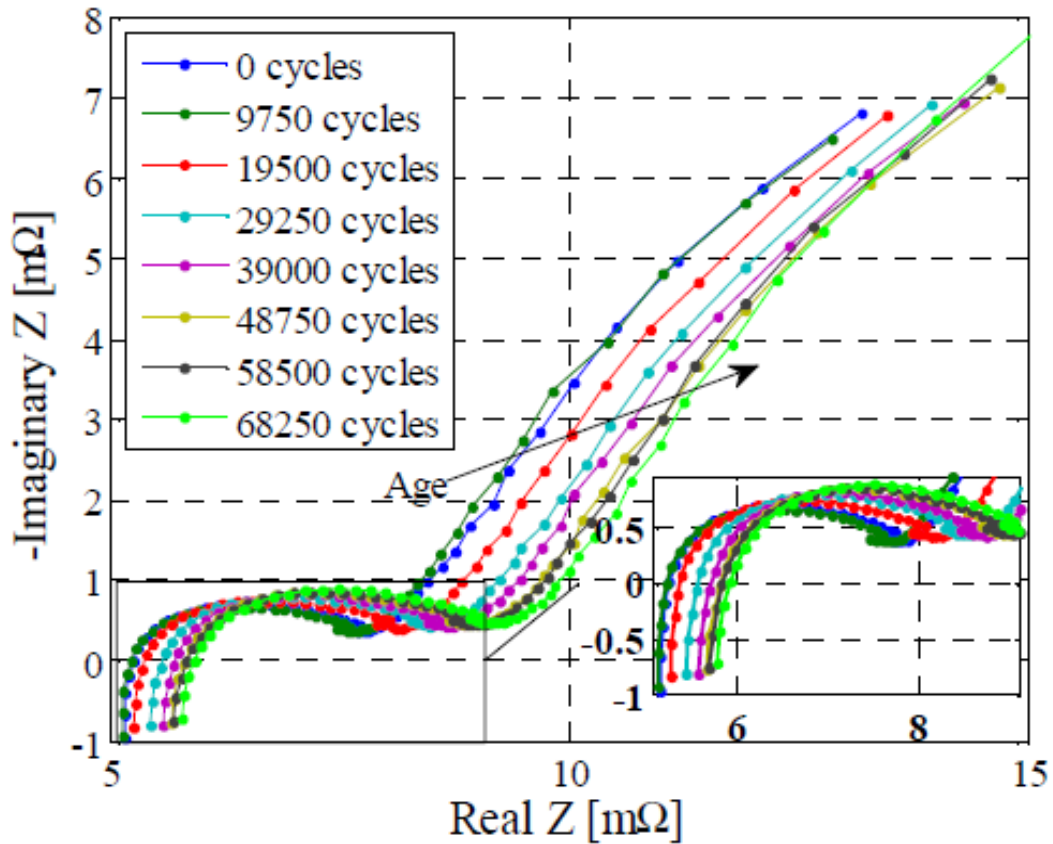


Figure 2.12: Change of EIS spectra during lithium-ion cell life span [49]

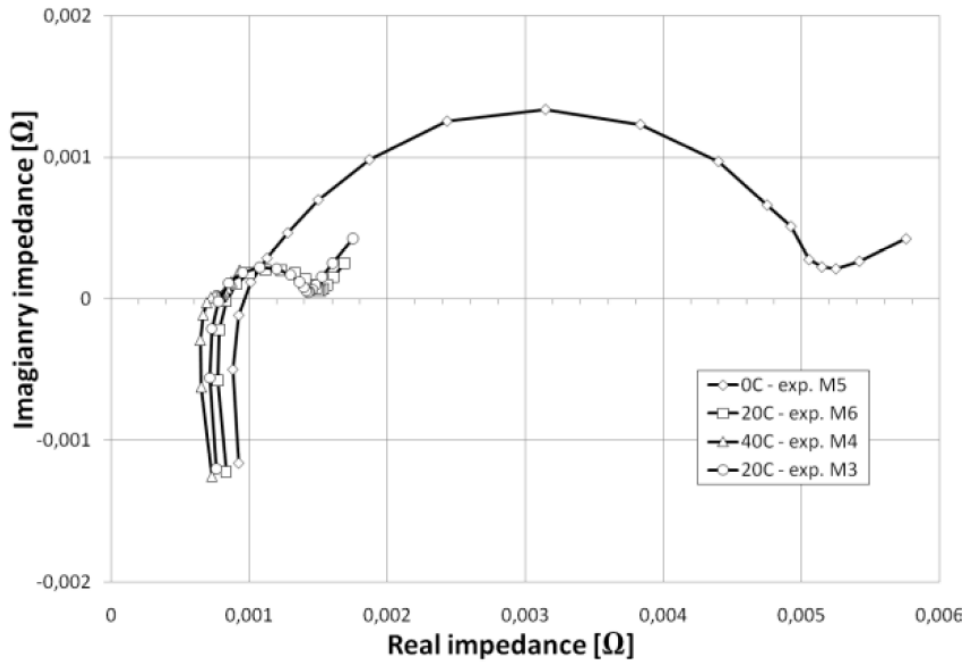


Table 1: EIS Test matrix

Test #	Current [A]	Temperature [°C]
M1	5 (C8)	Amb. (20)
M2	2 (C20)	Amb. (20)
M3	10 (C4)	20
M4	10 (C4)	40
M5	10 (C4)	0
M6	10 (C4)	20

Figure 2.13:Effect of Ambient Temperature in a Battery spectra at 50% SOC [50]

2.9. The EIS Model

Equivalent circuit models can also be utilized in order to represent battery internal dynamics as a function of frequency. The cell dynamics can be sub-categorized into charge-

transfer reaction on electrode/electrolyte interface, lithium-ion diffusion in electrode, double layer effects and the resistance/capacitance growth of the anode insulating film [52]. In this study, the Randles model is considered. This model is comprised of a resistor in series with a RC circuit and a Warburg element as shown in Figure 2.14. In this model diffusion characteristics are represented by the Warburg element, ohmic resistance is represented by the resistor and the RC element represents the double layer effect as follows.

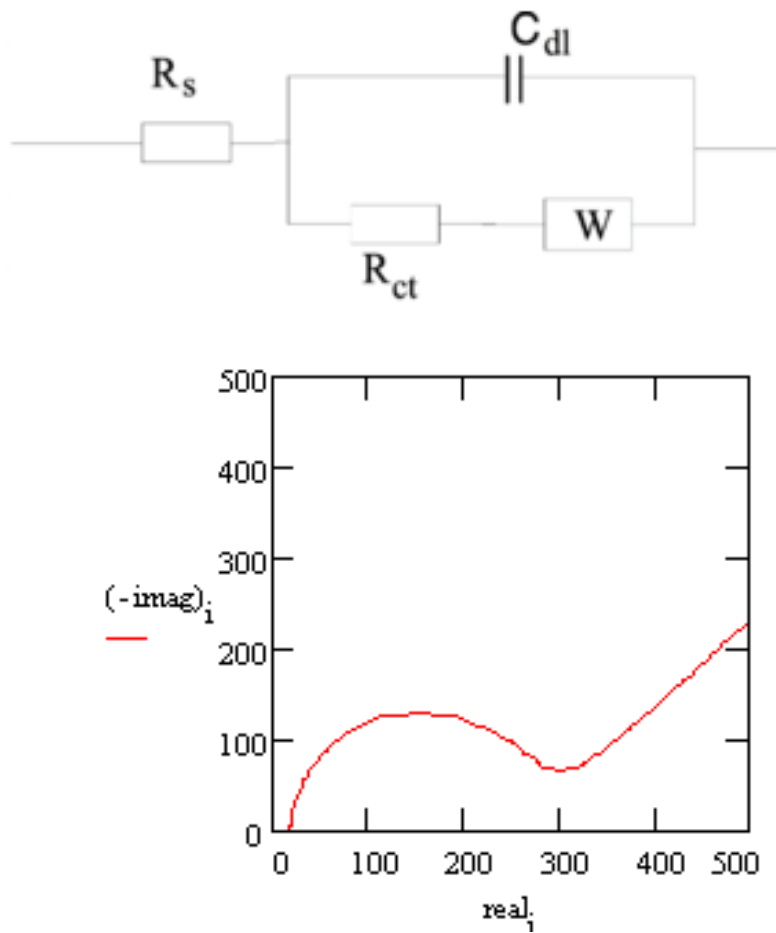


Figure 2.14: Randles Cell [53]

The Different elements of the Randle Circuit are discussed below :

- *Mass Transport Effects:* Diffusion and migration are the two primary modes by which ions transport through the cell. Diffusion is caused by the presence of a concentration gradient. Furthermore diffusion can occur within the free electrolyte, porous electrode and active mass as show in Figure 2.15. Mass transport effects can typically be observed at low frequencies ($f < 1\text{Hz}$). In EIS modeling, the Warburg element is typically employed to describe mass transport effects. The Impedance for the Warburg element is given by:

$$Z_W = \frac{\sigma}{\omega^{\frac{1}{2}}} - j \frac{\sigma}{\omega^{\frac{1}{2}}} \quad (2.25)$$

where σ is the Warburg coefficient and ω is the angular frequency.

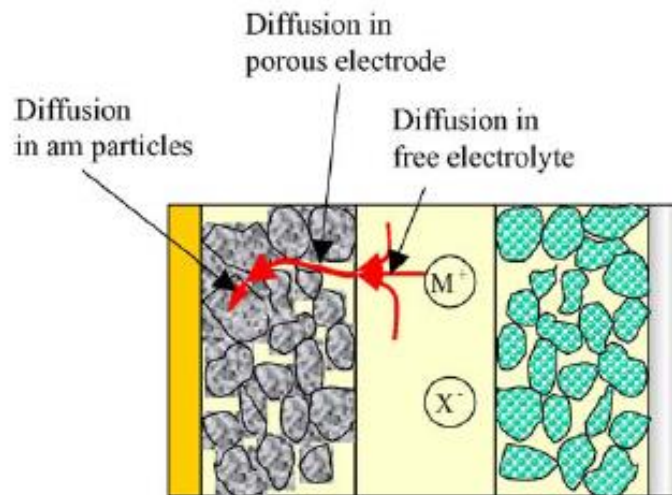


Figure 2.15: Diffusion processes in a battery [54].

- *Double Layer Effect:* The space between the electrode and electrolyte is location for the formation of a charged zone. This phenomena is induced due to the short distance and large surface in porous electrodes. Similar to a capacitor charge is stored in the charged zone within moments of application of a charge pulse, and discharged as the charge pulse is lowered or stopped. R_{CT} and C_{DL} are used to model Double-layer effects, where R_{CT} represents the resistor and C_{DL} represents the capacitor shown in Figure 2.14. Worth mentioning is that R_{CT} and C_{DL} are not constants and their values are dependent on current, SOC, SOH and temperature. The impedance of R_{CT} and C_{DL} is given by

$$Z_{R_{CT}/C_{DL}} = \frac{R_{CT}}{(1 + R_{CT}^2 + C_{DL}^2) * \omega^2} - j \frac{R_{CT}^2 * C_{DL} * \omega}{(1 + R_{CT}^2 + C_{DL}^2) * \omega^2} \quad (2.26)$$

- *Electric and magnetic effects:* The resistance induced by the electrolyte, current collecting plates, active mass and transition between active mass and current collector are summed up and simply represented by ohmic resistance R_S . In agreement with Ohm's law the voltage at the ohmic resistance follows the battery current [54].

Finally real and imaginary impedance components resultant from mass transport effects, double layered effects and electric and magnetic effects are summed up and demonstrated below:

$$Z_{REAL} = R_S + \frac{R_{CT}}{(1 + R_{CT}^2 + C_{DL}^2) * \omega^2} + \frac{\sigma}{\omega^{\frac{1}{2}}} \quad (2.27)$$

$$Z_{RCT/CDL} = -j \frac{R_{CT}^2 * C_{DL} * \omega}{(1 + R_{CT}^2 + C_{DL}^2) * \omega^2} - j \frac{\sigma}{\omega^{\frac{1}{2}}} \quad (2.28)$$

2.10. Industry Cell Testers

Battery testing equipment is required in order to obtain the experimental results that are essential in parameterizing several battery models, some of which were previously discussed in this chapter. This equipment is supplied from various manufacturers and come with a range of capabilities based on application. Table 2.2 summarizes findings from examining various manufacturer catalogues with the aim of finding a tester with the dual capability of obtaining characterization results as well as high frequency results. In order to conduct high frequency tests without aliasing, a tester must possess relatively high sampling rate (i.e.50 KHz). The tester also needs to provide sufficient voltage and current capabilities (i.e. $\pm 5V$ and $\pm 50A$) in order to carry out characterization tests. As presented in Table 2.2, the reader was unable to find a tester able to provide both capabilities.

Table 2.2: Specifications of the Battery Tester

Manufacturer	Model Number	Voltage Capability	Current Capability	Max Sampling Rate
Arbin	BT-5HC	0-5V	Up to 2000A	1Hz
Maccor	Series 3600	0-5V	Up to 2.5 A	200Hz
CADEX	C8000	0-45V	Up to 10 A	20 KHZ
Gammry	Interface 1000	±12V	Up to 1 A	1 MHZ

2.11. Summary

Energy storage devices are of paramount importance in sustaining the needs of future generations. Lithium-ion cells are able to produce sufficient energy and power for vehicular applications. The safety, performance and longevity of lithium-ion cells is based in parts by their operation and control strategy, or their BMS. BMS in turn requires knowledge of SOC and SOH, which can be estimated using model base estimation. Battery modeling techniques

include equivalent circuit models, electro-chemical models and electro-chemical impedance spectroscopy.

Chapter 3

Design of a Lithium-ion Cell Tester

In order for Battery Management Systems (BMS) in EVs to be able to accurately predict SOC and SOH, accurate models are required. Battery models need to be parameterized using laboratory data. Once a battery model is constructed, further testing needs to be conducted for model validation. The experimental data therefore must be collected in an accurate, precise and safe manner. Different modeling strategies require different testing capabilities. Cycle Characterization results for example, requires a tester to be able to apply and collect data from a predefined cycle. High frequency characterization results require similar capabilities with the addition of high frequency sampling (i.e. 50 KHZ) capability. The ability for a tester to conduct both tests saves time and money which are valuable resources in battery research and development.

Literature review in Chapter 1 revealed the needs for a tester with dual capabilities of cycle characterization and high frequency characterization that does not currently exist. The aim of this chapter is to demonstrate the development of a lithium-ion cell tester with dual capabilities. This chapter highlights the key components of the developed tester as well as the safety circuit designed to keep cell operational within cell manufacturer safety limits.

3.1. Battery Tester Specifications

Specification for a battery tester is influenced by the cell chemistries and application domain. For instance, a tester should be capable to operate within the full voltage range of the cells it is intended to test. The battery used for this research is a lithium iron phosphate cell used for automotive applications. The required specifications for tester based on cell attributes are listed in Table 3.1. Each item represented in Table 3.1 imposes a requirement on the testing equipment. The charging and discharging specifications requires the tester to be able to supply up to 4.2 V and 86.4A. The operating temperature specification requires the environmental chamber to be able to modulate temperature between -20°C to 60°C. Finally the frequency specification requires the data acquisition software and hardware to be able to supply and collect data at 10KHz. This frequency is chosen in order to obtain the high frequency region of the EIS spectra. Sampling capability of the data acquisition should be sufficiently high in order to avoid aliasing.

Table 3.1: Specifications of the Battery Tester based on a lithium iron Phosphate Cell

Item	Specification	
Charging(continuous)	Voltage	4.2V
	Current	16.2A(3C)
Discharging(continuous)	Voltage	2.8V
	Current	86.4A(16C)
Operating Temperature	Charging	0 ~ 45°C
	Discharging	-20 ~ 60°C
Sampling Frequency (max)	Charge/Discharge	100KHz
Operating Frequency(max)	Charge/Discharge	10KHz

3.2. Battery Tester Components

The battery tester circuit architecture is demonstrated in Figure 3.1. The components of the tester include a battery holder, power supply, data acquisition chassis, data acquisition modules, an environmental chamber, a current sensor, thermocouples and a safety circuit. The setup is demonstrated in Figure 3.2 and more information is provided in Appendix A.

3.2.1 Battery Holder

The battery holder is intended to enclose the battery and three thermocouples, as shown in Figure 3.3. It is made up of three materials that include copper for conductivity, fibre glass for electrical insulation and stainless steel for strength.

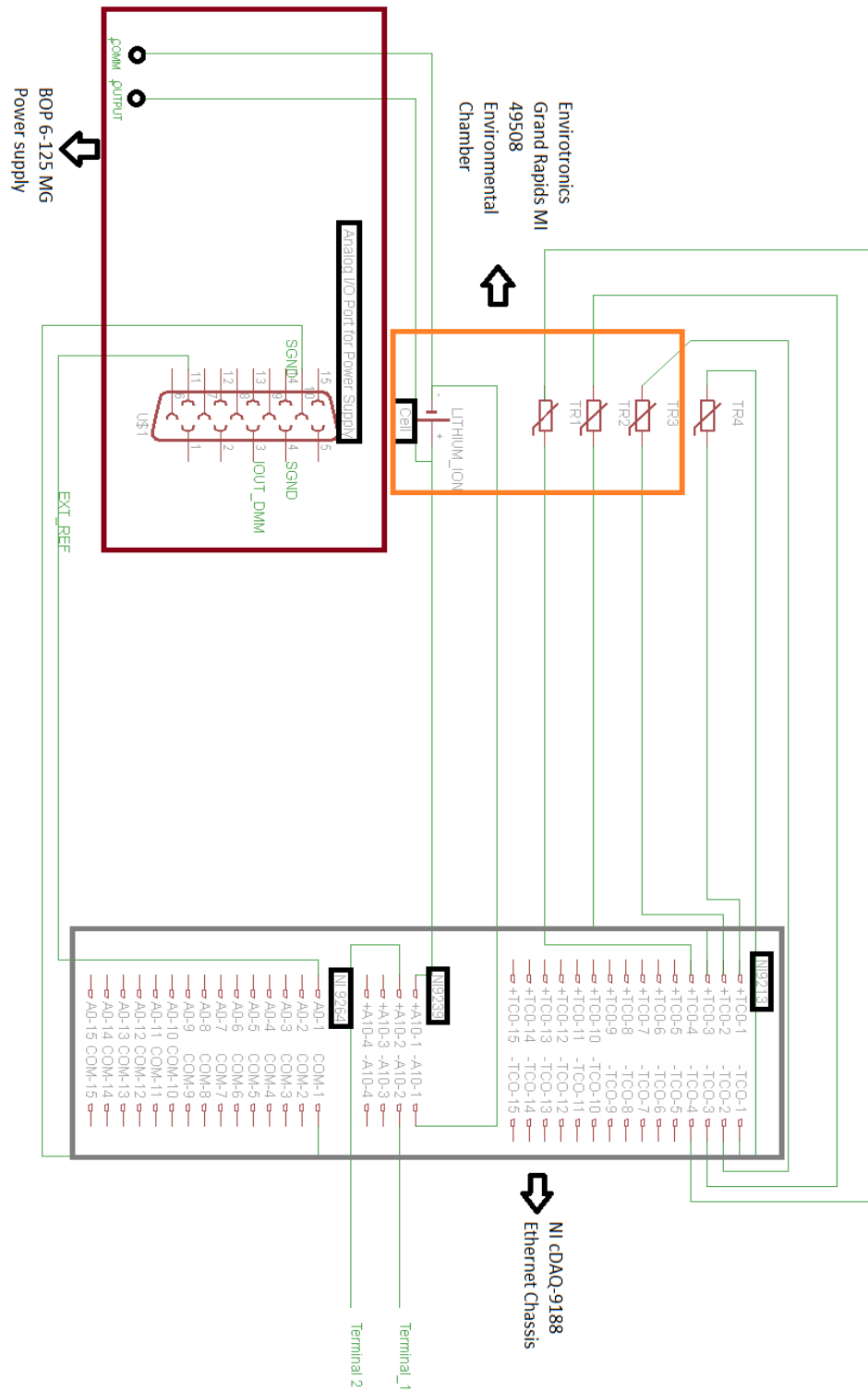


Figure 3.1: Tester Circuit Architecture



Figure 3.2: The Experimental Setup

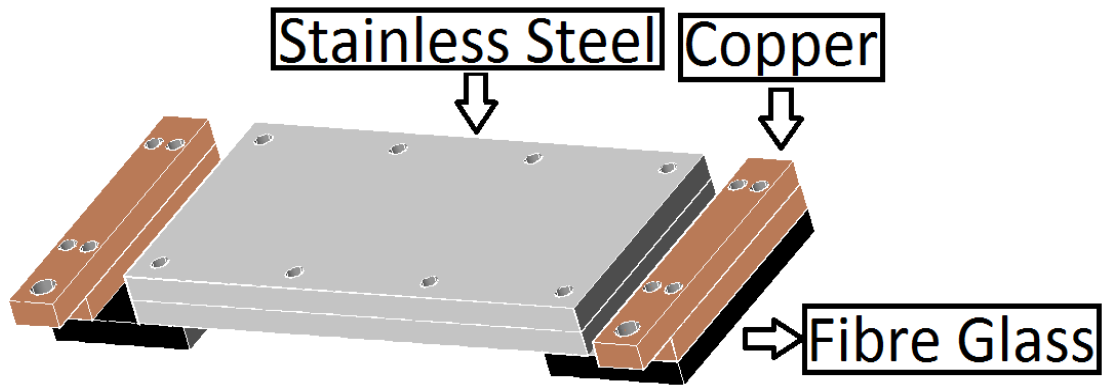


Figure 3.3: Battery Holder Materials

3.2.2. Power Supply

The power supply is able to provide $\pm 6V$ and $\pm 150 A$. It is connected directly to the battery cell for charging and discharging. It is controlled from LabVIEW software on a computer via three connections. The analog I/O port of the power supply is connected to an analog output module (NI 9264), subsequently the analog output module is connected to the chassis (NI cDAQ 9188) which in turn is connected to a computer using an Ethernet cable. The power supply connections are demonstrated in Figure 3.4.

3.2.3. Data Acquisition Chassis

The NI cDAQ-9188 is an 8-slot Ethernet chassis capable of measuring up to 256 channels. Seven I/O modules with integrated signal conditioning can be operated simultaneously using this chassis.

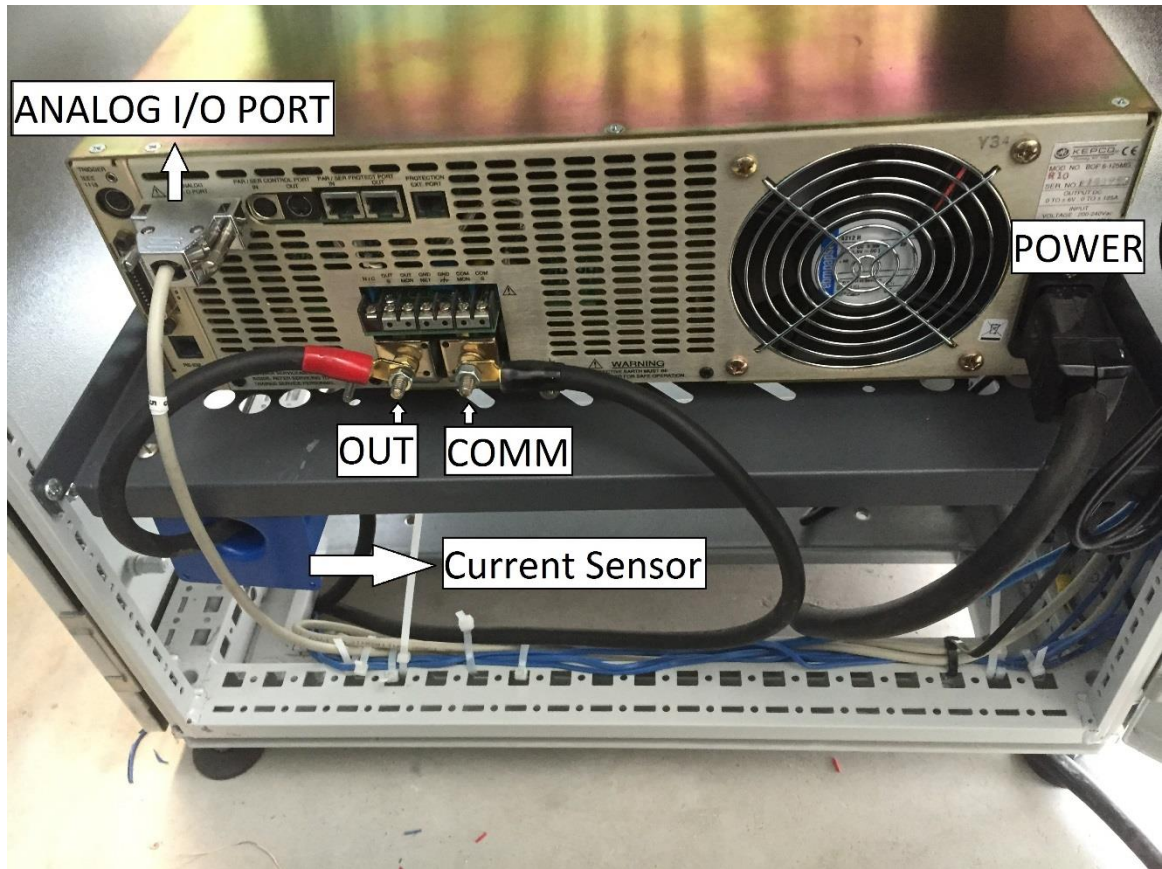


Figure 3.4: Power Supply Connections

3.2.4. Data Acquisition Modules

The Modules used for this project include the following:

- *NI 9213*: A 16 channel thermocouple input module capable of 75 samples per second. This module supports type J, K, T, E, N, B, R and S thermocouples.
- *NI 9264*: A 16 channel analog output module capable of 25 Kilo samples per second with 16 bit resolution and $\pm 10V$ output range.
- *NI 9239*: A 4 channel simultaneous analog input module capable of 50 Kilo samples per second with 24 bit resolution.

- *NI 9205*: A 32 channel analog input module capable of 250 Kilo samples per second with 16 bit resolution. The input range can be programmed to be set at $\pm 10V$, $\pm 5V$, $\pm 1V$ and $\pm 0.2V$.

3.2.5. Environmental Chamber

The Envirotronics Grand Rapids 49508 is a temperature only environmental chamber capable of varying temperature between $-66^{\circ}C$ to $177^{\circ}C$. The work space inside the chamber is equivalent to 8 cubic feet and it utilizes two, 2.5Hp compressors in order to vary temperature.

3.2.6. Current Sensor

The LEM IT 200-S ULTRASTAB is a high accuracy current measurement device. This device scales down current with a ratio of 1:1000. A Printed Circuit Board (PCB) was developed in order to connect the 9 pin output connector of this device to the data acquisition system. The schematic diagram for the current sensor PCB is shown below:

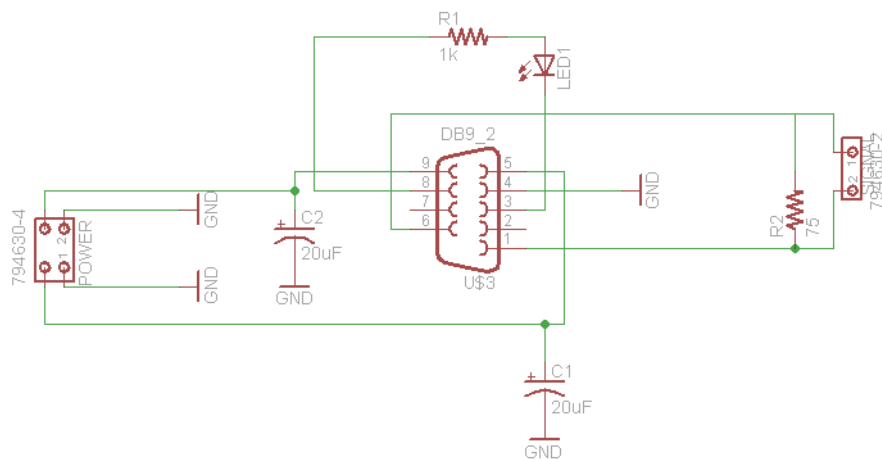


Figure 3.5: Current sensor PCB diagram



Figure 3.6: Current Sensor PCB

3.2.7. Thermocouples

Total of four Omega type-T thermocouples were utilized in order to monitor and record temperature. Three of those thermocouples were inserted into thermocouple insertions sites in the battery holder as seen in Figure 3.7 and one thermocouple was used in order to monitor and record temperature inside the environmental chamber in Figure 3.8.

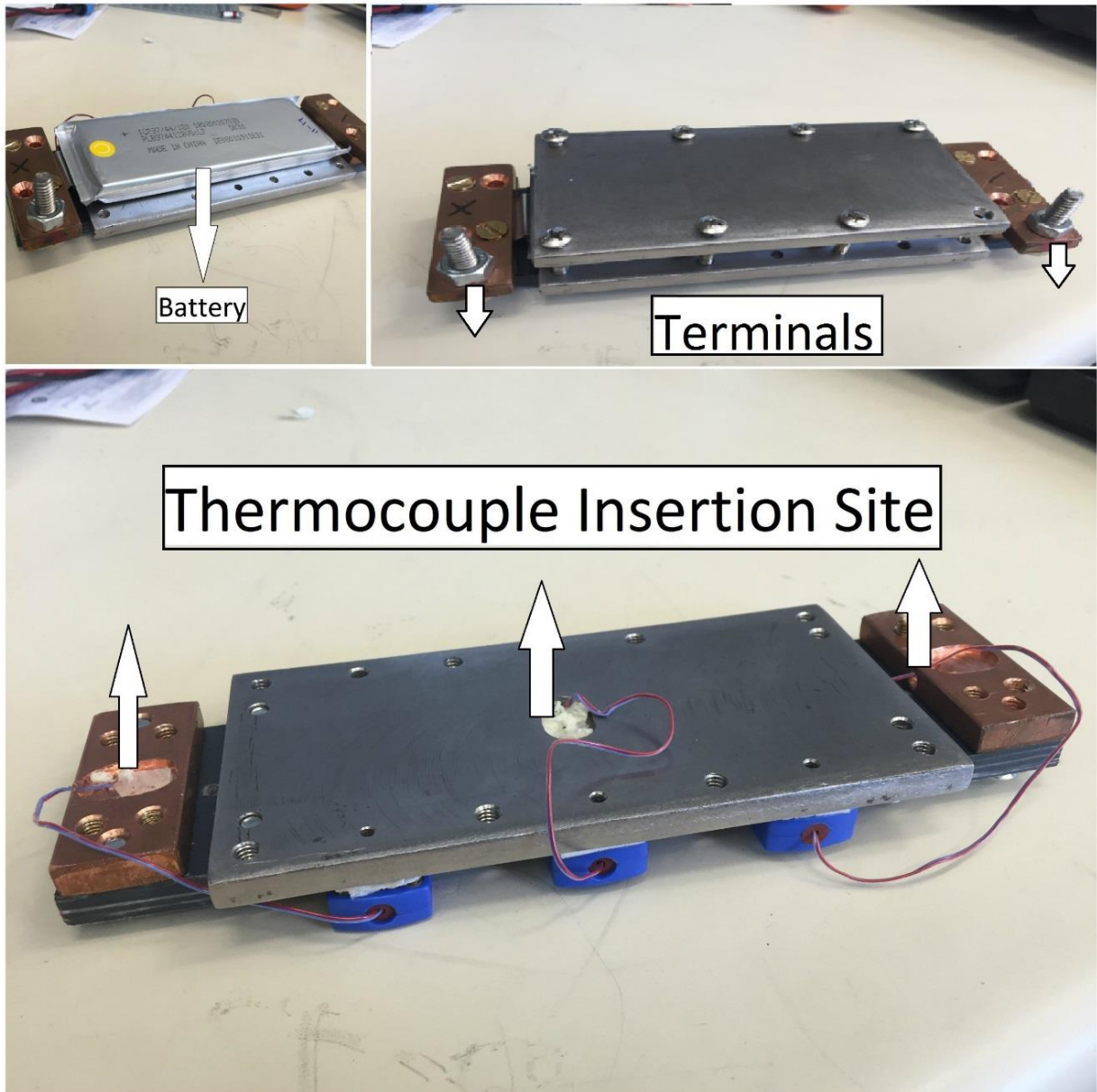


Figure 3.7: Thermocouple Insertion Sites

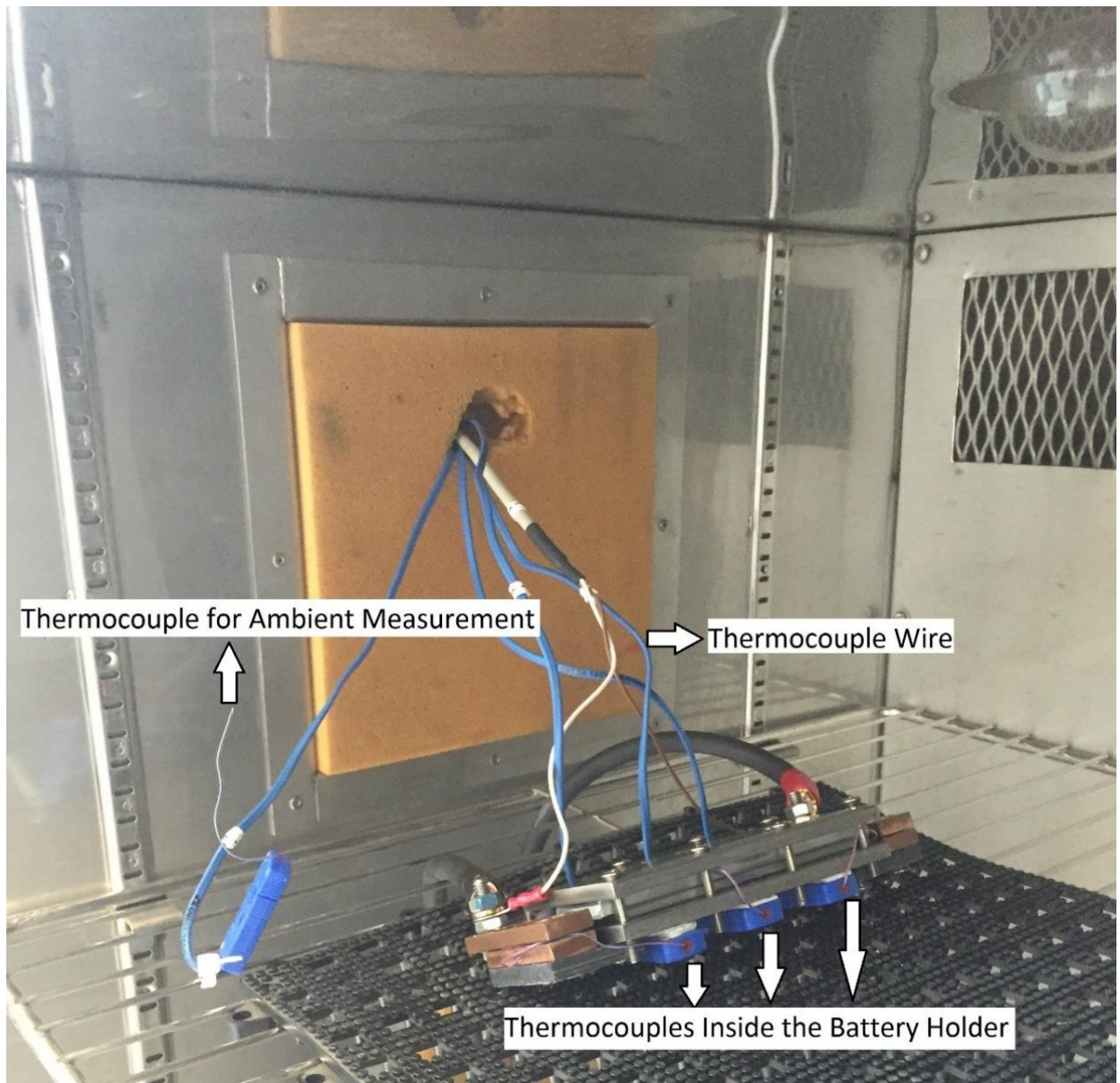


Figure 3.8: Thermocouple connections

3.2.8. Safety Circuit

The purpose of the safety is the following:

- *Cut off power from the power supply to the battery if the maximum allowable voltage or minimum allowable voltage of the battery has surpassed.*
- *Cut off power from the power supply to the battery if the maximum current limit in charge/discharge has exceeded.*
- *Cut off power from the power supply to the battery if the maximum operating temperature of the battery has exceeded.*

The safety circuit shown in Figures 3.9, uses comparator chips in order to compare reference voltages to the battery voltage and sensor generated voltage values that are indicative of current and temperature values.

The reference voltages (i.e. maximum and minimum voltage values) are set using potentiometers. Once a measurement surpasses a reference value, a relay circuit shown in Figure 3.10 that was previously powered is broken. This disconnection causes a safety relay that connects the battery to the power supply to be turned on, cutting off all power to the battery. The reference voltages can be set using voltage screens that can toggle between operating voltage, maximum and minimum set values. The flow chart of the safety circuit basics is also shown in Figure 3.11.

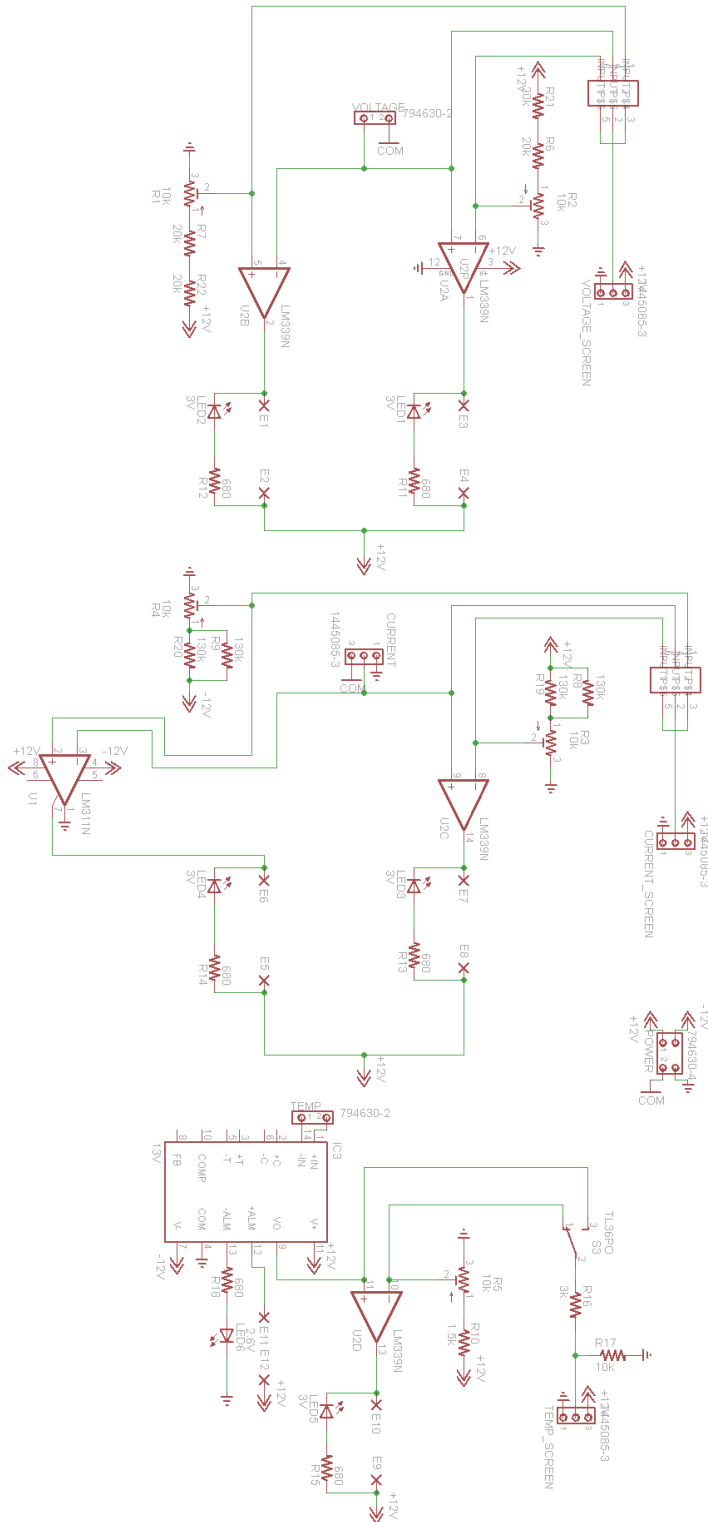


Figure 3.9: Current sensor PCB diagram Part 1.

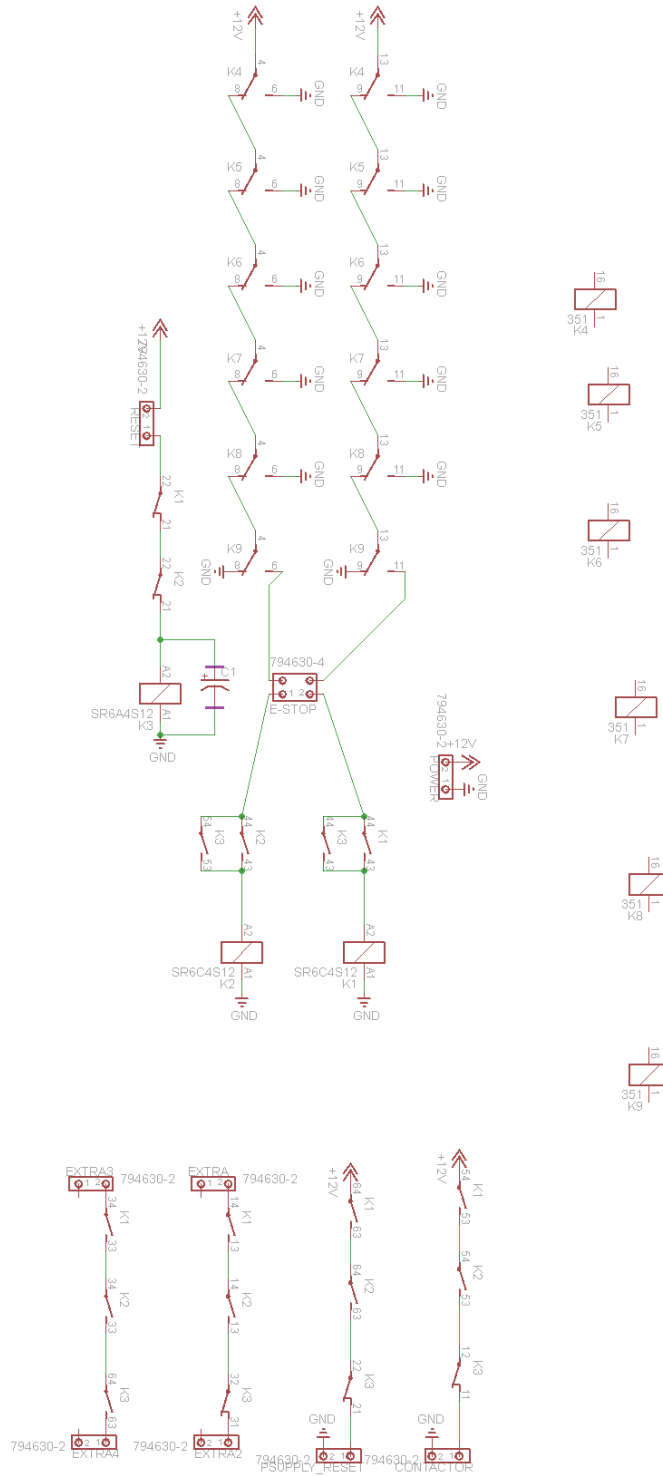


Figure 3.10: Current sensor PCB diagram Part 2.

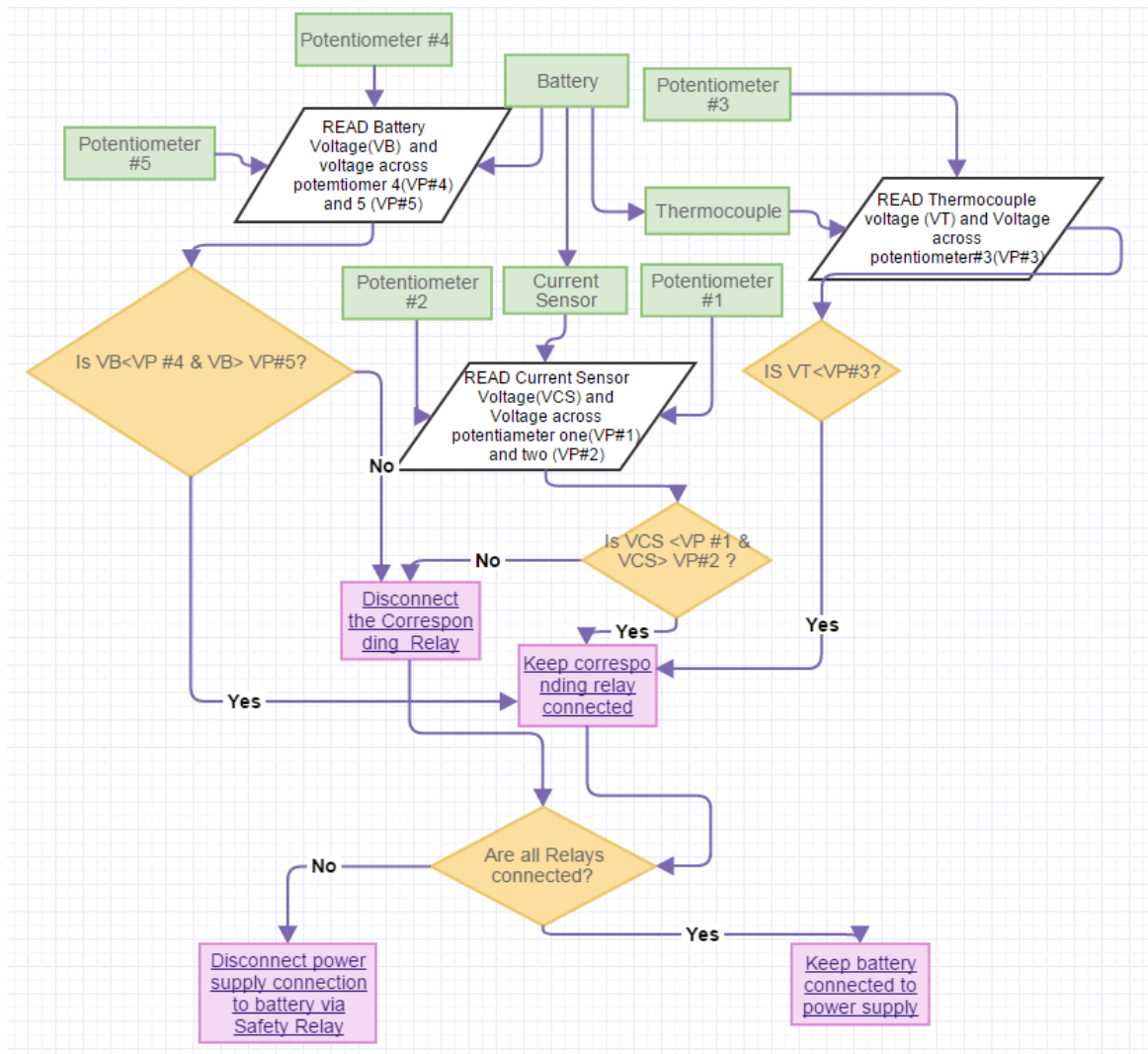


Figure 3.11: Current sensor PCB diagram Part 1.

Chapter 4

Results

Cell laboratory data is crucial in evaluating the performance of a given cell under different dynamic conditions. Furthermore, the laboratory test data can be used in parameterizing various battery models. These models can be then used for State of Charge and State of Health determination in real time applications. In order to create repeatable battery cell tests, various organizations such as the U.S department of energy have published reports [55] [56] on test protocols. The purpose of these reports is to standardize test techniques.

Based on these reports battery tests can be sub-grouped into characterization and life tests. Characterization tests entail evaluating the standard performance of the battery [55]. Life testing involves determining the behavior of the battery as it degrades.

4.1.Characterization tests

Here characterization tests are performed for the purpose of demonstrating cell tester capabilities and modeling the battery. The tests performed include static capacity test, SOC-OCV characterization test, drive cycle tests and electro-chemical impedance spectroscopy tests. The characterization tests are all performed at room temperature.

4.1.1. Static Capacity Test

A static capacity test is conducted in order to compute the capacity of the cell in ampere-hours. This test is performed following an hour of rest from a fully charged state at a constant discharge current until the terminal voltage reaches the cut-off voltage. At this point according to the constant current constant voltage (CCCV) protocol, voltage is held constant and current is dropped to 0.02C. Integrating under the current-SOC curve yields the capacity for the battery under study as shown in Equation 2.1. This test was programmed using LabView, the block diagram and front panel are shown below:

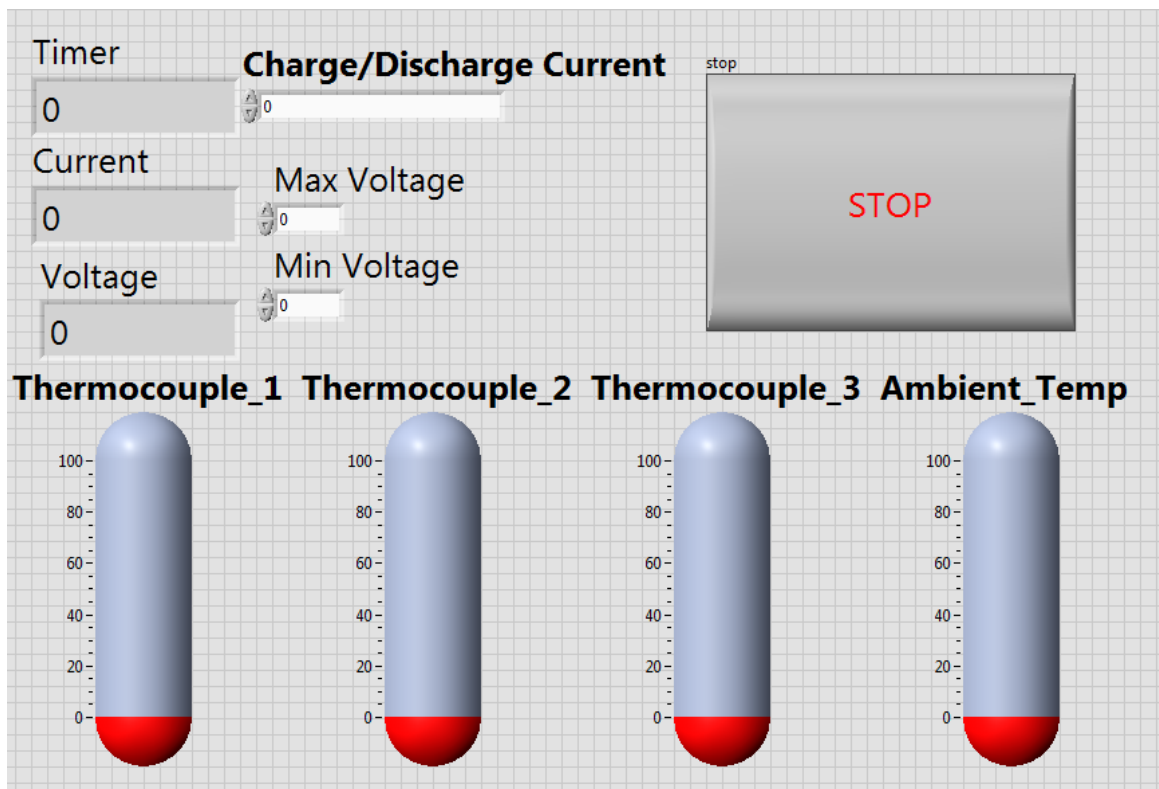


Figure 4.1:Front Panel Design for Capacity and SOC/OCV Tests

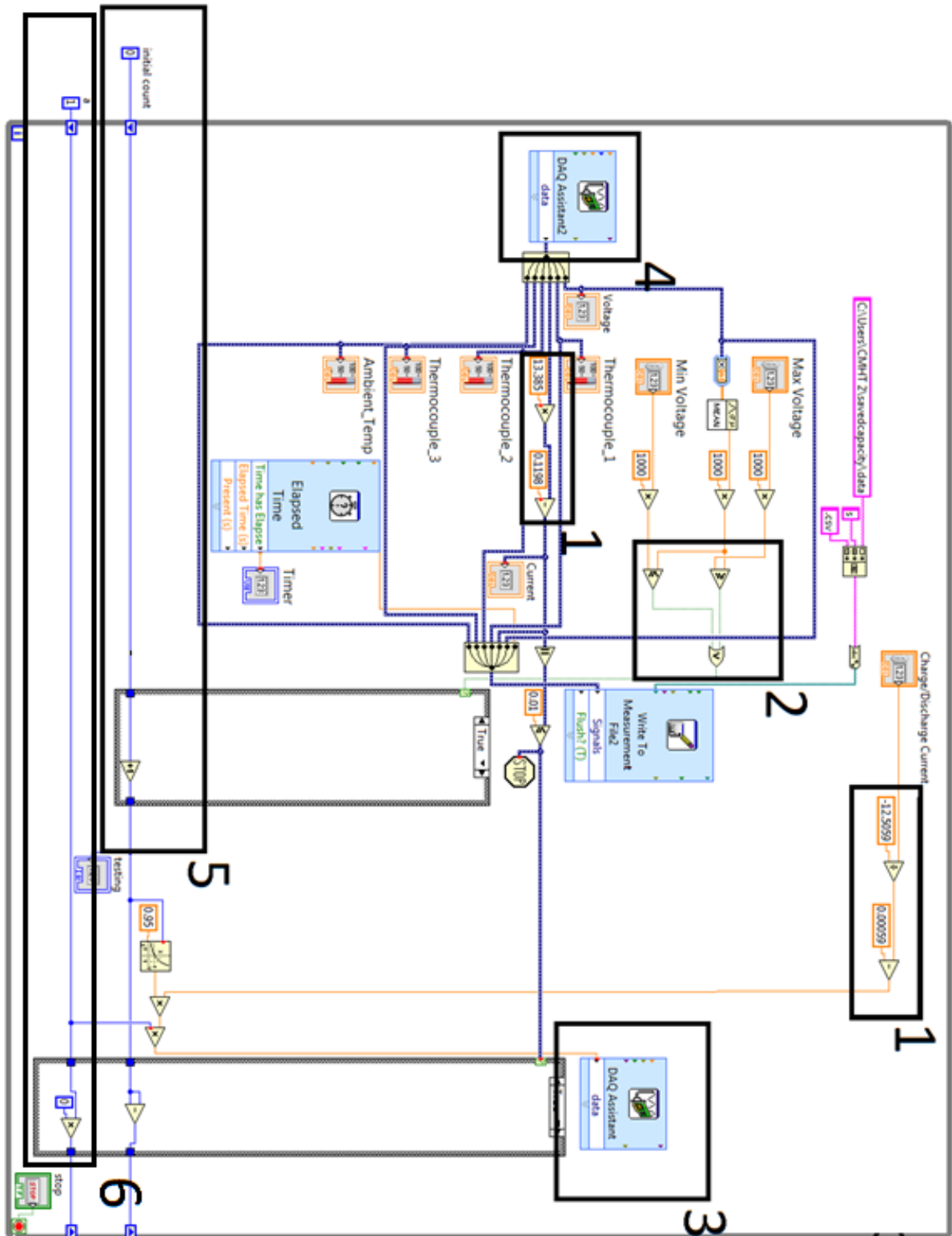


Figure 4.2:Block Diagram for Static Capacity and SOC-OCV Tests

The blocks on Figure 4.1 are explained below:

The timer block labeled “*Timer*”, keeps track of the number of seconds since the test has begun. The current and voltage blocks labeled “*Current*” and “*Voltage*” allow for monitoring of current and voltage respectively. Battery temperature is monitored using readings from “*Thermocouple-1*” to “*Thermocouple-3*” that correspond to measurements taken from thermocouples TR1 to TR3 (refer to Figure 3.2) respectively. The ambient temperature (TR4) is monitored using thermometer labeled “amb_Temp”. The block labeled as “*charge/discharge current*” allows for modification of the current rate. Note that the current rate for a static capacity test is 1C. The blocks labeled as “*Max Voltage*” and “*Min Voltage*” are used to input maximum and minimum voltages specified by a manufacturer of a given battery cell, and should be modified as such. The “*Stop*” button is provided so that the test can be stopped at any given time.

Key parts of Figure 4.2 are labeled and separately described in Table 4.1.

Table 4.1: Block Diagram notes for Static Capacity and SOC-OCV tests

Number	Note
1	<p>Parts labeled as “1” are calibration blocks. Calibration needs to be performed in order to make readings displayed in the GUI (Figure 4.1) meaningful.</p> <p>The input current (<i>charge/discharge current</i> on Figure 4.1) is calibrated by dividing it by $\frac{125}{10} = 12.5$, because Pin 11 of the Analog I/O port of the power supply [57] is used as an external reference for controlling current. 0 to $\pm 10V$ corresponds to zero to $\pm 125 A$ when power supply is set in current mode.</p> <p>The PCB Board (shown in Figure 3.5) uses a 75 ohm resistor to convert the scaled down current to a voltage in order for it to be processed by the Analog input module. In order to convert the scaled down voltage back to a current reading and show it visually in the “<i>Current</i>” block of Figure 4.1, The signal is multiplied by $\frac{1}{75} * 1000 = 13.33$.</p>
2	<p>The part labeled as “2” is used for control of current and voltage. If the Voltage of the cell is larger than the value inputted in the “<i>MaxVoltage</i>” block or smaller than the value inputted in the “<i>MinVoltage</i>” block (refer to Figure 4.1) then voltage is held constant and current is decreased exponentially until it reaches $\pm 0.01 A$ at which point the program stops, this is called the constant Voltage protocol. The Maximum allowable and minimum allowable voltages for the cell used in this research are presented in table 3.1.</p>
3	<p>The part labeled as “3” is the block diagram depiction of Analog output modules presented in section 3.2.4.</p>
4	<p>The part labeled as “4” is the block diagram depiction of Analog input modules presented in section 3.2.4. The values of temperature, current and voltage are recorded during a specific test using the “<i>write to measurement file</i>” block in Figure 4.2 and stored in an excel file. Current, Voltage and Temperature graphs for the static capacity test are shown in Figures 4.3 to 4.5.</p>
5	<p>The part labeled as “5” is used for control of current and voltage. Initially $0.95^0=1$ is used for constant current protocol, once conditions described for part “2” are reached, increments of 1 are added to the power ex.(0.95^1)for constant voltage protocol</p>
6	<p>The part labeled as “6” is the condition for end of program (current equal to 0).</p>

The current, voltage and temperature plots for the static capacity test are provided below:

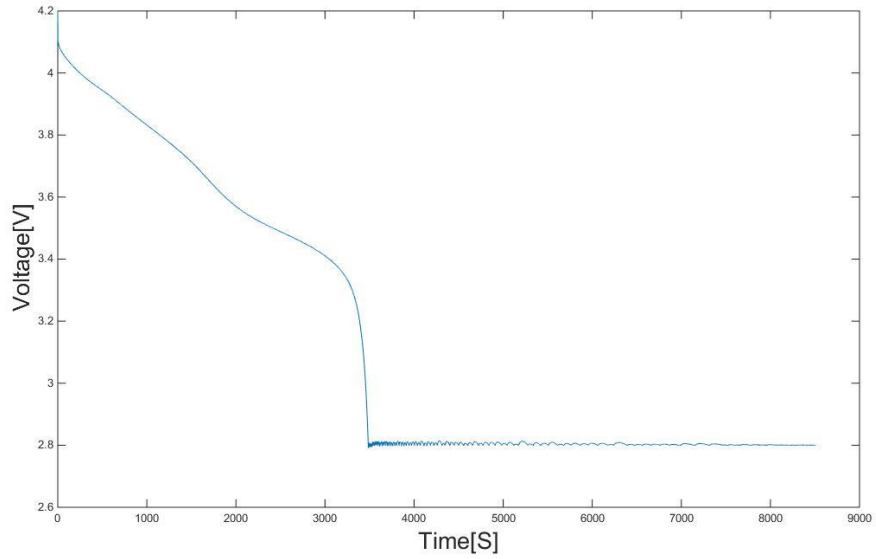


Figure 4.3: Voltage vs Time for a Static Capacity test

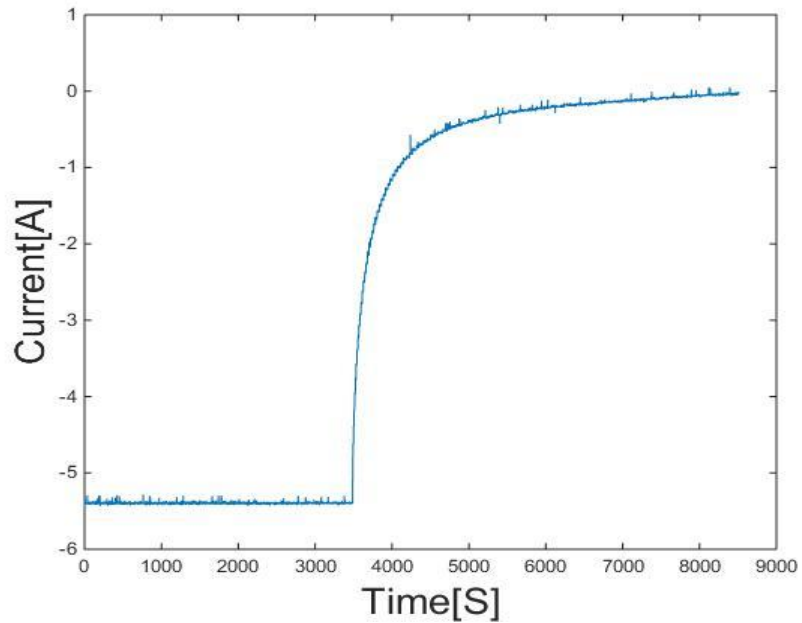


Figure 4.4: Current Vs Time for a Static Capacity Test

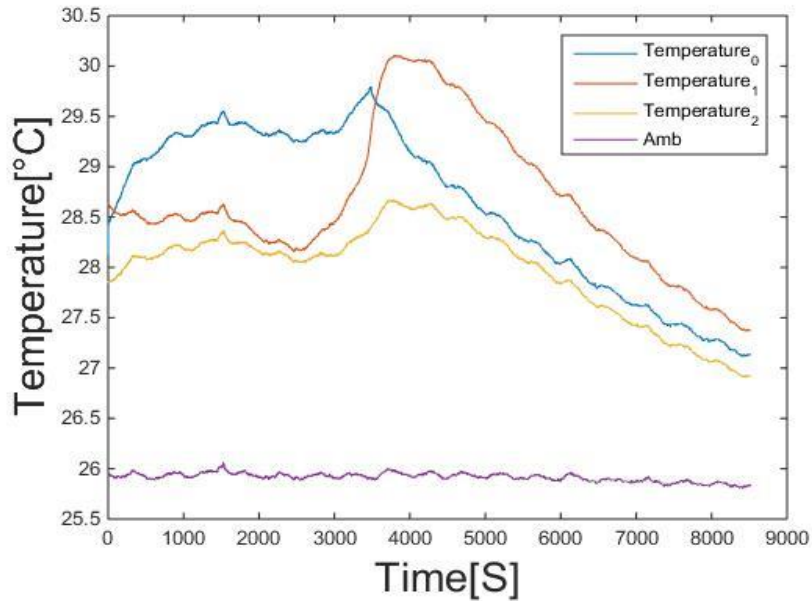


Figure 4.5: Temperature Vs Time for a Static Capacity Test

Integrating under the current curve (shown in Figure 4.4) using trapezoidal approximation yields the capacity of 5.9 Ah. This value is higher than the 5.4 Ah specified for this cell by the manufacturer. This is due to manufacturers commonly setting conservative specifications.

4.1.2. SOC-OCV Test

This test is conducted in order to obtain open circuit voltage as a function of State of Charge. This relationship can then be used in various modeling strategies such as equivalent circuit modeling.

The test is conducted at very low current rates such as C/20, C/15 and C/10, in order to reduce cell dynamics and minimize internal resistance. The ohmic resistance being diminished, the measured voltage of the cell is the open circuit voltage. The test involves

charging the battery with C/10, letting the battery rest for an hour and discharging with C/10. In order to compute OCV as a function of State of Charge, the coulomb counting method is utilized (Equation 2.1). Using trapezoidal approximation the current curve is integrated and time axis is converted into SOC axis as shown in Figure 4.6. The hysteresis level shown in Figure 4.7 is considerably high and needs to be accounted for in the utilized modeling technique (see section 2.6.4).

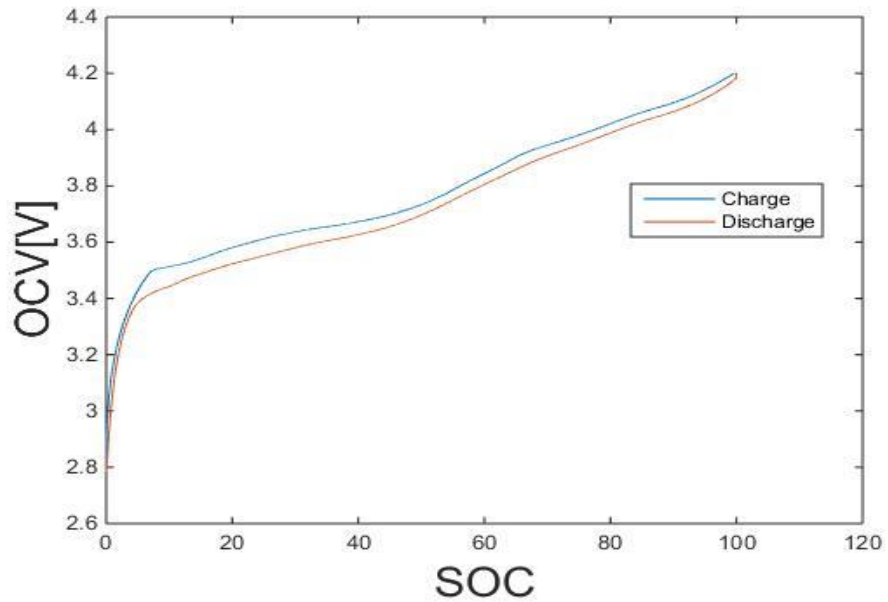


Figure 4.6:OCV vs SOC for charge and discharge

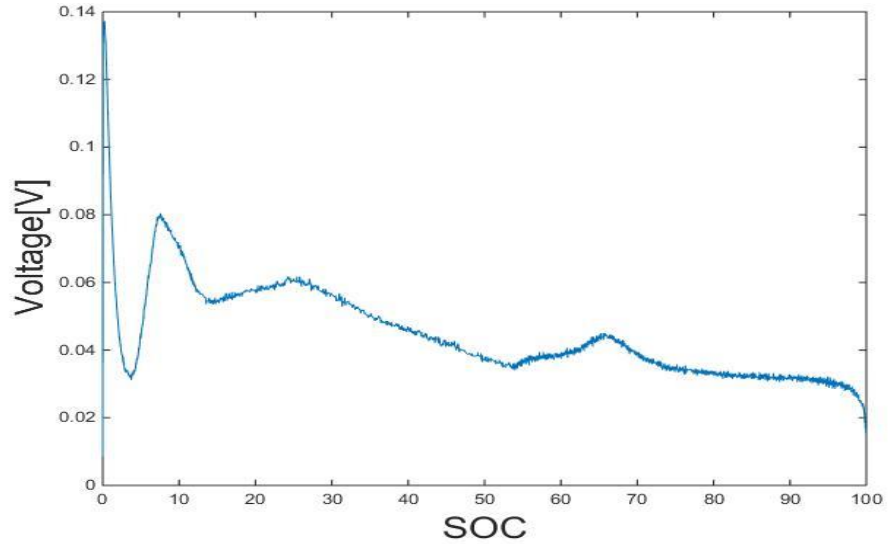


Figure 4.7:Hysteresis vs SOC

The two curves are then averaged in order to obtain the relationship between open circuit voltage and State of Charge. The average SOC-OCV curve as well as a 10th order polynomial fit to the curve are shown in Figure 4.8. The *polyfit* function in MATLAB is used in order to fit a 10th order polynomial function to the averaged experimental curve. Further the *polyval* MATLAB function is used in order to compute the polynomial at distinct points. The coefficients for the 10th order polynomial are shown in Table 4.2.

Table 4.2: Coefficients for the 10th order polynomial fit to the SOC-OCV curve

Coefficient	Value
1	-3.4566e-17
2	1.9555e-14
3	-4.7816e-12
4	6.6072e-10
5	-5.6604e-8
6	3.31034e-6
7	-1.0860e-4
8	0.0024
9	-0.0297
10	0.2013
11	2.9133

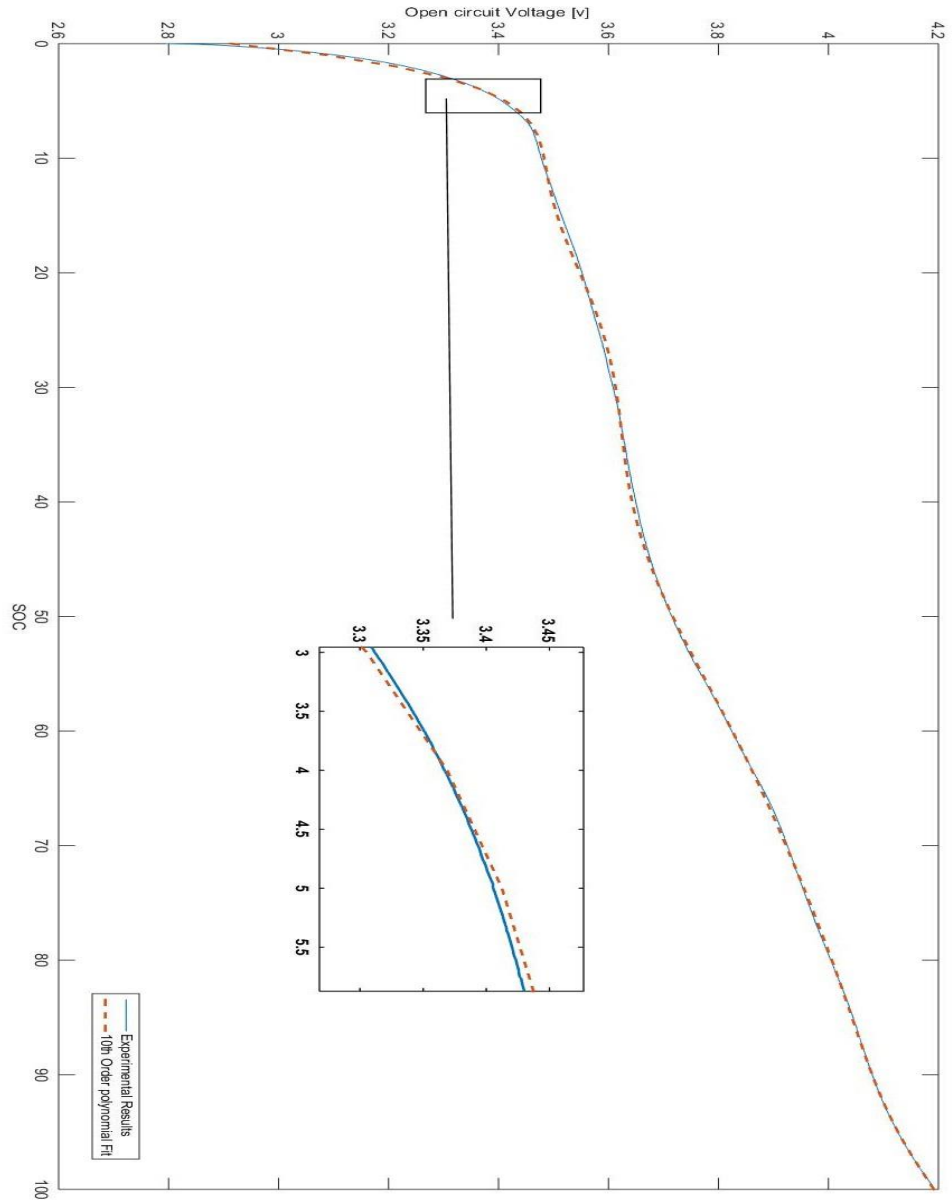


Figure 4.8:OCV vs SOC- Averaged Experimental Results and 10th Order Polynomial fit

4.1.3. Driving Cycles

Driving cycles are a number of tests designed by the US Environmental Protection Agency (EPA) to measure fuel economy of passenger cars [57]. Using an electric vehicle model, the velocity profiles from these tests can be used to develop pack current profiles. The pack current profile can then be scaled down to individual cell level. Cycles are rich in frequency content, consequently they can be used for parameter identification for various models. The cycles covered here include Urban Dynamometer Driving Schedule (UDDS), US06 Supplemental Federal Test Procedure (SFTP) and Highway Fuel Economy Driving Schedule (HWFET). The UDDS cycle simulates city driving conditions. This cycle represents a route of 12 *km* with repeated stops. The maximum and average speed for this test are 91 *km/h* and 31 *km/h* respectively [58]. The US06 cycle simulates a highly aggressive and dynamic driving schedule. This cycle represents a route of 13 *km* with rapid speed changes. The maximum and average speed for this test are 130 *km/h* and 75 *km/h* respectively [58]. The HWFET cycle simulates highway driving conditions. This cycle represent a route of 16.5 *km* with no stops. The maximum and average speed for this test are 97 *km/h* and 77 *km/h* respectively. The velocity profiles of the discussed cycles are presented in Figures 4.9 to 4.11. [58]:

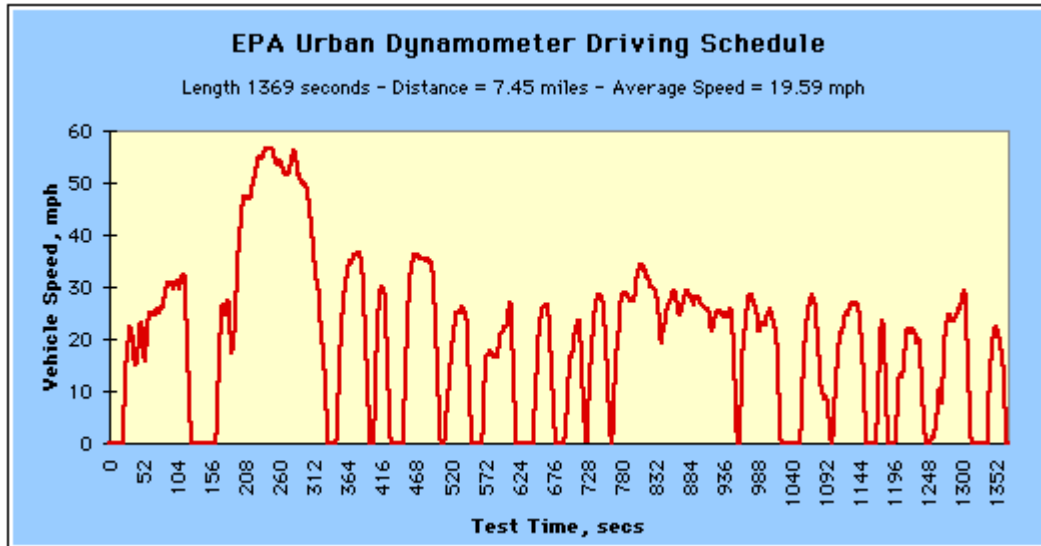


Figure 4.9:UDDS Driving Schedule Velocity Profile [58]

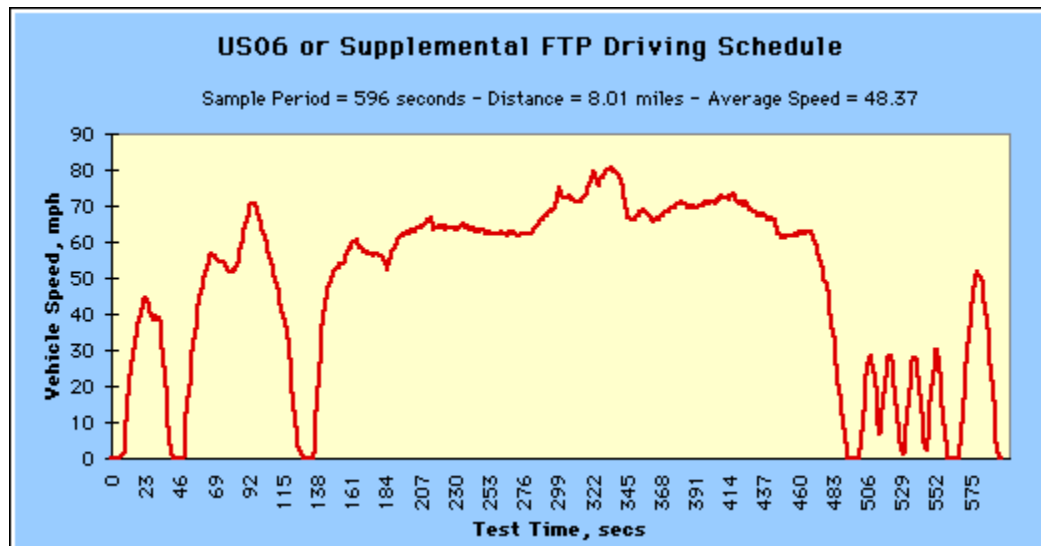


Figure 4.10:US06 Driving Schedule Velocity Profile [58]

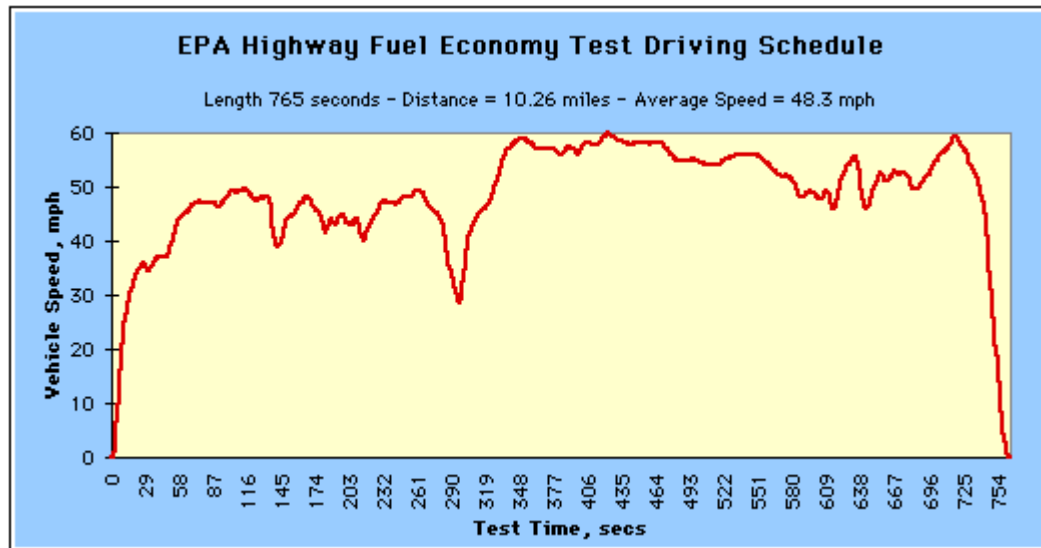


Figure 4.11: HWFET Driving Schedule Velocity Profile [58]

The battery was subjected to two cycles, separated by a 1C discharge period in between as shown in Figures 4.12 to 4.17. This test methodology was selected in order to cover a large SOC range for the parameterization and validation of equivalent circuit models.

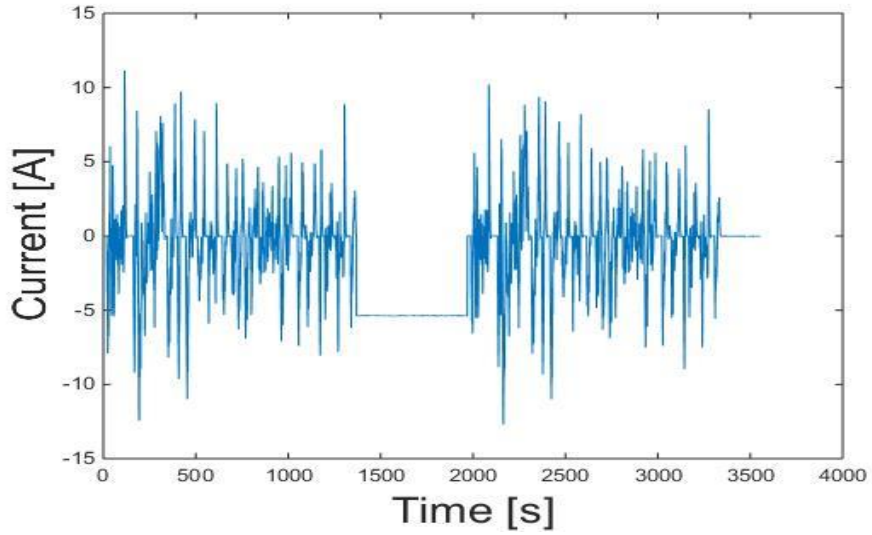


Figure 4.12:UDDS Driving Schedule Cell Current Profile

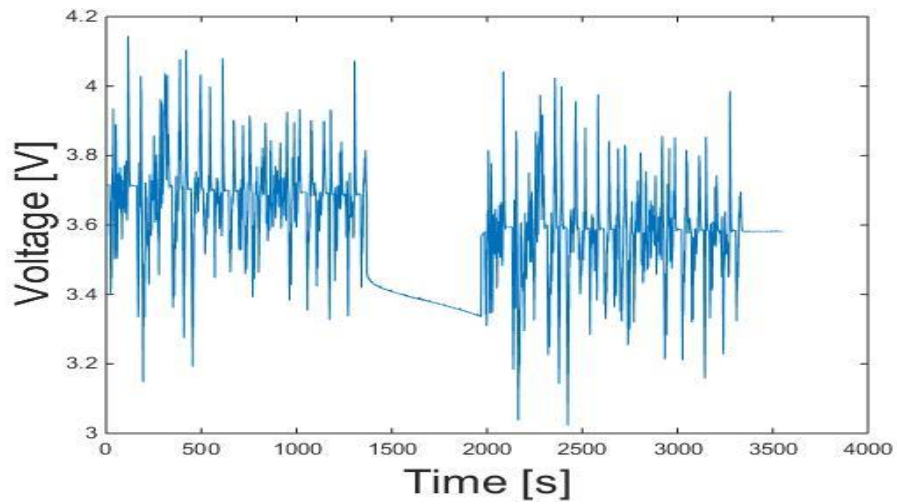


Figure 4.13:UDDS Driving Schedule Cell Voltage Profile

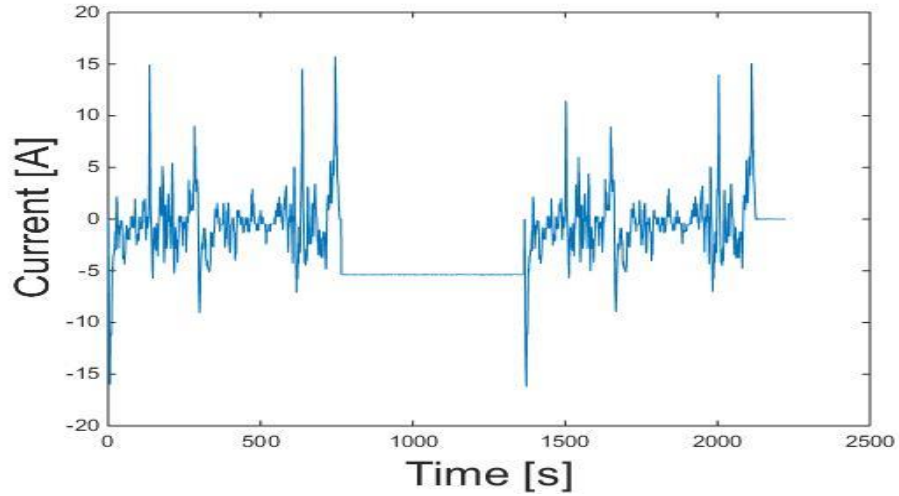


Figure 4.14: HWFET Driving Schedule Cell Current Profile

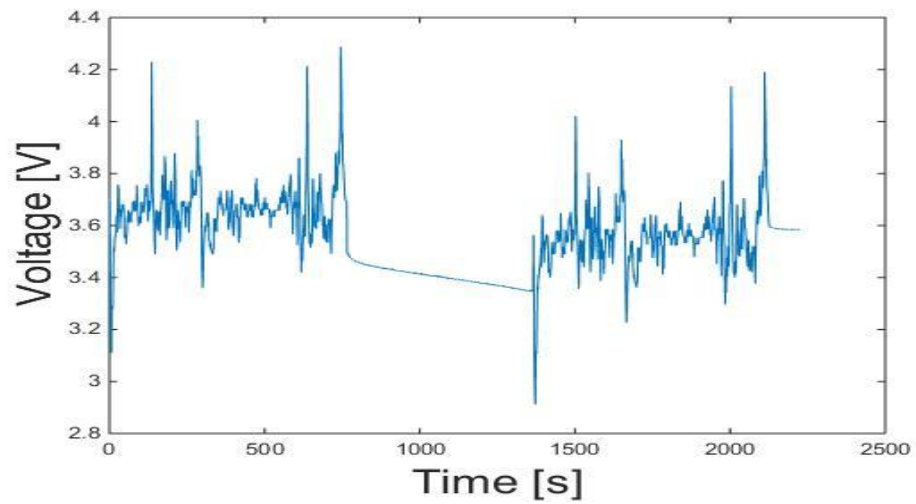


Figure 4.15: HWFET Driving Schedule Cell Voltage Profile

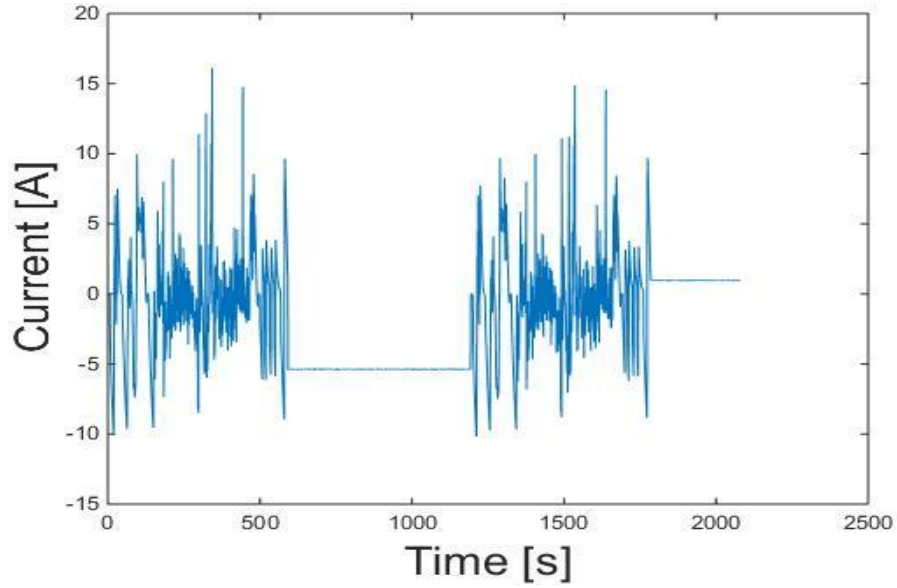


Figure 4.16:US06 Driving Schedule Cell Voltage Profile

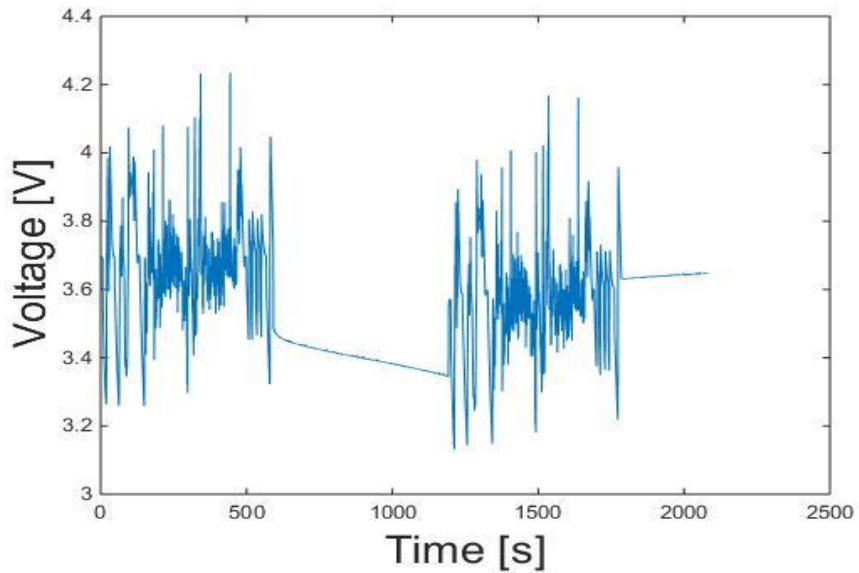


Figure 4.17:US06 Driving Schedule Cell Voltage Profile

The cycles were programmed using LabVIEW software, the panel of which is demonstrated in Figure 4.18. Here the user can select the appropriate cycle in “*Select Wave Form*” pull down menu. The “*Timer*”, “*Voltage*” and “*Current*”, “*Thermocouple*” blocks update the user on parameter values as the test is running. The “*Wave Form*” graph demonstrates the shape of the selected input profile. The values of parameters is stored in an excel spreadsheet following the termination of the test. Location of the stored file is the default path set in the program, however it is possible for the user to change the file path on the front panel.

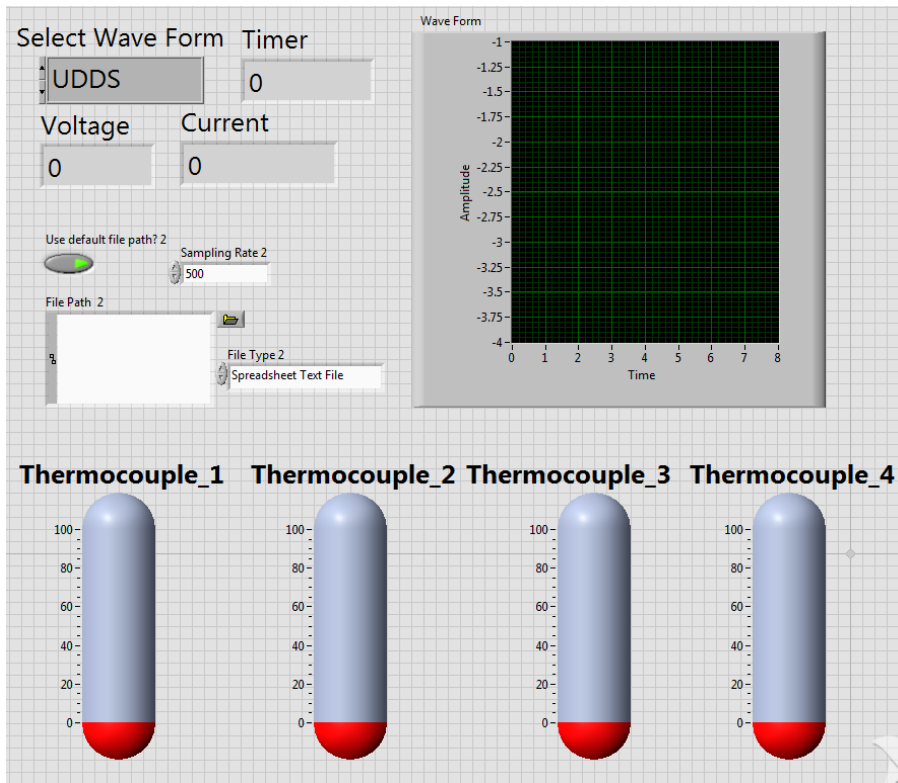


Figure 4.18:Front Panel for drive cycle tests

4.1.4. Battery Cycling Test

Cycling tests are conducted in order to simulate the degradation of State of Health as a results of battery usage over time. The block diagram for battery cycling is shown in Figure 4.19. The user can select charging/discharging current by modifying the *Cycling Current* box on the front panel. The voltage range between which the cell is cycled at can be modified using *Cycling Min Voltage* and *Cycling Max Voltage* boxes. The number of full cycles that have been applied to the battery is shown by *Number of Cycles* box.

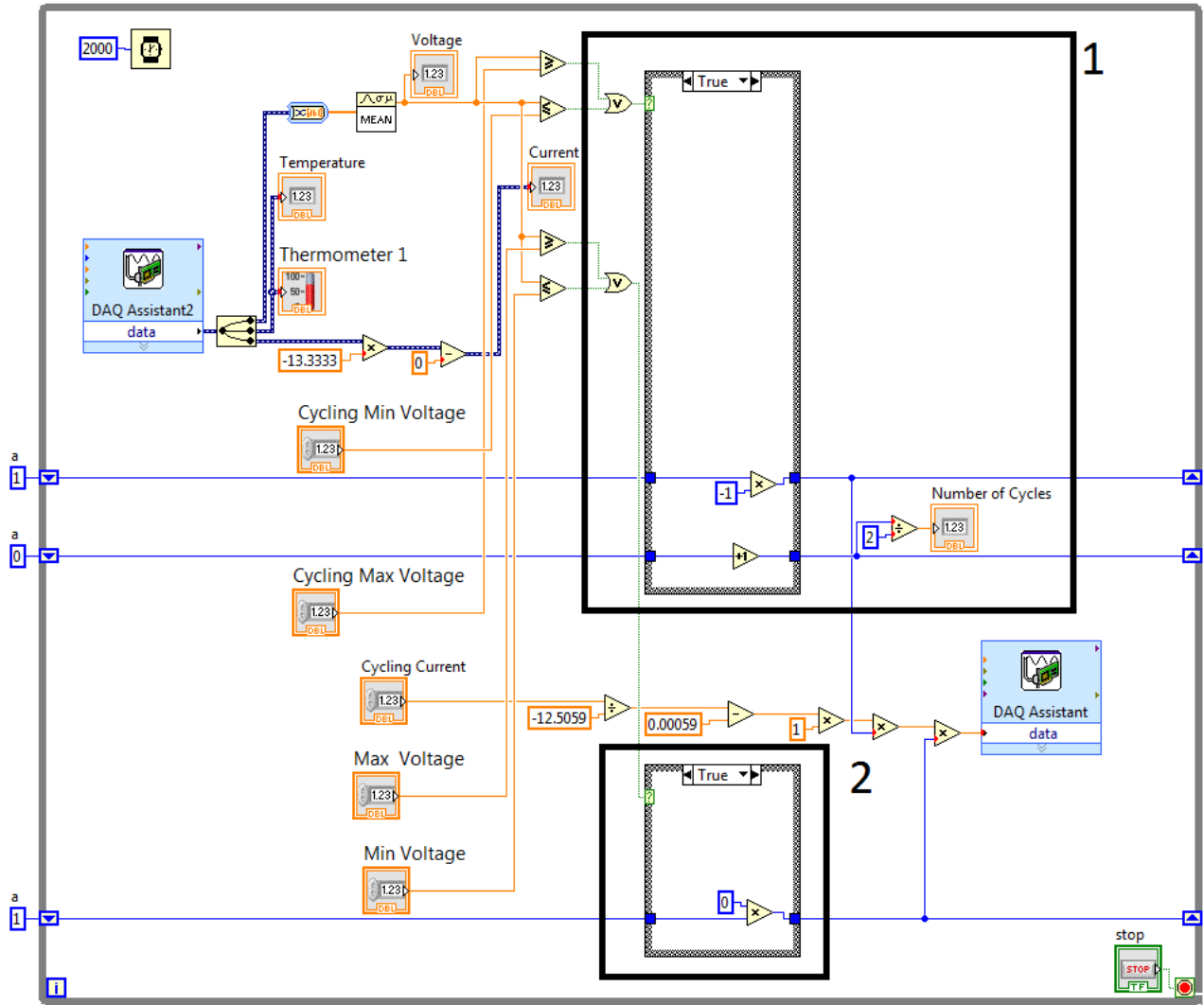


Figure 4.19:Block Diagram for cycling tests

Key parts of Figure 4.19 are labeled and separately described in Table 4.3.

Table 4.3: Block Diagram notes for Aging tests

Number	Note
1	The part labeled as “1” is used for cycling of the battery cell. If the Voltage of the cell is larger than the value inputted in the “ <i>Cycling Max Voltage</i> ” block or smaller than the value inputted in the “ <i>Cycling Min Voltage</i> ” block (refer to Figure 4.19) then current input “ <i>Cycling Current</i> ” is multiplied by -1 and reversed in direction. This effectively means the cell is cycled between values inputted in “ <i>Cycling Max Voltage</i> ” and “ <i>Cycling Min Voltage</i> ” blocks.
2	The part labeled as “2” is used for shutting the current value to 0 when voltage limits are exceeded. If the Voltage of the cell is larger than the value inputted in the “ <i>MaxVoltage</i> ” block or smaller than the value inputted in the “ <i>MinVoltage</i> ” block (refer to Figure 4.19) then then current input “ <i>Cycling Current</i> ” is multiplied by 0. This effectively stops the cell from getting cycled.

4.2. Electro-chemical Impedance Spectroscopy

In order to obtain high frequency characterization of the system, initial tests on a simple resistor had to be performed. Firstly to discover if the wiring and power supply skewed measurement by inducing a gain and or phase shift. Secondly to compare high frequency characterization results of the tester to results obtained from industrially used equipment. As such four 0.1Ω resistors were tested in individual and series configuration (series configuration shown in Figure 4.20). The EIS tests were conducted using both the designed tester and a Gamry Interface 1000. Gamry Interface 1000 is a potentiostat/galvanostat used for numerous high frequency applications such as battery testing and sensor development.

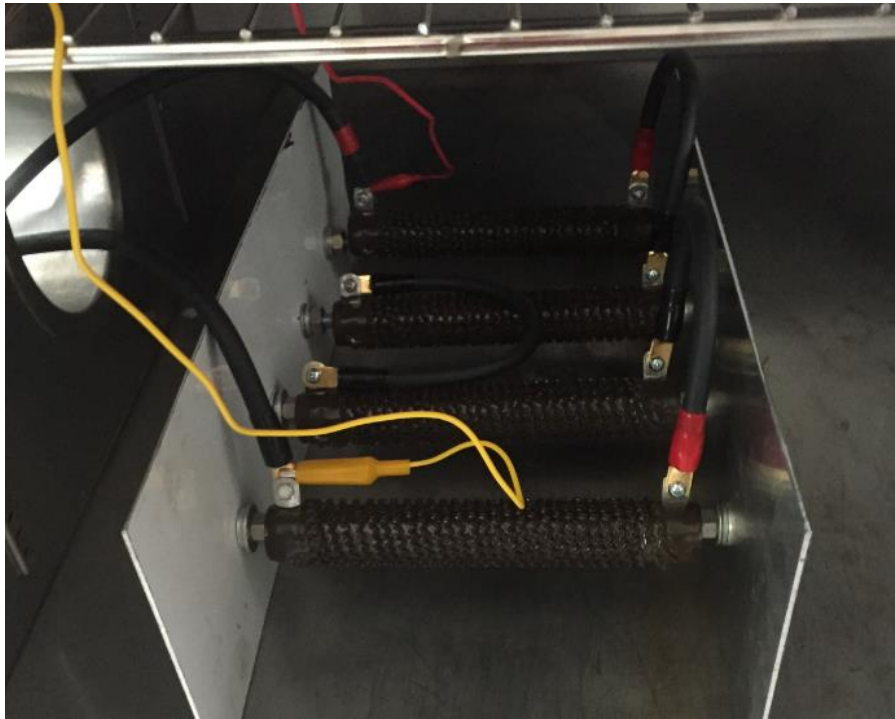


Figure 4.20: Resistor Setup for validation Test

The electro-chemical impedance spectroscopy tests involved applying a sine wave with the amplitude of $1 A$ using the Analog Output Module and collecting current and voltage readings from the system using the Analog Input Module). The sampling frequency of $50 KHZ$ was used for all the tests. Figure 4.21 shows the gain plot for the Power supply. In order to eliminate the effect of power supply on the high frequency characterization of the system, waveforms at different frequencies were multiplied by $1/Gain_{power supply}$.

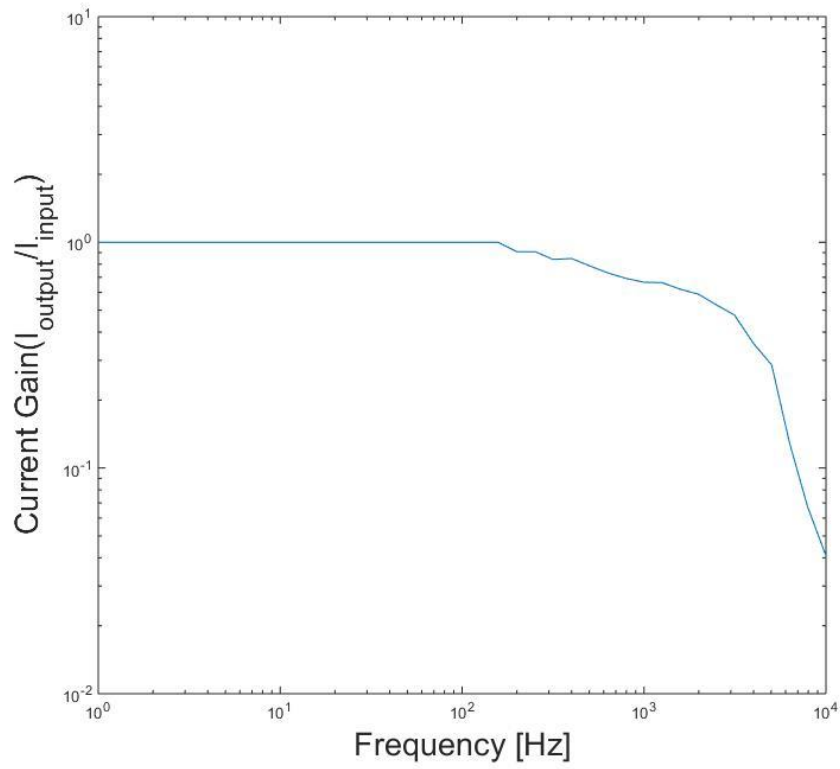


Figure 4.21: Bode Plot for the Power Supply [58]

The Block Diagram and front panel for high frequency tests are shown in figures 4.22 and 4.23 respectively.

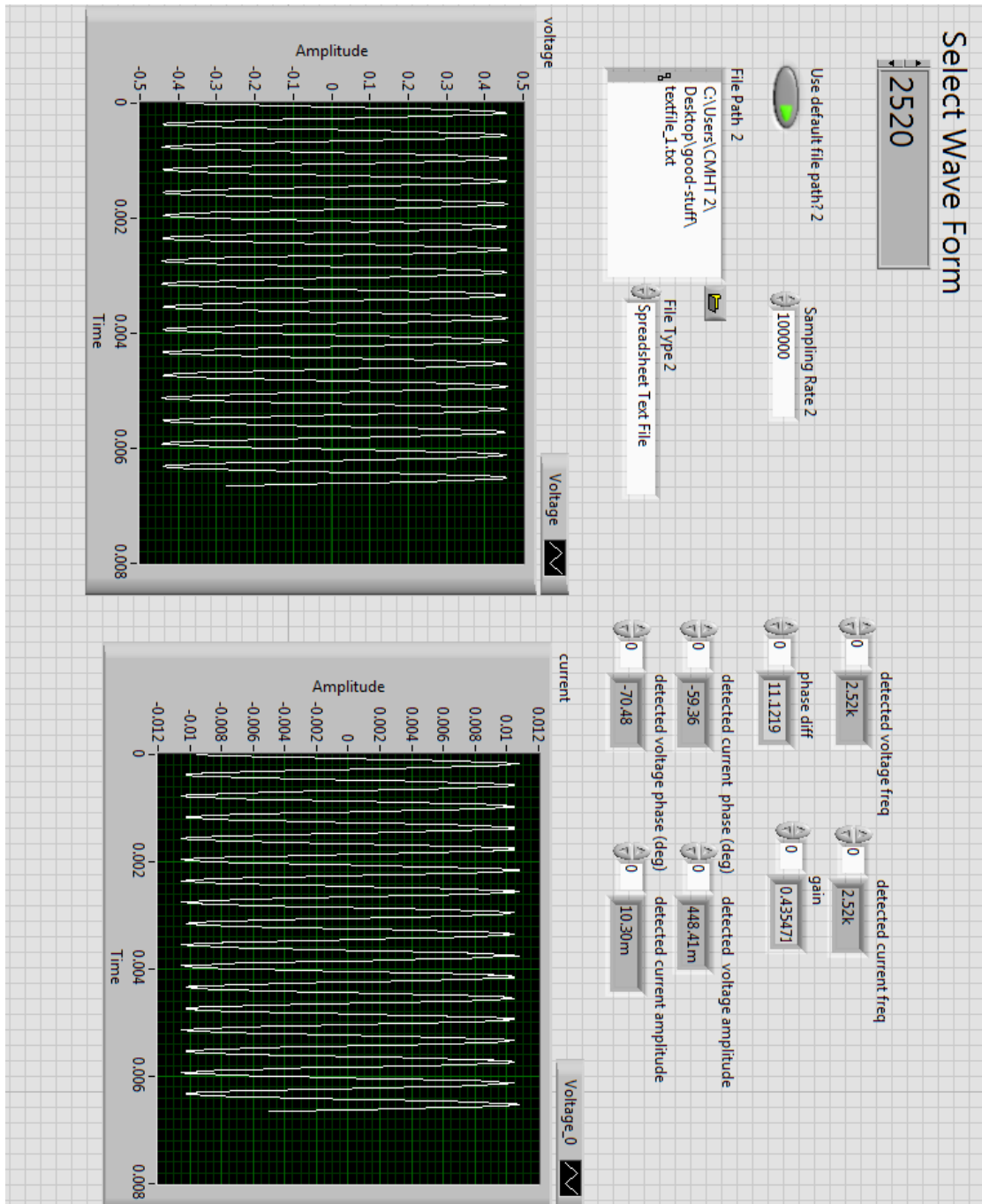


Figure 4.22:Front Panel for EIS tests [58]

Key parts of Figure 4.23 are labeled and separately described in Table 4.4.

Table 4.4: Block Diagram notes for EIS tests

Number	Note
1	The part labeled as “1” is the block diagram depiction of Analog input modules presented in section 3.2.4.
2	The part labeled as “2” which is the “ <i>signal tone information</i> ” block in LabVIEW takes a signal in and returns signals Amplitude (“ <i>detected voltage amplitude</i> ” and “ <i>detected current amplitude</i> ” on Figure 4.21), frequency (“ <i>detected voltage freq</i> ” and “ <i>detected current freq</i> ” on Figure 4.21) and phase (“ <i>detected voltage phase</i> ” and “ <i>detected current phase</i> ” on Figure 4.21).
3	The part labeled as “3” returns the Impedance gain at a specific frequency (the “ <i>detected voltage amplitude</i> ” is divided by the “ <i>detected current amplitude</i> ”).
4	The part labeled as “4” returns the phase gain at a specific frequency (the “ <i>detected voltage phase</i> ” is subtracted by the “ <i>detected current phase</i> ”).
5	The part labeled as “5” is the block diagram depiction of Analog output modules presented previously in section 3.2.4.
6	The part labeled as “6” is the depiction of Programmed Sinusoidal current input waves at different frequencies

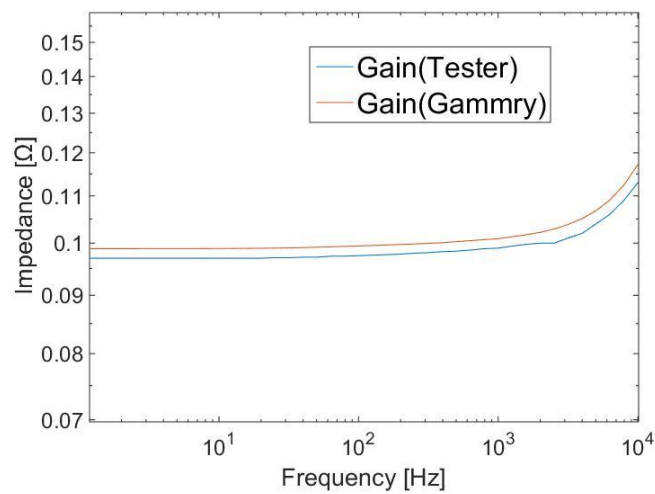


Figure 4.24: Impedance vs. Frequency for Tester and Gammry tests

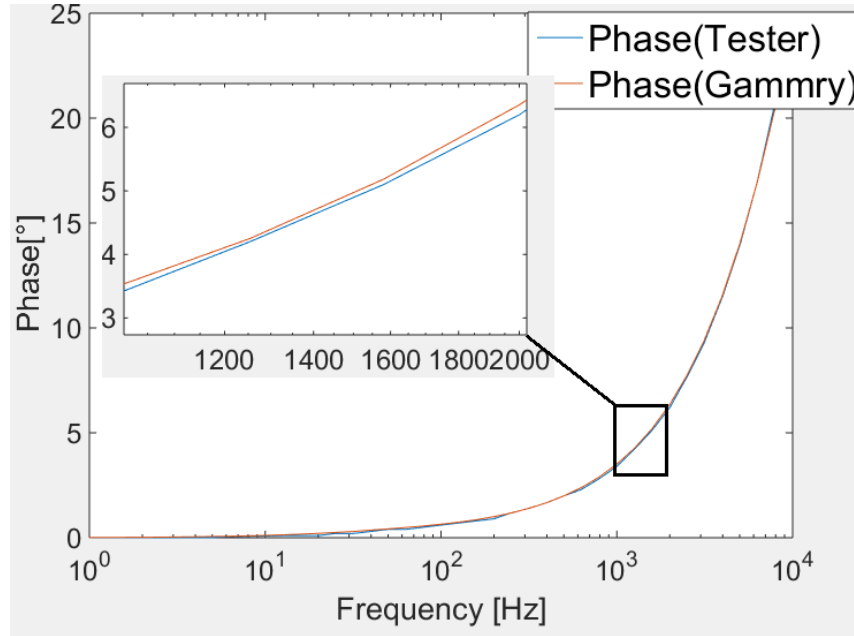


Figure 25: .Phase vs Frequency for Tester and Gammy tests

4.2.1. SOC Measurements

EIS tests were implemented using the developed tester at different levels of SOC(20%, 50%, 80%) and at room temperature. The results are shown in Figures 4.26 to 4.28. It is apparent that the ohmic internal resistance of the cell, visually shown as the intersection of the real and imaginary axes on Figure 4.28, remains constant for all SOC levels. Conversely the semi-circle portion of the spectrum, which demonstrates the charge transfer phenomenon changes as a direct result of variation in SOC. The results shown are consistent with works demonstrated in Chapter 2.

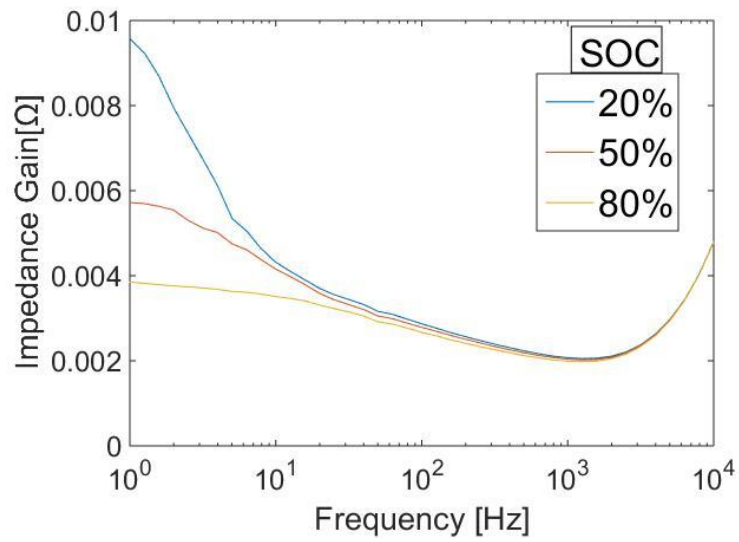


Figure 4.26: Impedance vs. Frequency at different SOC [58]

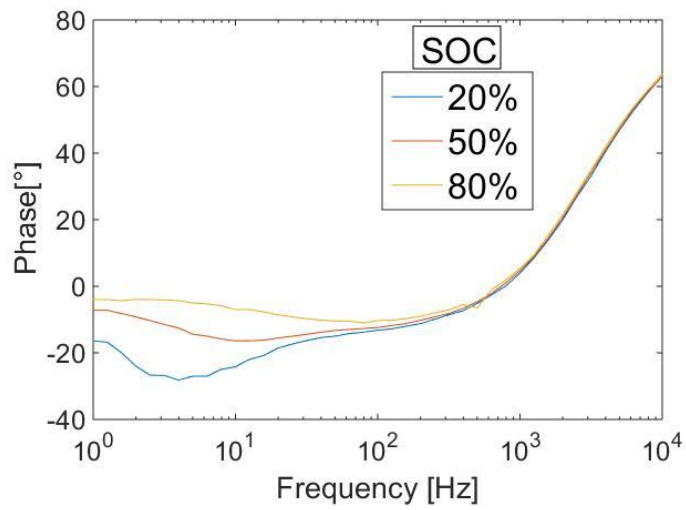


Figure 4.27: Phase vs. Frequency at different SOC [58]

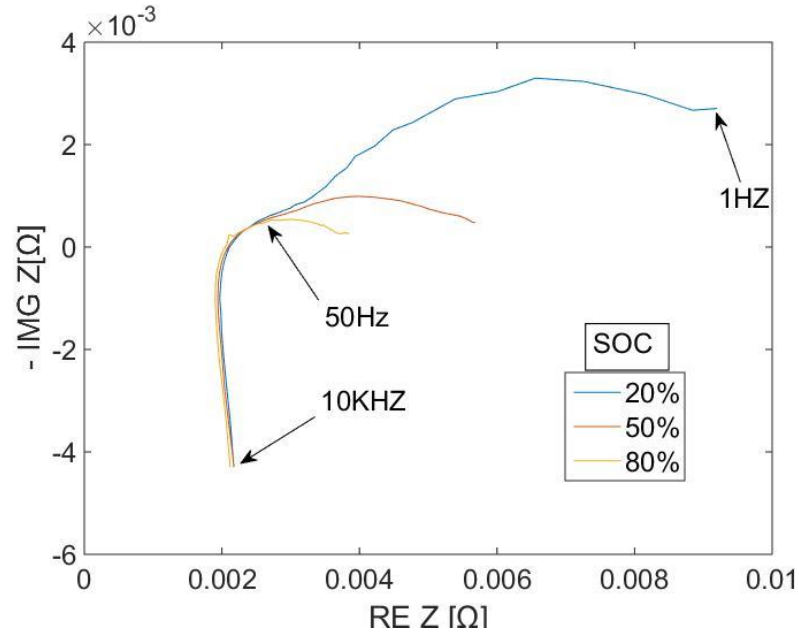


Figure 4.28:EIS spectra at different SOC

4.2.2. Ambient Temperature Measurements

EIS tests were implemented using the developed tester at different temperatures (0°C, 20°C and 40°C) all at 50% State of Charge. The results shown in Figures 4.29 to 4.31 demonstrate that variation in ambient temperature impacts both ohmic resistance and charge transfer loop parts of the spectra. Most notably the width of the mid-frequency arc is significantly increased at lower temperatures. It can be concluded that at higher temperatures, impedance is reduced and therefore is possible to transport more power. The results presented are consistent with findings of Abraham et al. [59]

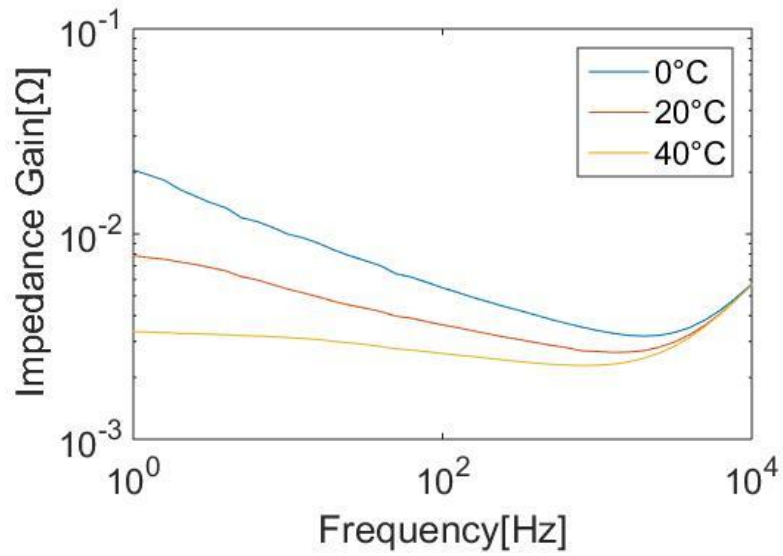


Figure 4.29: Impedance vs. Frequency at different temperatures

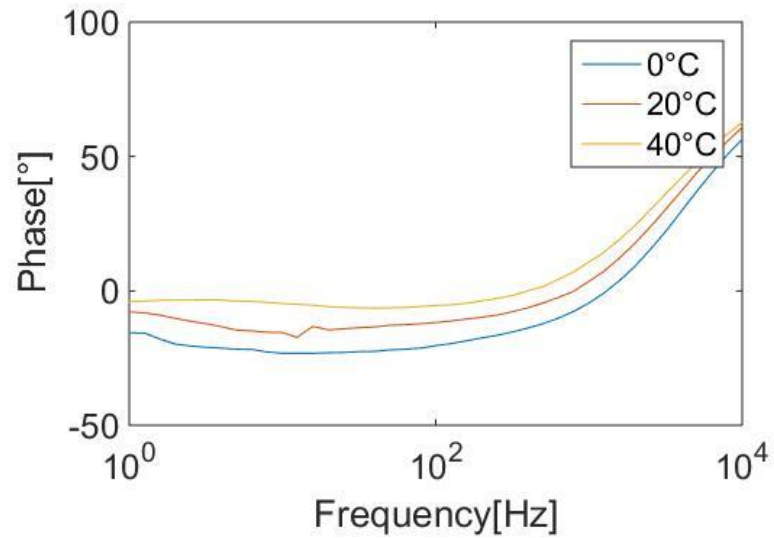


Figure 4.30: Phase vs. Frequency at different Temperatures.

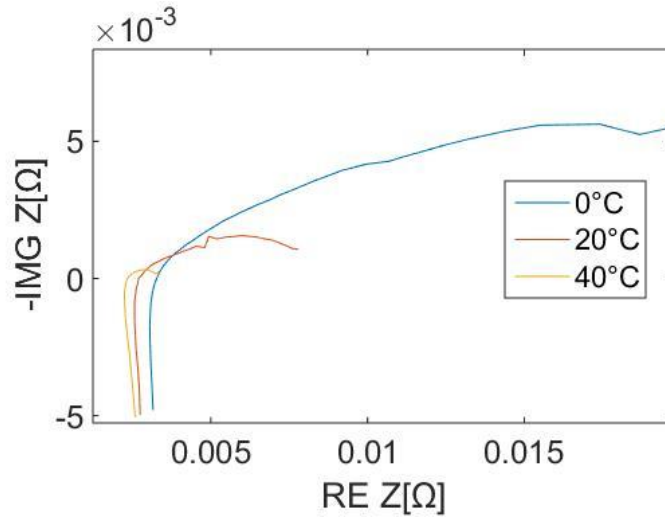


Figure 4.31: EIS Spectra at different Temperatures.

4.2.3. Cycling Measurements

EIS tests were implemented following accelerated aging. The Aging tests shown in Figures 4.32 to 4.34 were accelerated using high cycling current rates 16.2 A (3C) due to time restrictions. Furthermore relatively large cycling depth was used (3.1V to 4.1V). All tests were performed at room temperature (25°C) and 50% State of Charge. Following 20 accelerated aging tests shift of the spectra to the right is observed as shown in Figure 3.4. This shift is primarily due to the increase of ohmic resistance. The aging results are consistent with aging tests presented in [49].

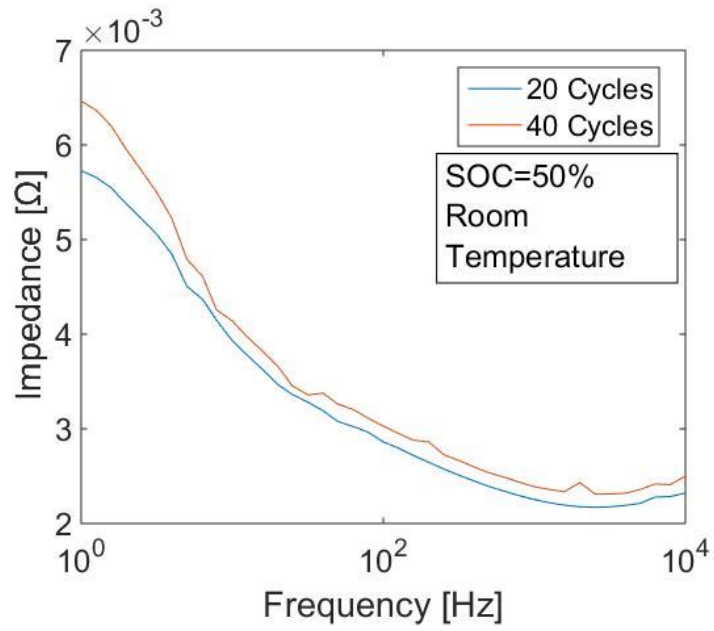


Figure 4.32: Impedance vs. Frequency at different SOH

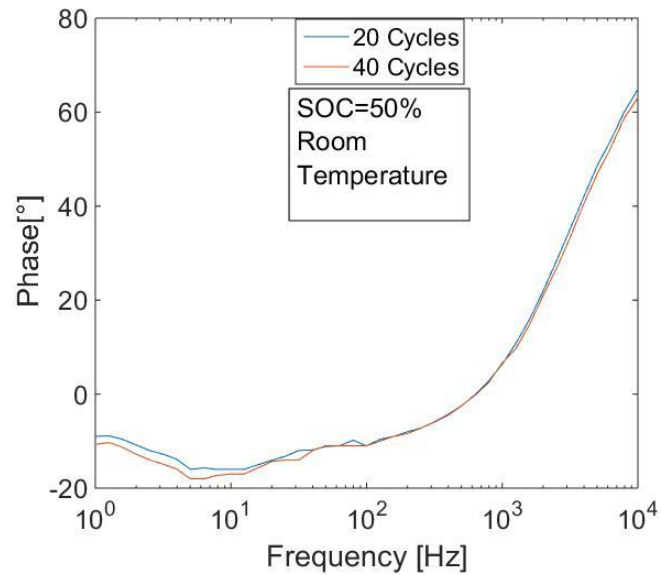


Figure 4.33: Phase Vs Frequency at different SOH

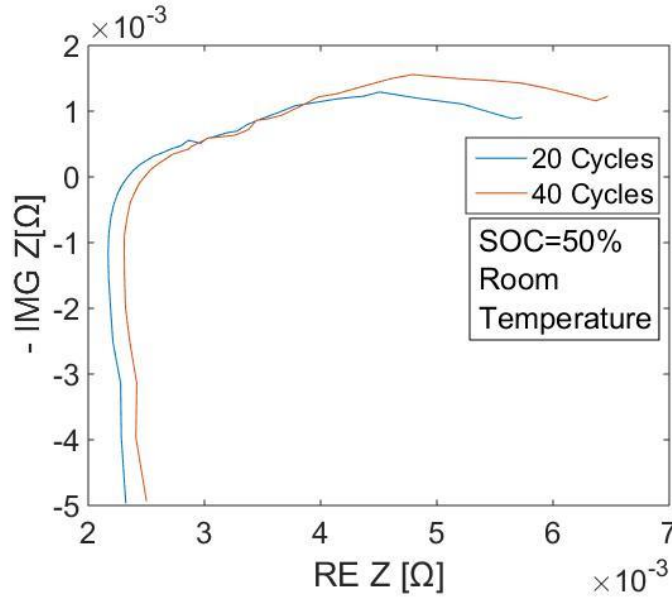


Figure 4.34: EIS Spectra at different SOH

4.3. Equivalent Circuit Modeling

The unknown values in the six equivalent circuit models discussed in chapter one may be estimated using a system identification procedure. Since the models discussed are not linear, MATLAB's Genetic Algorithm (GA) was utilized in order to estimate the unknown quantities. This optimization algorithm, starts off by constructing an initial population. The sequence of new generations are then created based on a few steps. Firstly the current population members are scored according to the *fitness function*. Next, parents (members of populations) are chosen based on their fitness values. Subsequently the members in the current population with the best fitness values are picked as *elite*. Furthermore children are produced from parents either through *mutation* (changes to a single parent) or *crossover*

(combination of properties from pair of parents). Finally new generation is created by replacing the parents with children [60].

The objective function here is the Root-Mean-Squared Error between experimental and simulated Terminal Voltage. The experimental data used for parameter identification is the US06 Driving Schedule. The identified parameters for the six models are shown in Table 4.5. Furthermore the models are validated using the UDDS cycle, and the validated results are shown in Figure 4.35 to 4.40. Third-Order Hysteresis model was able to best simulate the battery Terminal Voltage as shown in Figure 4.41. This result was expected as this model was the most complex of the six equivalent models utilized in this research.

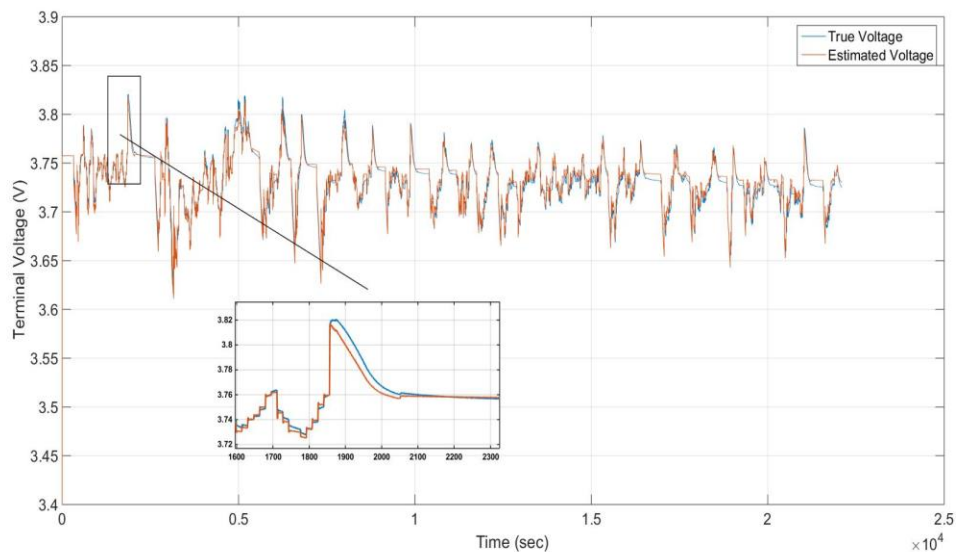


Figure 4.35: Simulated Voltage and Actual Voltage vs. Time for First-Order R-RC Model

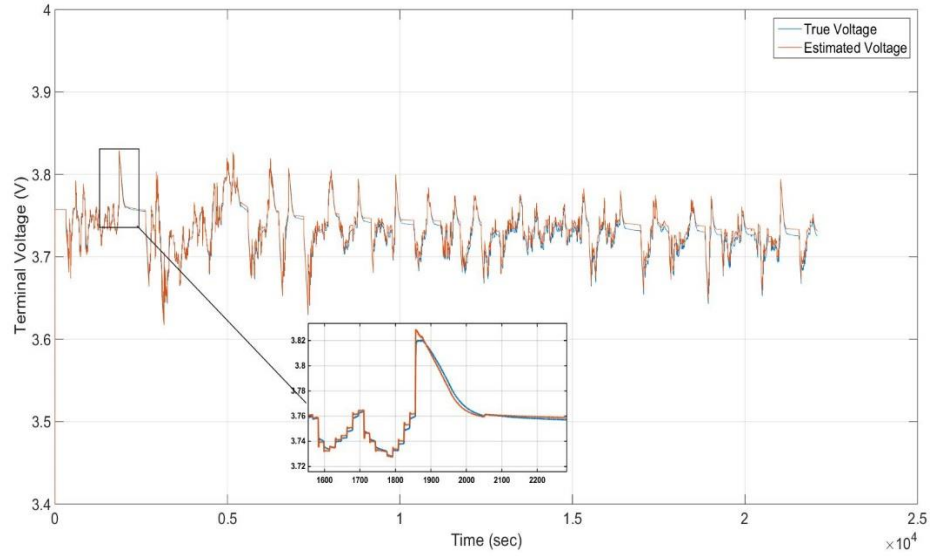


Figure 4.36: Simulated Voltage and Actual Voltage vs. Time for First-Order R-RC Model with Hysteresis

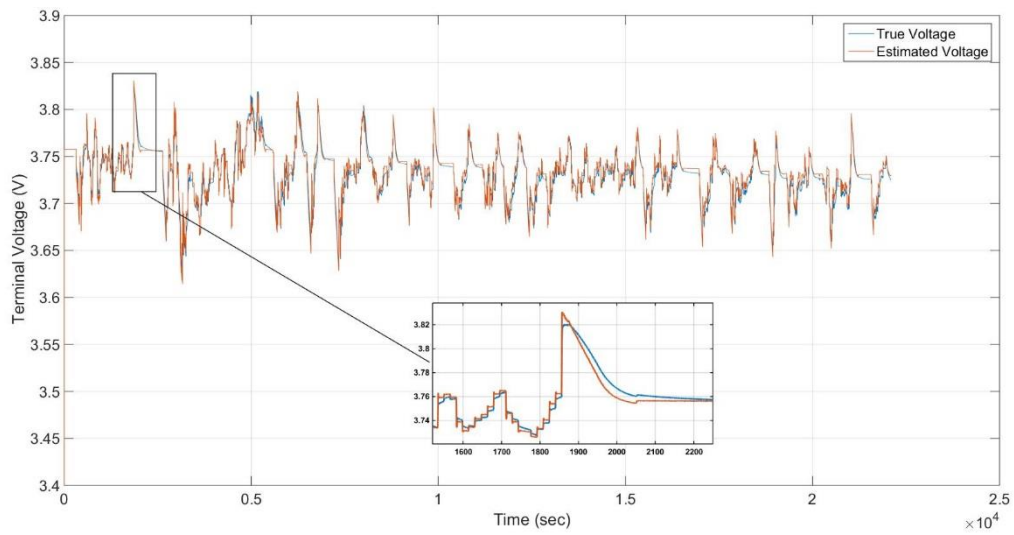


Figure 4.37: Simulated Voltage and Actual Voltage vs. Time for Second-Order R-RC Model

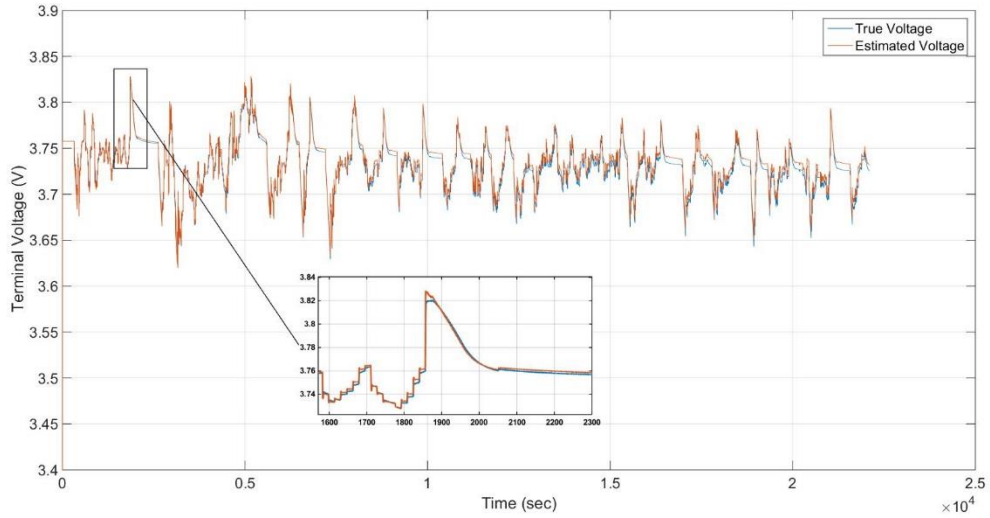


Figure 4.38: Simulated Voltage and Actual Voltage vs. Time for Second-Order R-RC Model with Hysteresis

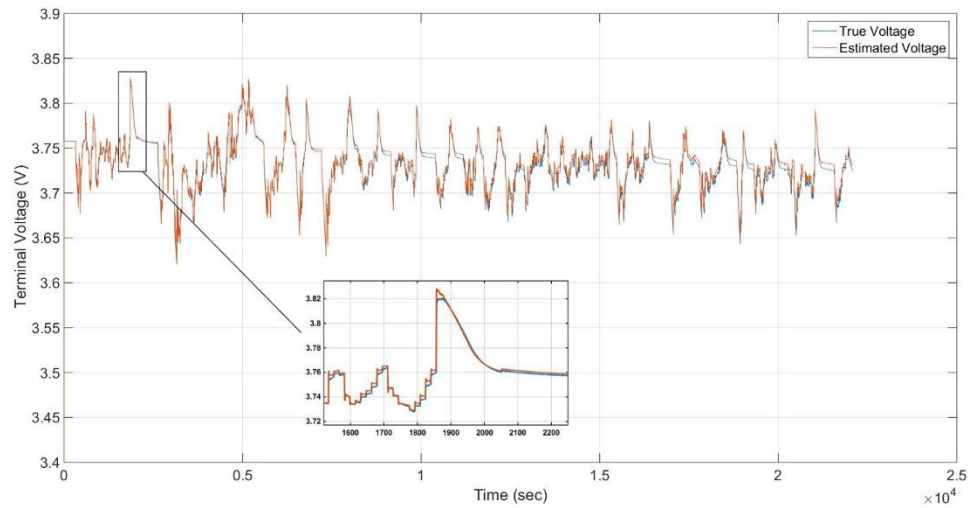


Figure 4.39: Simulated Voltage and Actual Voltage vs. Time for Third-Order R-RC Model

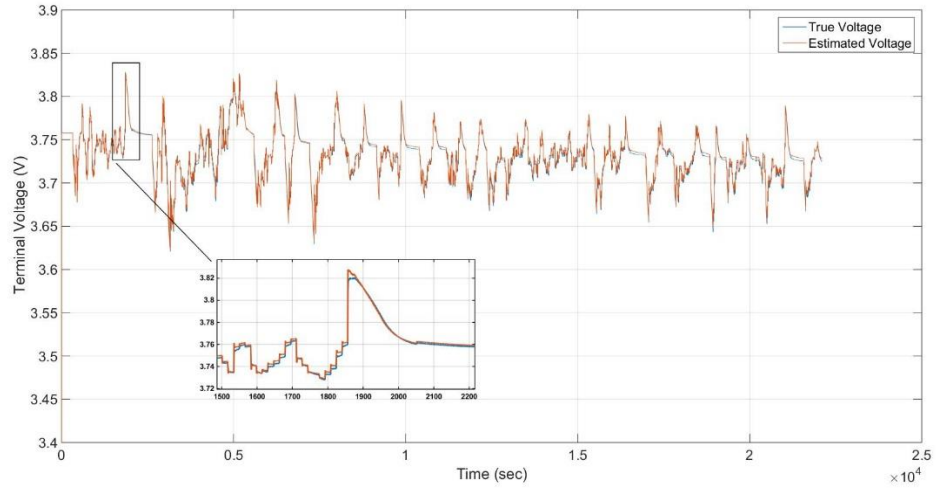


Figure 4.40: Simulated Voltage and Actual Voltage vs. Time for Third-Order R-RC Model with Hysteresis

Table 4.5: Identified parameters for six equivalent circuit models

Parameters	First-Order RC Model	First-Order RC Model Hysteresis	Second-Order RC Model	Second-Order RC Model Hysteresis	Third-Order RC Model	Third-Order RC model Hysteresis
R^+	0.009354	0.0086605	0.0095065	0.008189	0.008083	0.007947
R^-	0.006003	0.0069759	0.007124	0.006924	0.006883	0.006867
R_1	0.007266	0.0063176	0.003817	0.005937	0.004708	0.009453
C_1	5.189e3	3.8593e3	1.872e5	2.972e3	4.359e8	6.493e8
R_2	-	-	0.005155	0.001577	0.004847	0.008227
C_2	-	-	1.003e5	9.129e4	9.900e4	8.450e4
R_3	-	-	-	-	0.005516	0.005612
C_3	-	-	-	-	2.758e3	2.657e3
M^+	-	-0.5320	-	-0.1873	-	0.1980
M^-	-	0.8469	-	0.2839	-	-0.4432
γ	-	0.1267	-	0.2906	-	0.3311

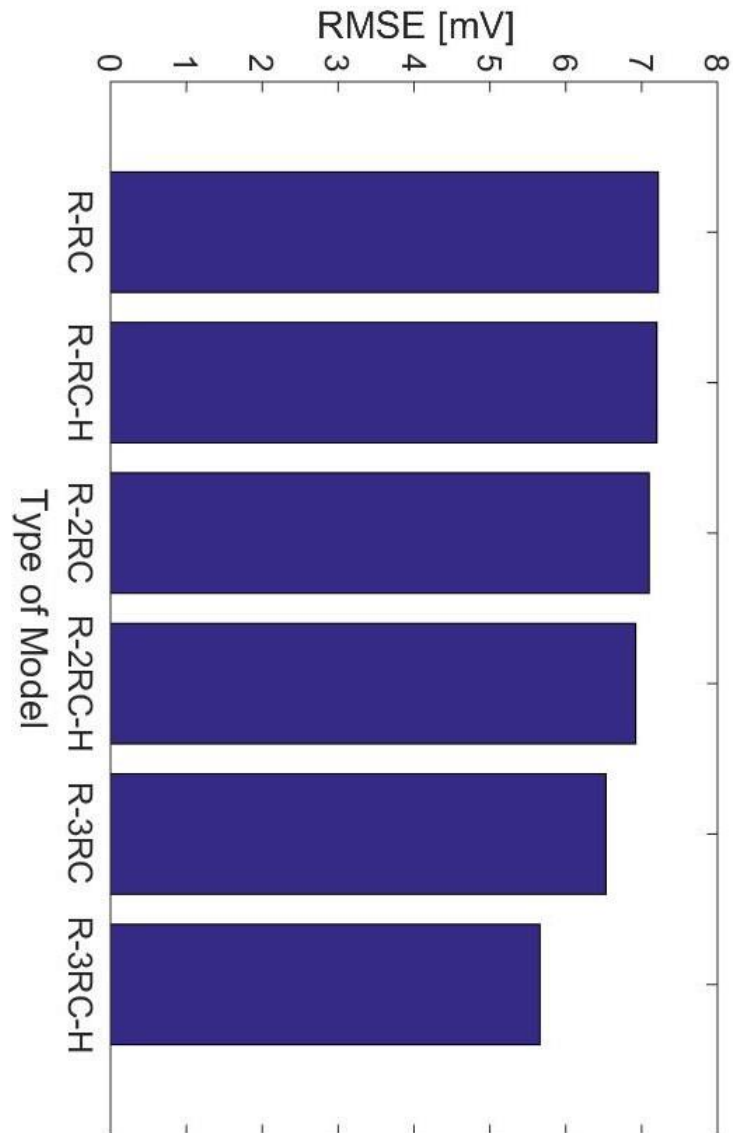


Figure 4.41:RMSE for each model

4.4. EIS Modeling

The Randle model was used in order to model EIS spectra for the cell at 50% SOC and room temperature. The ohmic resistance, which also corresponds to the intersection of the spectra with the real axis was found to be 0235. R_{CT} and C_{DL} responsible for the double layer effect and visually represented by width of the semicircle were found to be .00308 and 2.0015 respectively. Finally the Warburg element was found to be $1.005e - 5$. The Randle model proved to model the EIS spectra to an acceptable degree, however for better results more complex EIS modeling techniques are suggested [52].

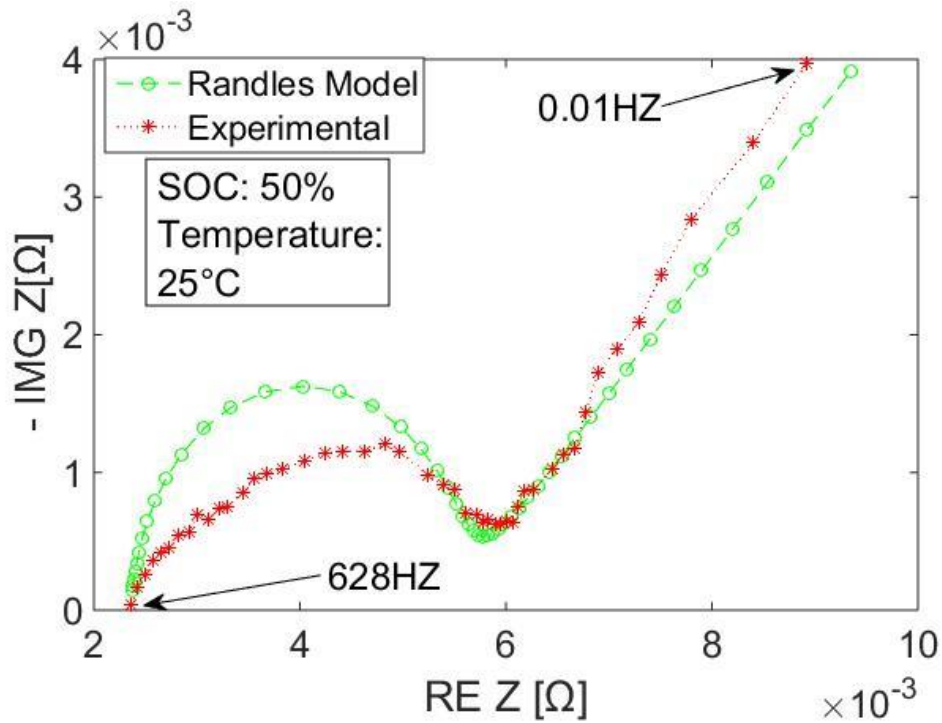


Figure 4.42: Simulated vs. Actual EIS Spectra at 50% SOC and Room Temperature

4.5. Multi-Objective Optimization

Previously similar equivalent circuit models were used for modeling terminal voltage as function of current and state of charge and impedance as a function of frequency. An intriguing idea would be to use one of the models in order to capture both characteristics. Optimizing parameters for the chosen model would require two objective functions. One objective would be to minimize the error between experimental and model terminal voltage, while the other objective would be to minimize the error between experimental impedance and model impedance at different frequencies. This methodology was used in order to optimize the simple model and yielded inadequate results. This failure highlights the importance of Warburg element in modeling the EIS spectra of a given cell.

Chapter 5

Conclusion

5.1. Summary of Research

The primary aim of this research was to develop a lithium-ion cell tester capable of cycle characterization as well as high frequency characterization. Different components of the developed tester that include battery holder, power supply, data acquisition chassis, data acquisition modules, an environmental chamber, a current sensor, thermocouples and a safety circuit were analyzed, selected and integrated. In order to demonstrate capabilities of the developed tester, various tests were performed on a lithium iron phosphate battery cell under different dynamic conditions. The Tests conducted included a static capacity test, SOC-OCV test, drive cycle tests, electro-chemical impedance spectroscopy tests and cycling tests. It was concluded from the static capacity test that the capacity of battery under study is 5.9 Ah. A 10th order polynomial was fit to results from the SOC-OCV test, in order to develop Open Circuit Voltage as a function of SOC for battery terminal Voltage modeling. Drive cycle testing was performed and resulted in experimental current and voltage profiles for the UDDS, HWFET and US06 drive cycles. Cycling tests were

performed in order to emulate degradation of State of Health of a battery as a result of aging.

The effect of State of Charge, ambient temperature and cycling on battery spectra was investigated. It was concluded that change in SOC affects the charge transfer portion of the spectra. Most significant impact of temperature on battery spectra was increased width of the mid-frequency arc at lower temperatures. Finally cyclic aging caused increased Ohmic resistance and therefore a shift of the spectra to the right of the Nyquist plot. The EIS results obtained were in coherence with findings from literature.

The results from the US06 drive cycle were used in order to identify parameters for six equivalent circuit models. The models were then validated using the UDDS cycle. Comparison between RMSE of different models showed that Third-order Hysteresis model provided the best results. Finally the Randle Cell was used in order to model the cell spectra.

It is concluded that the developed fully programmable tester is capable of conducting cycle characterization and high frequency characterization.

5.2. Future Work

Improvements need to be made to the software and hardware in order to create a more user friendly environment. The icons used in the developed testing programs can be enhanced to make the program more presentable. It is suggested that the control strategy for switching between the constant current and the constant voltage protocol be improved.

It is proposed that more channels be incorporated in order to test several batteries concurrently.

It is suggested that the experimental data collected be used to construct more complex system models such as electro-chemical models. Furthermore the system models should be used for State of Charge and State of Health estimation using various methodologies such as Artificial Neural Networks, the Extended Kalman Filter (EKF) and the smooth variable structure filter (SVSF).

References

- [1] M.Armand and J. Tarascon, "Building better batteries," *Nature*, pp. 451,652, 2008.
- [2] G. L.Plett, "Extended Kalman filtering for battery management systems of LiPB-based HEW battery Packs Part 2. Modeling and identification," *Journal of Power Sources*, no. 134, pp. 262-276, 2004.
- [3] K.Bose and Bimal, "Global Warming energy, environmental pollution and the impact of power electronics," *IEEE industrial electronics Magaznie*, p. 6, 2010.
- [4] Inventory, of, US, greenhouse, Gas and emissions, "Total Emissions in 2013," 2013.
- [5] Environment-Canada, "National Inventory Report 1990-2013: greenhouse sources and sinks in Canada," 2015.
- [6] BITRODE-SOVMA-POWER-ELECTRONICS, "Bitrode.com," Bitrode, [Online]. Available: <http://www.bitrode.com/wp-content/uploads/2015/03/01-MCV.pdf>. [Accessed 1 August 2015].
- [7] B.Ratnakumar, M.Smart and S.Surampudi, "lithium, Electrochemical Impedance Specctroscopy and its Applications to Lithium Ion Cells," in *Battery Conference on Applications and Advances*, Long Beach, 2002.
- [8] M.Asift and T.Muneer, "Energy supply, its demand and security issued for developed and emerging economics," *science direct*, vol. 11, pp. 1288-1412, 2007.
- [9] S.Shafiee and E.Topal, "When will fossil fuel reserves be deminished," *Energy policy*, vol. 37, pp. 181-189, 2009.
- [10] D.Anair and A.Mahmassani, "Electric Vehicles Global Warming Emissions and Fuel-Cost Savings across the United States," Union of Concerned Scientists, Cambridge, 2012.
- [11] M.Westbrook, *The Electric Car Development and future of battery, hybrid and fuel-cell cars*, London: The Institute if Electrical Engineers, 2005.
- [12] K. Hoyer, "The history of alternative fuels in transportation:The case of electric and hybrid cars," *Utilities Policy*, vol. 16, pp. 63-71, 2008.

- [13] A. Clerc, *Physique et chimie populaires*, 1881-1883.
- [14] Toyota, "Toyota Celebrates Ten Years of Prius Hybrid," Toyota, 29 July 2010. [Online]. Available: <http://www.toyotainthenews.com/toyota-celebrates-ten-years-of-the-prius-hybrid/>. [Accessed 16 November 2015].
- [15] H.Chen, T.cong, W.Yang, C.Tan, Y.Li and Y.Ding, "Progress in electrical energy storage system: A Critical review," *Progress in Natural Science*, vol. 19, pp. 291-312, 2009.
- [16] B.Scrosati, "Recent advances in lithium ion battery materials," *Journal of Power Sources*, vol. 45, pp. 2461-2466, 2000.
- [17] G.Ren, G.Ma and N.Cong, "Review of electrical energy storage system for vehicular applications," *Renewable and sustainable Energy Reviews*, no. 41, pp. 225-236, 2015.
- [18] S.Moura, J.Siegel, D.Siegel, H.Fathu and A.stefanopoulou, "Education on vehicle electrification: Battery Systems, Fuel Cells, and hydrogen," in *IEEE vehicle Power and Propulsion conference*, 2010.
- [19] M.Osiak, H.Geaney, E.Armstrong and C.O'Dwyer, "Structuring materials for lithium-ion batteries: Advancements in nanmaterial structure, composition, and defined assembly on cell performance," *Materials Chemistry*, vol. 2, pp. 9433-9460, 2014.
- [20] G. L. Plett, "Extended Kalman filtering for battery management systems of LiPB= based HEV battery packs part 1. Background," *Journal of power sources*, no. 134, pp. 252-261, 2004.
- [21] M. Gholizadeh and F. R. Salmasi, "Estimation of state of charge, Unkown Nonlinearities, and State of Health of a Lithium-Ion Vattery Based on a Comprehensive Unobservable Model," *IEEE Transactions on industrial Electronics*, vol. 61, no. 3, pp. 1335-1345, 2014.
- [22] S.Cho, H.Jeong, C.Han, S.Jin, J.Lim and J.Oh, "State-of-charge estimation for lithium-ion batteries under various operating condition using an equivalent circuit model," *Computers and chemical Engineering*, no. 41, pp. 1-9, 2012.
- [23] S.Piller, M.Perrin and A.Jossen, "Methods for state-of-charge determination and their application," *Journal of Power Sources*, no. 96, pp. 113-120, 2001.

- [24] M.Charkhgard and M.Farrokhi, "State-of Charge Estimation for Lithium-Ion Batteries Using Neural Networks and EKF," *IEEE Transactions on Industrial Electronics*, vol. 57, no. 12, pp. 4178-4187, 2010.
- [25] M. Farag, "Lithium-Ion Batteries: Modelling and State of Charge Estimation," McMaster University, Hamilton, 2013.
- [26] Y.Zou, X.Hu, H.Ma and S.Li, "Combined State of Charge and State of Health estimation over lithium-ion battery cell cycle lifespan for electric vehicles," *Journal of Power Sources*, no. 273, pp. 793-803, 2015.
- [27] D.Andre, C.Appel, T. Sozka-Guth and D. Sauer, "Advanced mathematical methods of SOC and SOH estimation for lithium-ion batteries," *Journal of Power Sources*, no. 224, pp. 20-27, 2013.
- [28] H.Han, H.Xu, Z.Yuan and Y.Shen, "A New SOH Prediction Model for Lithium-ion Battery for Electric Vehicles," in *International conference on Electrical Machines and Systems*, Hangzhou, 2014.
- [29] R.Ahmad, "MechEng 739," Avenue, McMaster, 1 January 2014. [Online]. Available: <https://avenue.cilmcmaster.ca/d2l/home/147979>. [Accessed 15 June 2015].
- [30] X.Hu, S.Li and H.Peng, "A comparative study of equivalent circuit models for Li-ion batteries," *Journal of Power Sources*, no. 198, pp. 359-367, 2012.
- [31] B.Liaw, G.Nagasubramanian, R.Hungst and D.Doughty, "Modeling of lithium ion cells_A simple equivalent-circuit model approach," *Solid State Ionics*, no. 175, pp. 835-839, 2004.
- [32] S.Cho, H.Jeong, C.Han, S.Jin, J.Lim and J.Oh, "State-of-charge estimation for lithium-ion batteries under various operating conditions using an equivalent circuit model," *Computers and chemical engineering*, no. 41, pp. 1-9, 2012.
- [33] H.He, R.Xiong and J.Fan, "Evaluation of Lithium-Ion Battery Equivalent Circuit Models for State of Charge Estimation by an Experimental Approach," *Energies*, no. 4, pp. 582-598, 2011.
- [34] R.Klein, N.Chaturvedi, J.Christensen, J.Ahmed, R.Findeisen and A.Kojic, "State estimation of reduced electrochemical model of a lithium-ion battery," in *American Control Conference*, Baltimore, 2010.

- [35] D.Domenico, G.Giengo and A.Stefanopoulou, "Lithium-Ion battery State of Charge estimation with a Kalman Filter based on electrochemical model," in *international conference on control applications*, Texas, 2008.
- [36] J.Newman and W.Tiedmann, "Porous-Electrode Theory with Battery Applications," *ALChE Journal*, vol. 21, no. 1, pp. 25-41, 1975.
- [37] M.Doyle, T.Fuller and J.Newman, "Modeling of Galvanostatic Charge and Discharge of the Lithium/polymer/insertion cell," *Journal of electrochem*, vol. 140, no. 6, pp. 1526-1533, 1993.
- [38] D.Domenico, A.Stefanopoulou and G.Fiengo, "Lithium-Ion Battery State of Charge and Critical Surface Charge Estimation using an Electrochemical Model-Based Extended Kalman Filter," *Journam of Dynamic Systems*, vol. 132, pp. 061302-1-11, 2010.
- [39] N.Chaturvedi, R.Klein, J.Christensen, J.Ahmed and A.Kojic, "Modeling, estimation and control challenges for lithium-ion batteries," in *American Control Conference*, Baltimore, 2010.
- [40] J.Forman, S.Bashash, J.Stein and H.Fathy, "Reduction of an electrochemistry-based Li-ion Battery Model via Quasi-linearization and pade approximation," *Journal of The Electrochemical Society*, vol. 158, no. 2, pp. A93-A101, 2010.
- [41] C.Wang, W.Gu and B.Liaw, "Micro-Macroscopic Coupled Modeling of Batteries and Fuel Cells part I. Model development," *Journal of The Electrochemical Society*, vol. 145, no. 10, pp. 3407-3417, 1998.
- [42] J.Lee, A.Chemistruck and G.Plett, "One-dimensional physics-based reduced-order model of lithium-ion dynamics," *Journal of Power Sources*, vol. 220, pp. 430-448, 2012.
- [43] C.Speltino, D.Domenico, G.Fiengo and A.Stefanopoulou, "Experimental Identification and Validation of an Electrochemical Model of a Lithium-Ion Battery," in *European control conference*, Budapest, 2009.
- [44] P.Gambhire, N.Ganesan, S.Basu, K.Hariharan, S.Kolake, T.Song, D.Oh, Y.Yeo and S.Doo, "A reduced order electrochemical thermal model for lithium ion cells," *Journal of Power Sources*, vol. 290, pp. 87-101, 2015.

- [45] P.Amirbbavandpour, W.Shen, D.Mu and A.Kapoor, "An improved theoretical electrochemical-thermal modelling of lithium-ion battery packs in electric vehicles," *Journal of Power sources*, vol. 284, pp. 328-338, 2015.
- [46] L.Rao and J.Newman, "Heat-Generation Rate and General Energy Balance for Insertion Battery Systems," *Journal of Electrochemistry*, vol. 144, no. 8, pp. 2697-2704, 1997.
- [47] Y.Xie, J.Li and C.Yuan, "mathematical modeling of the electrochemical impedance spectroscopy in lithium ion battery," *Electrochimica Acta*, vol. 127, pp. 266-275, 2014.
- [48] D.Andre, M.Meiler, K.Steiner, C.Wimmer, T.Soczka-Guyh and D.Sauer, "investigation, Characterization of high-power lithium-ion batteries by electrochemical impedance spectroscopy. I. Experimental," *Journal of Power Sources*, vol. 196, pp. 5334-5341, 2011.
- [49] D.Stroe, M.Swierczynski, A.Stan, V.Knap, R.Teodorescu and S.Andreasen, "Diagnosis of Lithium-Ion Batteries State-of-Health based on Electrochemical Impedance Spectroscopy Technique," in *Energy Conversion Congress and Exposition(ECCE)*, Pittsburgh, 2014.
- [50] J.Jespersion, A.E.Tonnesen, K.Norregaard, L.Overgaards and F.Elefsen, "Capacity Measurements of Li-Ion Batteries using AC Impedance Spectroscopy," *World Electric Vehicle Journal Vol.3*, vol. 3, pp. 127-133, 2009.
- [51] R.Robinson and C.Corporation, "On-line Battery testing: a reliable method for determining battery health," in *telecommunications energy conference* , Boston, 1996.
- [52] S.Li, B.Wang, H.Peng and X.Hu, "An electrochemistry-based impedance model for lithium-ion batteries," *Journal of Power Sources*, vol. 258, pp. 9-18, 2014.
- [53] D. C. Beasley, "Basics of Electrochemical Impedance Spectroscopy," Gamry Instruments, 29 April 2015. [Online]. Available: <http://www.gamry.com/application-notes/EIS/basics-of-electrochemical-impedance-spectroscopy/>. [Accessed 10 Nov 2015].
- [54] A.Jossen, "Fundamentals of battery dynamics," *Journal of Power Sources* , vol. 154, pp. 530-538, 2005.

- [55] Program-U.S-Department-of-Energy-Vehicle-Technologies, "Battery Test Manual For Plug-In Hybrid Electric Vehicles," The Idaho National Laboratory Operated by Battelle Energy Alliance, Idaho, 2009.
- [56] PNGV-Electrochemical-Energy-Storage-Team, "PNGV Battery Test Manual," U.S Department of Energy, Idaho, 2001.
- [57] K. t. p. supplier, "Operator's Manual BOP-MG 1KW," KEPCO, 2015. [Online]. Available: <http://www.kepcopower.com/support/bop1kw-mg-opr-r18h.pdf>. [Accessed 14 Jan 2016].
- [58] Environmental-Protection-Agency, "epa.gov," 2012. [Online]. Available: <http://www.epa.gov/otaq/standards/light-duty/index.htm>. [Accessed 10 09 2015].
- [59] "Testing and Measuring Emissions-Dynamometer Drive Schedules," Environmental Protection Agency , 2 6 2013. [Online]. Available: <http://www.epa.gov/nvfe/testing/dynamometer.htm>. [Accessed 10 09 2015].
- [60] D.Abraham, M.Furczon, S.Kang, D.Dees and A.Jansen, "Effect of electrolyte composition on initial cycling and impedance characteristics of lithium-ion cells," *journal of Power Sources*, vol. 180, pp. 612-620, 2009.
- [61] Mathworks, "How the Genetic Algorithm Works," Mathworks, 2015. [Online]. Available: <http://www.mathworks.com/help/gads/how-the-genetic-algorithm-works.html>. [Accessed 5 January 2016].
- [62] "NI Compact DAQ," National Instruments, 6 11 2014. [Online]. Available: <http://www.ni.com/datasheet/pdf/en/ds-255>. [Accessed 4 12 2015].

Appendix A.1

A more detailed description of components of the designed tester.

Data Acquisition Chassis:



Figure A.1: NI cDAQ-9188 [61]

Table A.1: Specifications for NI cDAQ-9188

Item	Specification	
Timing	Resolution	32 bits
	External Base Clock Frequency	0-20 MHz
Temperature	Operating	-20 to 55°C
	Storage	-40 to 85°C
Humidity	Operating	10 to 90% RH
	Storage	5 to 95%RH
Physical Characteristics	Weight	Approx. 900 grams
	Dimensions	194mm x 88.7mm x33.6mm
Power Requirements	Input Voltage Range	9-30 V
	Input Power	15 W

Data Acquisition Modules:



Figure A.2: NI 9213, NI 9264, NI 9239, NI 9205

Environmental Chamber:

Table A.2: Rate Specifications for the Environmental Chamber

Difference in Temperature	Rate
Ambient to 116°C	20 Minutes
Ambient to 177°C	30 Minutes
Ambient to -40°C	20 Minutes
Ambient to -44°C	25 Minutes
Ambient to -68°C	40 Minutes